2017

The Physics of Rodent Ultrasonic Vocalizations

Matthew Dornfeld

THE PHYSICS OF RODENT ULTRASONIC VOCALIZATIONS

A Thesis Presented To the Faculty of

The Rockefeller University

in Partial Fulfillment of the Requirements for

the degree of Doctor of Philosophy

by

Matthew Dornfeld

June 2017

THE PHYSICS OF RODENT ULTRASONIC VOCALIZATIONS

Matthew Dornfeld, Ph.D.

The Rockefeller University 2017

Although much work has been done on the physics of vocalizations caused by the vibrating motion of vocal folds, relatively little work has been done on the physics of ultrasonic vocalizations (USVs). There are two orders of mammals known to make these kind of vocalizations: cetaceans and rodents. Of these two the mechanism behind the rodent calls are better understood. Thus, this thesis investigates the physics of rodent USVs with the hope that findings will help elucidate the mechanisms behind cetacean USVs. Chapter 1 discusses the anatomical background of rodent vocal tracts, evolutionary pressures that shaped the development of USVs, physical modeling of vibrating vocal folds, and experimental work that discounts the possibility of vibrating vocal folds as the mechanism behind rodent USVs. Chapter 2 discusses acoustic and fluid dynamics background as well as a previously proposed physical model, known as the hole tone, for the rodent USV mechanism. Chapter 3 discusses an original data analysis of rodent USVs. This analysis exploits the presence of frequency jumps in the USVs. These frequency jumps are extracted. A machine learning model is then used to fit the frequency jumps to acoustic equations. The results of this analysis show that the hole tone model is incorrect. Chapter 4 discusses original modeling of the rodent vocal production mechanism, in which the rodent vocal tract is treated as a resonator driven by a jet of air emerging from the vocal folds.

This representation of the rodent vocal tract is used to derive a set of time domain acoustic oscillator equations, which describe the transient acoustics of rodent USVs. It is found in chapter 4 that an additional driving mechanism is needed in the oscillator equations, or the acoustic oscillations will decay to a fixed point. Chapter 5 discusses several attempts at including this driving mechanism by considering the forcing that results from the formation of vortex rings in the rodent vocal tract. First, a linear frequency domain approach is attempted. However, it is found that this approach is incompatible with the time domain equations of chapter 4. Next, a nonlinear time domain approach is attempted. This approach is compatible with the time domain equations of chapter 4, and solves the decay problem that occurs without the additional driving force. Furthermore, the model is able to reproduce the 22 kHz alarm call made by rats. However, it is unable to produce the higher harmonics or the frequency jumps observed in rodent USVs. It is concluded that the model is successful in producing the fundamental frequency of the rodent vocal tract, but it seems to be neglecting a mechanism which can account for the higher harmonics and the frequency jumps.

This work is dedicated to my mother. Without her support I never would have made it this far.

Acknowledgments

I would like to acknowledge Marcelo Magnasco, Oreste Piro, Diego Laplagne, Martin Elias Costa, Carl Modes, Leandro Alonso, Ana Hocevar, Alexander Petroff, Jacob Oppenheim, Keith Hayton, Sean Woodward, and Dmitrios Moirogiannis for their invaluable contributions and collaborations.

Table of Contents

List of Figures

Chapter 1

Background on Sonic and Ultrasonic Vocalizations

1.1 Introduction

It is well known that in most animals vocalizations are produced in a larynx like structure by the mechanical vibrations of membranous tissues called vocal folds. These vocalizations tend to have frequency content that mostly lie in the sonic range $(0 - 20kHz)$. These types of vocalizations are very well studied from both a theoretical and experimental point of view. From the theoretical standpoint there has been a great deal of success modeling the motion of vocal folds as spring like oscillators [18]. However mammalian ultrasonic vocalizations (USVs) are comparatively much less studied. In particular the method by which they are produced is largely not understood.

Cetaceans are perhaps the best known order of mammals to vocalize in the ultrasonic range, but ethical and practical constraints make them a poor laboratory organism. Lesser known however rodents, a very common laboratory organism, also display a wide variety of calls in the ultrasonic range. This thesis focuses on the USV production mechanism in rats with the hope that findings will also help elucidate the production mechanism in cetaceans.

1.2 Ethology of Rodent Ultrasonic Vocalizations

To be a rodent is to be prey. A large number of vertebrate predators make use of rodents as a primary food source. Birds of prey are especially effective hunters, depleting local rodent populations in an area before undertaking migrations to search for new hunting grounds. With these environmental pressures it is no wonder many rodents have evolved burrowing behaviors as a strategy for hiding from these dangers. Predators, however, have evolved strategies to negate the advantages obtained by burrowing. Specialized predators such as weasels have even evolved slender and elongated bodies to capture rodents from their burrows. Thus, even the relative safety of their nest areas can be ineffective protection. Some studies report that predation can have a staggering 95% impact on rodent populations [19]. With these considerations in mind, it is quite reasonable to expect that predation has been one of the driving factors in the evolution of rodent social behavior

[20]. Perhaps one of the more powerful and complex evolutionary traits in vertebrates is that of vocal communication. As a results of their position in the food chain some rodent species have developed a peculiar form of vocal communication, one that lies entirely in the ultrasonic range. The advantage of this form of vocalization is the ability of an individual to communicate and provide warning to conspecifics with lowered risk of detection by predators. In this section I will discuss the origins of and behavior surrounding rodent ultrasonic vocalizations (USVs), more specifically those of rats.

There is evidence that the phylogenetic origins of social vocalizations in vertebrates are over 400 million years old. Bass et al. have shown that the same vocal region in the caudal hindbrain and rostral spinal cord region is present in fish and all major lineages of vocal tetrapods [21]. Rodent USV as a defensive adaptation is however a much more recent development. The suborder of myomorph rodent emerged about 40 million years ago, while the genera Mus and Rattus emerged as distinct groups between 16 and 23 million years ago. Species of both these genera use ultrasound for communication. Thus, it is likely rodent USV emerged somewhere between 20 and 40 million years ago. It is believed that the rodent's nocturnal lifestyle predisposed them to evolve ultrasonic communication as a defensive strategy. Increased visual acuity is not beneficial to nocturnal animals. Thus, many rodents have evolved increased auditory acuity that extends into the ultrasonic range, and auditory sensitivity in the ultrasonic range is a prerequisite for communication in those frequencies.

It has been suggested by Blumberg and Alberts and then later by Hofer and Shair that rodent USVs originally evolved as a way for infants to help stimulate endogenous heat production. Blumberg and Alberts observed during vocalization closure of the larynx results in an increase in intrathoracic pressure, a phenomenon known as laryngeal braking. Under certain circumstances laryngeal braking can increase pulmonary oxygenation of the blood. They hypothesized that this increased blood oxygen level could assist brown adipose tissue with increasing the body temperature of a hypothermic infant [22]. In their 1992 paper, Hofer and Shair observed that when infant rats are brought into a comatose state of hypothermia, at a body of temperature of 20C, they will begin vocalizing in the ultrasonic range. When the comatose rat pup is placed in contact with its mother there is initially no change in the emission of USVs. However when its temperature warms to 25C it becomes responsive to the mothers presence and ceases vocalizing [23]. This suggests that infant USVs serve a dual purpose: to assist in raising the body temperature of a hypothermic pup and to summon the mother to a pup in distress. However, it does not conclusively determine the original evolutionary strategy surrounding infant USVs. To help elucidate this Hofer and Shair compared rising body temperature in two groups of hypothermic rat pups, a control group and a group devocalized through laryngeal denervation or tracheostomy. They found that the body temperature of the control group rose faster than the devocalized group, and 20% of the devocalized group did not recover at all. Autopsy of these specimens found pulmonary edema [24].

Thus it seems likely that USVs in rodents originally evolved as a strategy for increasing the body temperature in infant hypothermia and the maternal instinct to interpret that as a distress call arose later [25].

In adult rodents ultrasonic vocalization requires complex laryngeal control, prolonged exhalation, and increased lung pressure. These significant energy demands are consistent with the adaptive value of ultrasonic communication in avoiding detection by predators. The acoustic properties of vocalizations in the ultrasonic range confer this adaptive value. Because acoustic waves in the ultrasonic range spread at a lower rate than those in the sonic range, USVs allow individuals to better control the directionality of their calls. Ultrasonic acoustic waves also attenuate at a much higher rate in atmosphere and solid matter than sonic waves, minimizing the chance of detection by an outside predator. Furthermore, because rodent USVs are largely monotonal in frequency, it is more difficult to localize their source, another acoustic property that makes detection more difficult by a predator. These acoustic properties make USVs ideal for short-range communication with conspecifics inside of burrows [26].

Rat species are commonly used when studying rodent USVs. This is because of the ease of laboratory handling and their highly social nature. Adult rats exhibit a large repertoire of USVs. One of the most easily recognizable of their USVs is the 22 khz alarm call (Fig. **??**). This type of vocalization is elicited by the presence of a predator or by social defeat. Blanchard et al. were able to observe these calls in burrowing lab rats when exposed to a cat

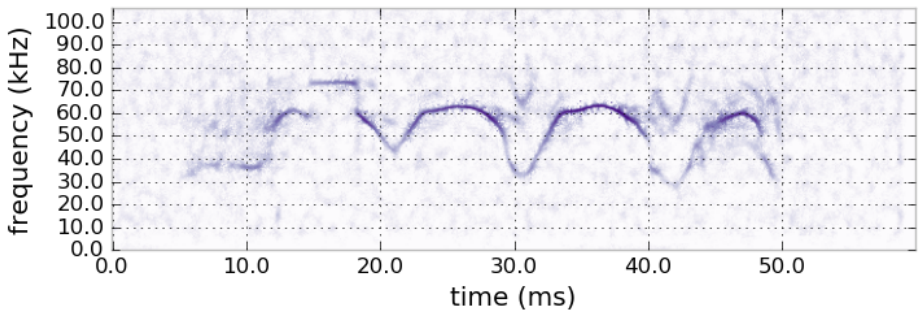

Figure 1.1: Spectrogram of 60-kHz trill call.

[27]. Panksepp et al. were also able to observe this type of call after Long-Evans rats submitted to more socially aggressive conspecifics in a laboratory setting [28]. Brudzynski and Brihari were able to artificially stimulate 22 kHz alarm calls by intracerebral injection of the acytelcholine agonist carbachol, which is known to cause an acute stress response [29]. [30].

Another distinct group of rat USVs lies in the $50 - 85$ kHz range (Figs. 1.1, 1.2, 1.3). They are associated with positive social interactions with conspecifics (mating and playful fighting) and anticipation of food. Aversive stimuli such as social defeat, frustrating situations, and electrical shock decrease the number of calls emitted in this range. Mu-opiate and dopamine agonists as well as electrical stimulation of the mesolymbic dopamine system also elicit calls in this frequency region [30]. The calls in this region exhibit considerable variability. Beyond signifying positive emotional states it is not entirely certain what information they are encoding.

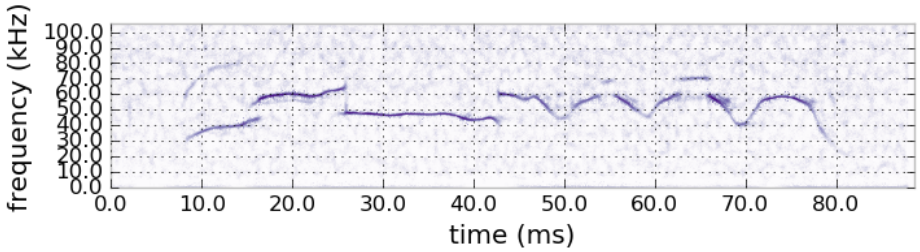

Figure 1.2: Spectrogram of flat to trill call.

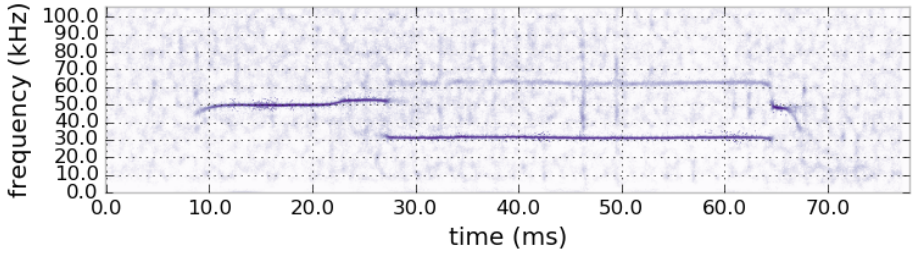

Figure 1.3: Spectrogram of 30-kHz to 50-khz flat call with frequency jump.

1.3 Anatomy of the Larynx

The essential structure of the larynx is mostly conserved throughout mammals. It consists of a cartilagenous framework, extrinsic laryngeal muscles, which connect the framework to its surroundings in the body, and smaller intrinsic laryngeal muscles, which lie entirely inside the larynx. The cartilage framework consists of the cricoid, thyroid, and arytenoid cartilages (Fig. 1.4). The cricoid cartilage is ring like in shape and sits at the top of the trachea. The thyroid cartilage, also known as the Adams apple, attaches to the cricoid cartilage posteriorly. It posses a few degrees of articulation. At the top of cricoid cartilage ring sit the arytenoid cartilages. They are roughly pyramidal in shape and have complex rotational articulations. Two sets of intrinsic laryngeal muscles, the posterior and lateral cricoarytenoid muscles, attach the arytenoid cartilages to the cricoid cartilage: and are responsible for their abduction and adduction. Adduction of arytenoids occurs during swallowing, to prevent debris from entering the trachea, and during phonation, to set the vocal folds in a position in which they can oscillate. Adduction occurs when the lateral cricoarytenoid muscles, attached to the front of the cricoid, contract, causing the arytenoids to rotate inward. The interarytenoid muscles, which as its name suggest lies in between the arytenoids assists with this process. Abduction occurs during inspiration and when the posterior cricoarytenoid muscles contract rotating the arytenoids outward [31]. The thyroarytenoid muscles attach at the arytenoids anteri-

orly and run to the thyroid cartilage posteriorly. These muscles are covered with a layer of connective tissue. Collectively these muscles and connective tissue structure are called the vocal folds. In common speech this structure is called the vocal cords, which is somewhat of a misnomer, since they are not chord shaped, nor do they generate sound in the manner of a vibrating guitar string. As mentioned above, rotation of the arytenoids can abduct and adduct the vocal folds by contraction of the cricoarytenoid and inter-arytenoid muscle. Contraction of the thyroarytenoid muscles themselves can further adduct the vocal folds, in addition to shortening them by rotating the arytenoids inward. Contraction of the cricothyroid muscles can lengthen the vocal folds. A total of five muscles contribute to the movement of and tension of the vocal folds. Considering the small size of the structure this is a remarkable degree of control, which is used for the complicated process of vocalization. Fig. 1.5 is an illustration of the intrinsic laryngeal muscles [31].

Innervation of the vocal fold musculature is completely supplied by the vagus nerve. Efferent motor fibers of the nerve emerge from the nucleus ambiguus in the medulla oblongata. Afferent sensory fibers of the nerve also terminate there. At the root of the neck the vagus branches into left and right components. Each component branches again into the superior laryngeal nerve (SLN) and the recurrent laryngeal nerve (RLN). The RLN contains only motor fibers, while the SLN contains both motor and sensory fibers. The SLN runs to the larynx, where it divides into the external

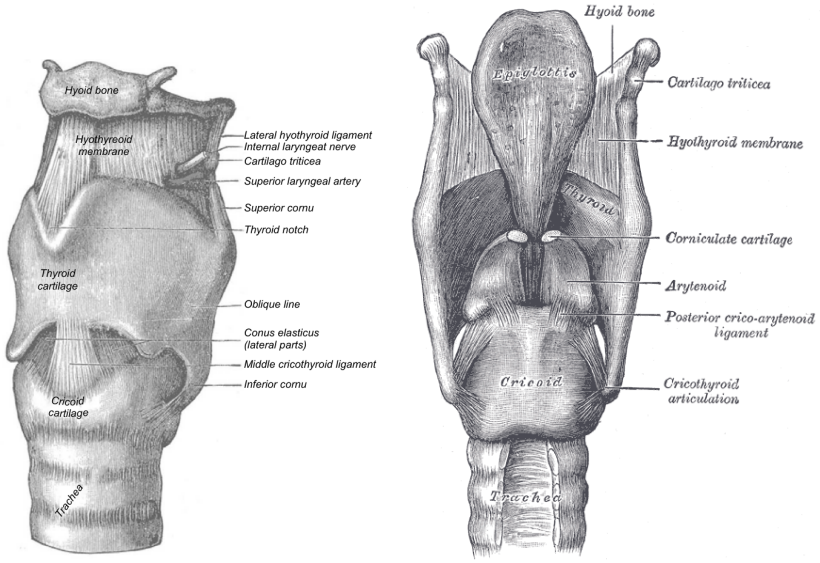

(a) (b)

Figure 1.4: Ligaments of the human larynx (a) antero-lateral view (b) posterior view. Reprinted from *Gray's Anatomy*. This work is in the public domain [1].

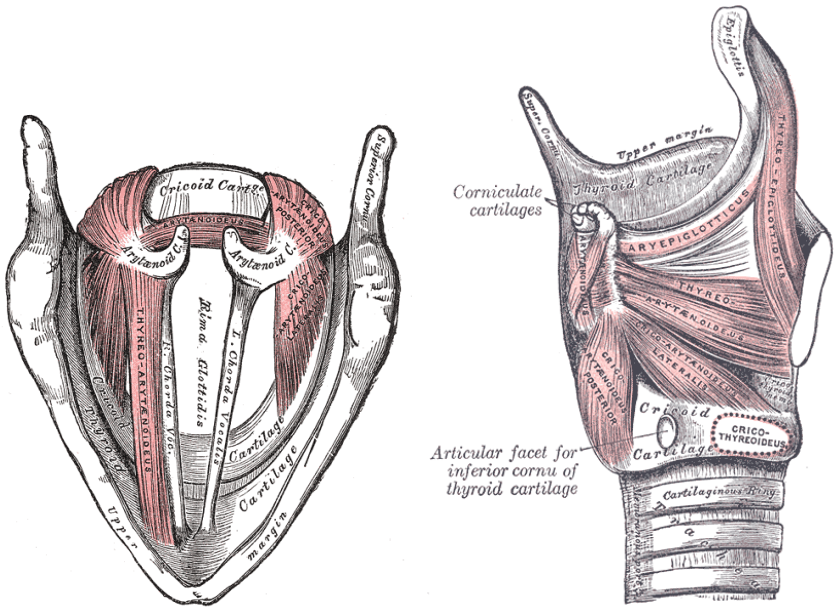

(a) (b)

Figure 1.5: (a) Top view of human laryngeal muscles (b) Side view of the laryngeal muscles. Shown in both (a) and (b) are the thyroarytenoid muscles, the interarytenoid muscles (arytanoideus), the posterior cricoarytenoid muscles, and lateral cricoarytenoid muscles. Shown only in (b) is the cricothyroid muscle. Reprinted from *Gray's Anatomy*. This work is in the public domain [1].

and internal branches. The external branch provides motor control to the cricothyroid muscle. The internal branch carries sensory information from the mucosa lining, larynx, epiglottis, and part of the tongue. It enters the larynx through the thyrohyoid membrane. The left and right RLNs branch from the vagus nerve low in the neck. Upon reaching the larynx the RLNs branch again, innervating the posterior cricothyroid muscles, lateral cricothyroid muscles, interarytenoid muscle, and the thyroarytenoid muscle [32]. Fig. 1.6 illustrates the path taking by the branchings of the vagus nerve. The order of branching is stereotyped, but the precise branching pattern can vary between individuals. Each laryngeal muscle can be individually controlled by the human motor cortex. Such a high degree of control is indicative of the large evolutionary advantage imparted by vocal communication [31].

1.4 Physics of Vibrating Vocal Folds

Phonation is the physical process underlying vocalization. It is the process by which the vocal folds produce sound through vibration. The basics physics and physiology underlying phonation are as follows. Stimulation of the intrinsic laryngeal muscles from the RLN causes the vocal folds to adduct into a closed position with a converging profile. With the vocal folds in a closed position, air flow from the lungs results in an increase in subglottal pressure. Because of the converging profile, this increase in subglottal pressure will force the vocal folds apart. The inferior portion of the vocal folds open

first. A wave, compressing the tissue laterally, travels upward to the superior portion of the vocal fold. This is called a mucosal wave. The forcing apart of the vocal folds causes an increase in airflow, which corresponds to a drop in the pressure holding them open. Abduction continues until this pressure can longer balance the elastic restoring force of the vocal fold tissue. At this point the vocal folds will begin to close. Their most inferior points will collide before returning to their closed position with a converging profile, when the cycle will start again [33, 31].

Detailed studies have been performed indicating the sound properties of vocalizations can be controlled through activity of the laryngeal muscles. In most models the cricothyroid and thyroarytenoid are the most important muscles for control of vocal acoustics. Studies have shown activation of the cricothyroid muscle increases the fundamental frequency f_0 of vibration by increasing the internal tension of the vocal folds. The role of the thyroarytenoid muscle in the modulation of f_0 is less clear. Studies in canines show f_0 increases with thyroarytenoid activation when f_0 is in the modal register but decreases when f_0 is the falsetto register [31, 33, 34]. The body-cover theory proposed by Hirano and advanced by Titze attempts to explain modulations of fundamental frequency as a function of cricothyroid and thyroarytenoid muscle activation [35]. The body-cover theory states that two distinct layers of tissue contribute to vocal fold tension differently. The outer layer, the cover, is composed of epithelial tissue as well as the superficial and intermediate layers of the lamina propria. The cover does not have contractile prop-

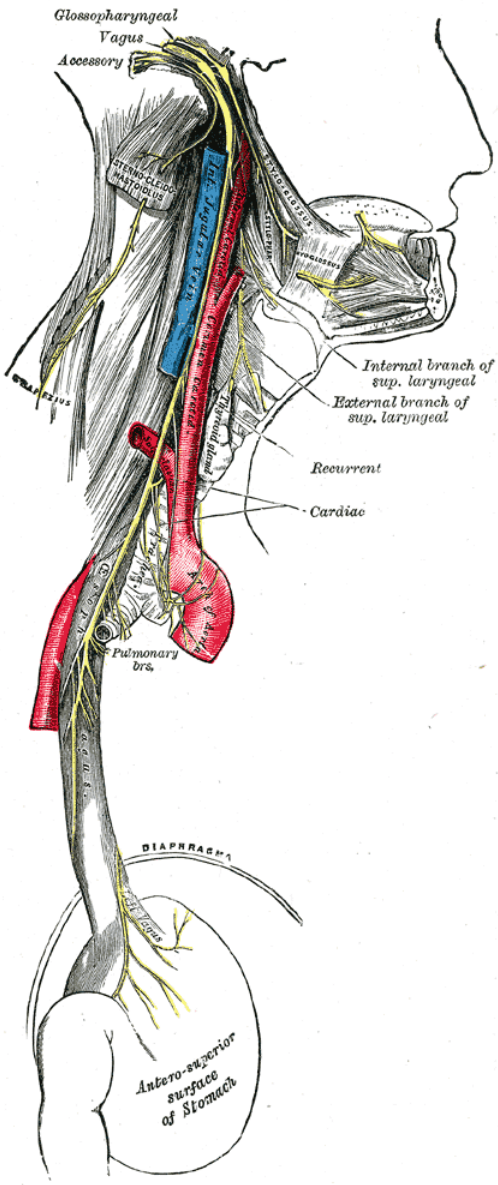

Figure 1.6: The vagus nerve. Reprinted from *Gray's Anatomy*. This work is in the public domain [1].

erties, and thus its tension is completely controlled by the vocal fold length. The inner group, the body, is composed of the deep layers of the lamina propria and the thyroarytenoid muscle. Its tension is not only determined by length but also by the active contractile properties of the thyroarytenoid muscle. Thus activation of the thyroarytenoid muscle can shorten the vocal folds but still cause an increase in f_0 due to an increase in internal stiffness of the muscle fibers.

A simple rod model, proposed by Titze [35], of the thyroid and cricoid cartilages with forces acting on them due to laryngeal muscle activation leads to the following expression for fundamental frequency f_0

$$\begin{aligned} f_0 &= f_{0p}\left(1+\frac{A_a}{A}\frac{\sigma_{am}}{\sigma_p}a_{ta}\right)^{\frac{1}{2}} \\ \sigma_p &= 4L_0^2\left(1+\epsilon\right)^2 f_{0p}^2 \\ f_{0p} &= 38+175(\epsilon+1)+2450(\epsilon+1)^2+2p_s \\ \epsilon &= 0.2(1.5a_{ct}-a_{ta}) \end{aligned} \tag{1.1}$$

Here a_{ta} and a_{ct} are the activation percentages of the thyroarytenoid and cricothyroid muscles, f_{0p} is the fundamental frequency for passive tissue (i.e for $a_{ta} = 0$), σ_p is the mean passive stress over the entire vibrating cross section A, σ_{am} is the maximum active stress in the muscular cross section A_a , L_0 is the passive length of the vocal folds, ϵ is the vocal fold strain, ρ is the vocal fold density, and p_s is the subglottal pressure. Titze obtained the numerical constants through experimental data fitting. A plot of f_0 as

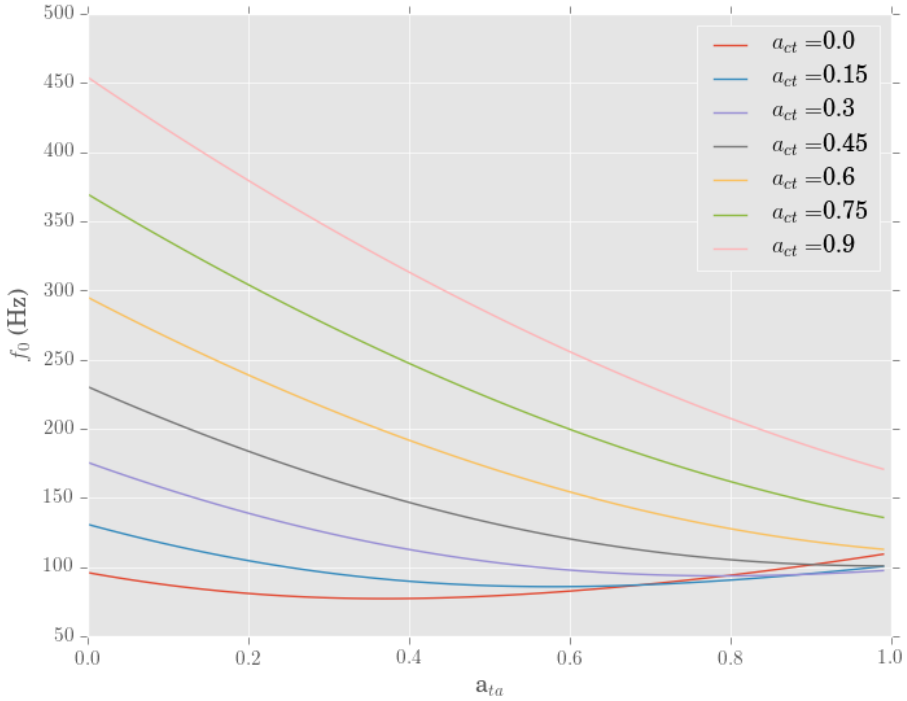

Figure 1.7: Fundamental frequency f_0 plotted against thyroarytenoid muscle activation a_{ta} for different values of cricothyroid muscle activation a_{ct} ($\frac{A}{A_a} = 0.5$ $\sigma_p = 100$ kPa , $p_s = 8$ cm H20, $L_0 = 1.5$ cm). From this figure it can be seen complex modulations of f_0 can be performed through activation of these muscles.

a function of thyroarytenoid and cricothyroid muscle activation can be seen in Fig. 1.7 From the figure it can be seen that complex modulations of fundamental frequency can be obtained through activation of these muscles. Additionally it can be seen that while activation of the cricothyroid muscle usually corresponds to an increase in f_0, activation of the thyroarytenoid muscle can lead to more complicated behavior.

While the body-cover theory can explain variations of fundamental frequency as a result of vocal fold tension and subglottal pressure it is not sufficient to account for the harmonic content of vocalizations and their transient time behavior. To account for these complexities time domain oscillator models of the vocal folds must be considered. Fig. 1.8 shows a single mass model for the vocal folds. In his 1998 paper, Titze derived an equation that describes the small amplitude oscillations of a single mass model of the vocal folds [18].

$$\begin{aligned} m\ddot{x} + b\dot{x} + kx &= p_g \\ p_g &= p_s + (p_s - p_i)\left(1 - \frac{a_2}{a_1} - k_e\right)/k_t \\ a_1 &= 2L(x_{01} + x + \frac{T}{2c}\dot{x}) \\ a_2 &= 2L(x_{02} + x - \frac{T}{2c}\dot{x}) \end{aligned} \tag{1.2}$$

where x is the displacement of the vocal folds from their equilibrium position, m is their mass per unit area, b is the coefficient of linear dissipation per unit area, k is the restoration constant per unit area, p_g is the intraglottal pressure, p_s is the subglottal pressure, p_i is the superglottal pressure, a_1 is the inferior area of the vocal folds, a_2 is the superior area of the vocal folds, k_e is the pressure recover coefficient for the turbulent expansion region above the vocal folds, k_t is the transglottal pressure coefficient, L is the axial length of the vocal folds, T is their traverse thickness, c is the speed of sound, lastly x_{01} and x_{02} are the equilibrium displacements of the inferior and superior portions of

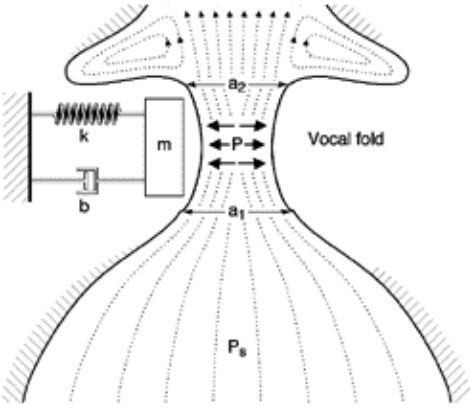

Figure 1.8: Single mass model of the vocal folds [2]. Reprinted with permission

the vocal folds respectively. Since the harmonic content of an acoustic wave in the vocal tract is determined by the oscillations of the vocal folds, the time course of a vocalization can be described using this model as a function of physiological parameters. The strength of the forcing is determined by the subglottal pressure p_s and the glottal areas a_1 and a_2. The fundamental frequency $f_0 = \frac{1}{2\pi}\sqrt{\frac{k}{m}}$ can be calculated using the body cover model and is thus determined by vocal fold tension and subglottal pressure. In addition, the effects of the upper vocal tract can be taken into account by the pressure p_i.

While Titze's equations are successful in accounting for the transfer of kinetic energy of air into vocal fold oscillations, they are only valid for small displacements from the vocal folds' equilibrium positions. Several attempts have been made to introduce nonlinearities into these oscillator equations.

The nonlinearities model the loss of energy due to collision of the vocal folds upon large deviations from their equilibrium positions. They have the affect of keeping solutions bounded and introducing harmonic content not accounted for by the fundamental frequency. One of the simpler, yet feature rich, attempts has been proposed by Magnasco et al. to model oscillations of vocal folds in bird syrinxes [3]. The Magnasco model basically consists of the Titze model with the introduction of a nonlinearity cubic in the vocal fold velocity.

$$m\ddot{x} + b\dot{x} + \beta\dot{x}^3 + kx = p_s \frac{a_0 - b_0 + 2\tau\dot{x}}{x + b_0 + 2\tau\dot{x}}, \tag{1.3}$$

where here τ is treated as phenomenological constant. The Magnasco model predicts that the onset of vocal fold oscillations occurs through a Hopf bifurcation, which can be achieved by varying the subglottal pressure p_s and vocal fold stiffness k (Fig. 1.10). Furthermore, the model was able to qualitatively reproduce the features of actual canary songs through simple modulations of these parameters .

1.5 The Failure of Vibrating Vocal Fold Models for Ultrasonic Vocalizations

The frequency of sonic mammalian vocalizations scales with species mass, according to a power law, over several orders of magnitude of size. This can be seen in Fig. 1.11. The dashed line in the figure is a scaling law proposed

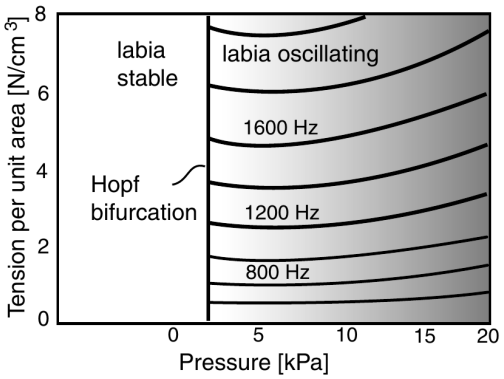

Figure 1.9: Bifurcation diagram for Eq. 1.3. The system is brought in an out of a state of self-oscillation through a Hopf bifurcation by varying the parameters k and p_s (reprinted with permission) [3].

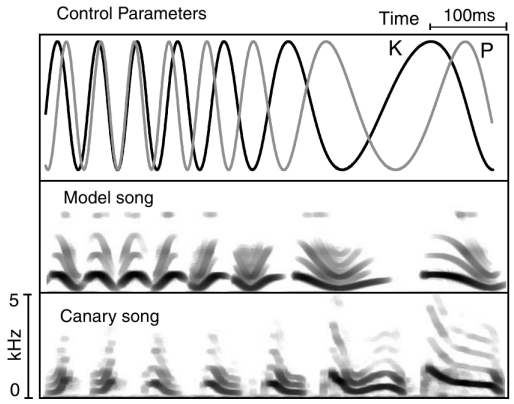

Figure 1.10: Qualitative features of canary song reproduced through simple variations of the parameters k and p_s (reprinted with permission) [3].

by Bradbury and Vehrenkamp [36]. They reasoned that call frequency should be proportional to the inverse of the linear scale of an animal, $f \propto L^{-1}$. Since L is proportional the cube of the mass M of the animal $f \propto M^{-3}$. It can be seen that while this scaling law does fit the general trend of the sonic data (purple boxes) agreement is not perfect.

A more accurate scaling law (the solid line) was derived by Fletcher by considering the optimal call frequency for an animal to make when it is a given distance away from a conspecific [4]. If A_v is the amplitude of oscillation of the vocal fold area, then from Bernoulli's law the amplitude of oscillation of the velocity of airflow through the vocal folds is given by

$$U = \left(\frac{2p}{\rho}\right)^{\frac{1}{2}} A_v, \tag{1.4}$$

where p is lung pressure and ρ is the density of air. The vocal folds can be though of as a circular aperture set in an infinite plane baffle. The effect of this is to ensure sound only radiates off into infinity in one direction and does not travel backwards. The acoustic power radiated as a function of frequency f is then given by

$$P = \frac{\pi \rho f^2 U^2}{2c}, \tag{1.5}$$

where c is the speed of sound in air. Sound amplitude decreases with distance according to an inverse square law. In addition, intensity decreases due to atmospheric absorption. Combining these effects the sound intensity as a

function of distance from its source is given by

$$I(r) = \frac{P}{4\pi r^2} e^{-\alpha f^{1.5} r}, \tag{1.6}$$

where $\alpha = 3.6 \times 10^{-8} m^{-1} Hz^{-1.5}$ is constant that takes into the account the effects of atmospheric absorption. The acoustic signal provided to the cochlea of a listening conspecific a distance r from the vocalizer is given by

$$S(r) = I(r) A_E, \tag{1.7}$$

where A_E is the cross-sectional area of the outer ear. Combings Eqs. 1.5, 1.6, and 1.7,

$$S(r) = \frac{p f^2 A_V^2 A_E}{4cr^2} e^{-\alpha f^{1.5} r}. \tag{1.8}$$

It is required that $S(r) \geq T$ for the signal to be audible by a conspecific at a distance r from the source, where T is a threshold value that does not vary much between species. From Eq. 1.8 it can be seen the amplitude of the signal received at a distance r varies as a function of frequency. To find the optimal frequency f^* for communicating at range r^* it is required that $\frac{\partial r}{\partial f} = 0$ with $S(r^*) = T$. The optimization condition is satisfied when $\alpha f^n r = \frac{2}{n}$. Substituting this back into Eq. 1.8 and solving for f^*,

$$f^* = \left(\frac{16cT}{\alpha^2 n^2 A_V^2 A_E p} \right)^{\frac{1}{2n+2}} \tag{1.9}$$

Assuming the mouth and ear diameters are proportional to the linear body dimension L gives the result $f^* \propto L^{-\frac{3}{n+1}}$. Since the animal's mass is proportional to L^3 this is equivalent to saying $f^* M^{-\frac{1}{n+1}}$. For the approximate value of $n = 1.5$, this becomes $f^* \propto M^{-0.4}$. It can be seen the solid line fits the data for sonic vocalization very well across several orders of magnitude of size, indicating the same mechanisms for vocal production and audition are used throughout different species of mammals. However, it is also quite apparent that the data for ultrasonic vocalizations (green boxes) completely diverge from the scaling law. This is indicative of the fact the mechanisms for USVs are fundamentally different from that for sonic vocalizations.

In 1975 Roberts presented the first evidence that indicated vibrating vocal fold models were insufficient to describe USVs [37]. In the study he placed young rats in a polyethylene bag and recorded both their sonic and ultrasonic vocalizations when the bag was filled with air. He then replaced the air with a heliox gas mixture of 20% oxygen and 80% helium. The effect of this is to increase the speed of sound in the bag by a factor of 1.7. For the sonic vocalizations he observed that although the higher harmonics increased in frequency the fundamental frequency remained constant. This is consistent with the vibrating fold model, since the harmonic content will be determined by resonance properties of the vocal tract, but the fundamental frequency will be determined by the oscillations of the vocal folds. However, for ultrasonic vocalizations he observed an increase in fundamental frequency when air was replaced with heliox gas. In 2011 Riede performed a more sophis-

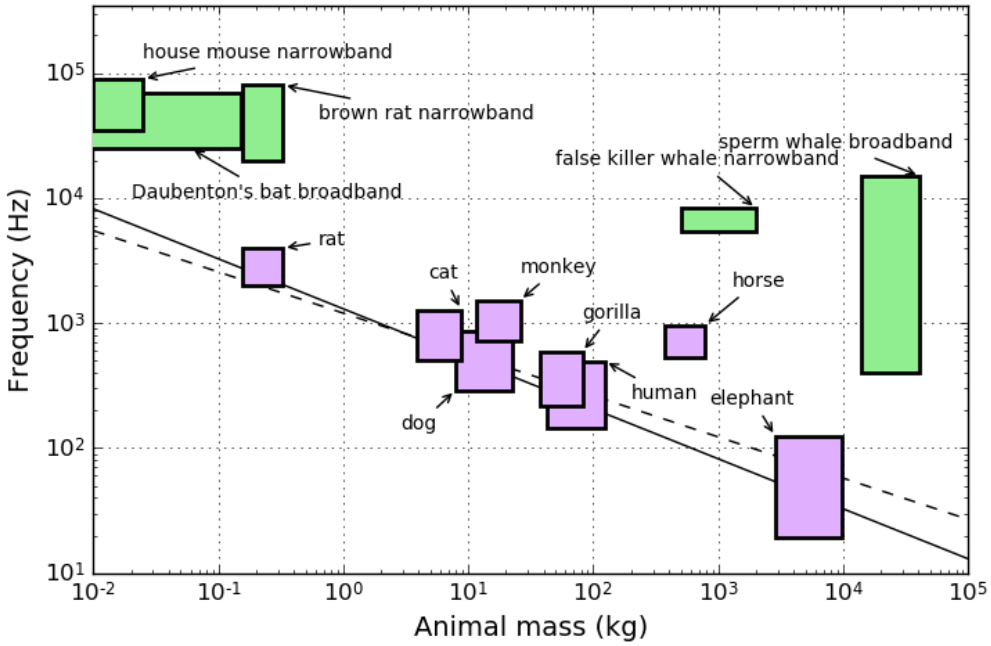

Figure 1.11: Frequency scaling for mammals across several magnitudes of size (adapted from [4]). The purple boxes show the ranges of audible frequencies emitted by several mammals plotted against the ranges of their masses. The solid and dashed lines show plots of a frequency scaling law of the form $f \propto M^{-\alpha}$. The dashed line ($\alpha = \frac{1}{3}$) is based on the conjecture that the average frequency emitted in audible vocalizations should be inversely proportional to the linear scale of the animal. The solid line ($\alpha = 0.4$) is based on more in depth acoustic analysis to find the most efficient vocalization frequency for an animal of a given size. The green boxes show the range of ultrasonic frequencies emitted by several mammalian species plotted against their masses. These vocalizations do not obey the scaling laws [5, 6, 7, 8, 9, 10, 11, 12, 13, 14].

ticated version of this experiment [38]. He inserted a metal tube into the trachea of several rats. The tube was capable of measuring subglottal pressure and injecting gas into the trachea. He injected a heliox mixture into the trachea of rats mid 22-kHZ vocalization and found an increase in fundamental frequency. Furthermore, he found the fundamental frequency increased in proportion to the amount of heliox gas present.This is inconsistent with a vibrating vocal fold model and indicates the source of oscillation is aerodynamic rather than physical in nature, since the fundamental frequency of an aerodynamic oscillator will be determined by the speed of sound in the gas. Riede has also provided evidence that the rat vocal folds cannot sustain oscillations at a high enough frequency to produce vocalizations in the ultrasonic range. He found that at frequencies of vibration higher than 4 kHz the strain experienced by the vocal folds starts to cause permanent damage to the lamina propia and epithelium [39]. This evidence together has led to the consensus that vibrating vocal folds cannot be the source of rodent ultrasonic whistles.

Although there has been sufficient work to discount vibrating vocal folds as the source of rodent USVs, there has been little positive evidence as to how these vocalizations are actually produced. Roberts was able to artificially generate sounds that are qualitatively similar to rat USVs using a hole tone apparatus, which consisted of two metal plates with axially aligned holes drilled in them (Fig. 3.3). The plates were spaced a distance of 1.5 mm apart and a steady air flow was forced through the holes [37]. In a hole tone,

air forced through the first hole forms a jet. Velocity perturbations to the jet, of different frequencies, destabilize and grow in amplitude. The geometry of the jet will determine a preferred frequency which will dominate the others. Perturbations of this frequency will force air harmonically through the downstream aperture, determining the frequency of sound that is emitted. Although Roberts was able to generate sounds similar to rat USVs, this is far from conclusive evidence that it is the mechanism used by rats to generate these vocalizations. His reasoning for favoring this mechanism that both the hole tone and rat USVs exhibit frequency jumps. However, many acoustic systems will display frequency jumps, and many acoustic systems will have similar sounding properties. Furthermore, although it is likely that the orifice formed by the vocal folds acts as the upstream aperture in the hole tone, there is no known anatomical feature which would correspond to the downstream aperture. In addition, this mechanism does not take into the resonance frequencies of the upper vocal tract. The upper vocal tract for an adult rat has been measured to be approximately $L = 4$ mm [40]. If the upper vocal tract is thought of as a half open pipe then its fundamental frequency is given by $f_0 = \frac{c}{4L} \approx 21.4kHz$. Thus if there is any driving mechanism in that frequency range it would likely excite these resonances. In a later chapter further evidence will be presented that shows a hole tone model is insufficient to explain the USV production mechanism.

Sanders et al. have provided another piece of positive evidence for the mechanism of rat USVs [15]. He inserted a camera into the mouth of an anes-

thetized rat and stimulated production of a USV by electrical stimulation of the periaqueductal gray (PAG) region of the brain stem. He observed the vocal folds to tense up at the beginning of a vocalization and to remain at approximately a constant distance apart throughout stimulation, even when the call exhibits a frequency jump. Fig. 1.12 summarizes the results of his experiment This indicates that mechanism likely consists of a jet of air emerging from the vocal folds and somehow exciting the resonance frequencies of the upper vocal tract. Furthermore, it indicates vocal fold separation is not the physiological variables responsible for frequency modulation and frequency jumps. Some other quantity, probably subglottal pressure, must control this behavior.

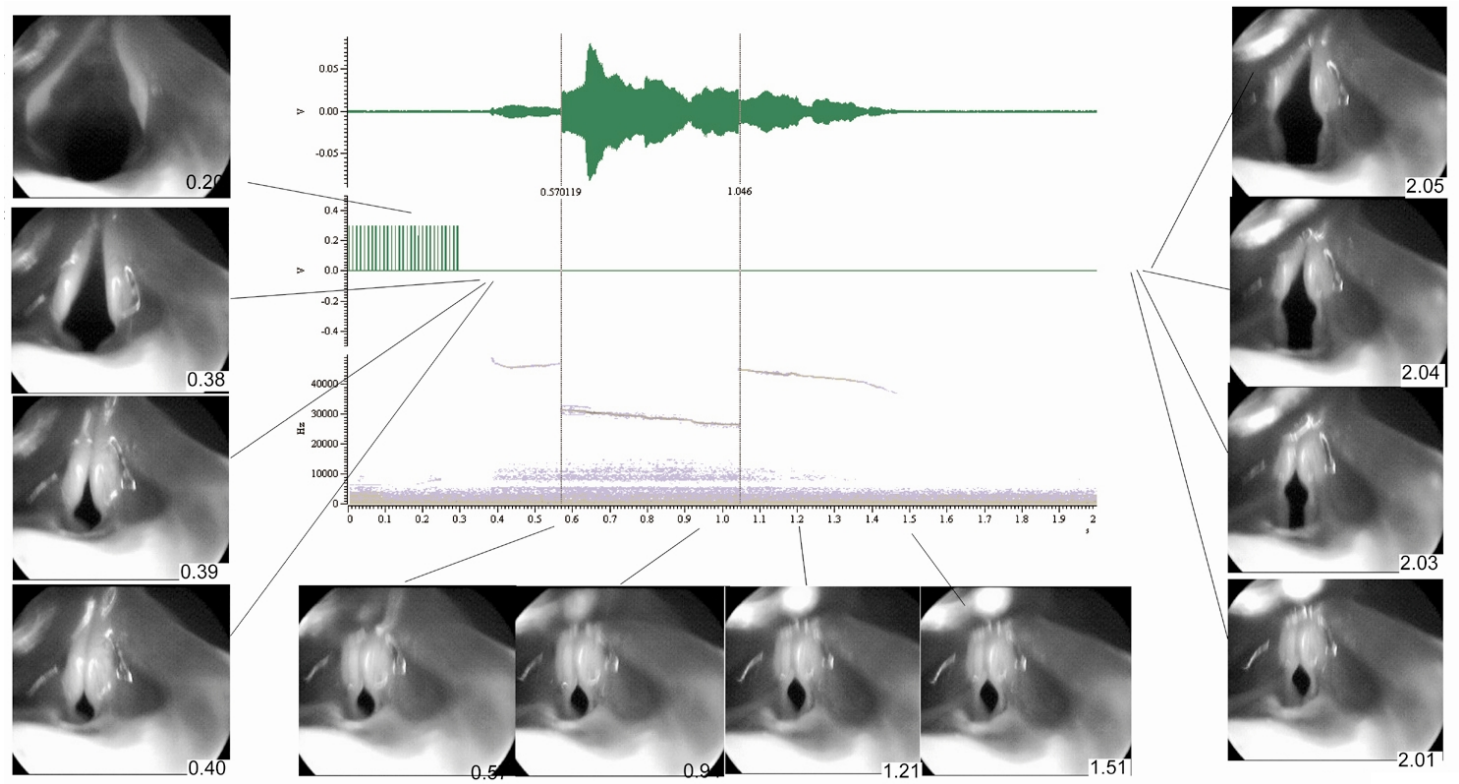

Figure 1.12: The photographs show the vocal folds of an anesthetized rat before, during, and after a vocalization was forced through stimulation of the PAG region of the brainstem. The top plot shows the acoustic signal recorded by a microphone. The middle plot shows the electrical pulses used to stimulate vocalization, and the bottom plot shows the spectrogram of the acoustic signal. From the photographs it can be seen the vocal folds tense up to form a small aperture through which air is forced by the lungs. The size of the aperture does not vary throughout the course of the vocalization, even through the discontinuous frequency jumps (reprinted with permission) [15].

Chapter 2

Fluid Mechanics and Acoustics Background

2.1 Introduction

It is the goal of this thesis to be accessible to researchers who are not experts in fluid dynamics. It is also a goal to emphasize that the time domain model of later chapters is as much a derivation from first principles as possible. Hence, in this chapter some important concepts and results from fluid dynamics and acoustics will be reviewed. These concepts will be used later on in deriving a description of the rat vocal tract. Discussions similar to these can be found in Batchelor [41] and Howe [42].

2.2 Conservation Laws

The state of a fluid at time t and position $\mathbf{x}$ is determined by its velocity field $\mathbf{v}(\mathbf{x}, t)$ and any two thermodynamic variables. Common choices for these thermodynamic variables are the pressure field $p(\mathbf{x}, t)$, density field $\rho(\mathbf{x}, t)$, or temperature field $T(\mathbf{x}, t)$. Thus, five scalar equations are needed to specify the equations of motion for the fluid. This section reviews the derivation of these equations by applying conservation of mass, momentum, and energy to the motion of a fluid.

2.2.1 Mass Conservation

The first equation of motion is a statement of conservation of mass. To derive it the total mass in a volume V is considered. The mass can be expressed as a volume integral of the fluid density

$$M = \int_V \rho dV. \tag{2.1}$$

Considering an infinitesimal element $d\mathbf{S}$ of the volume's enclosing surface S, the net flux of mass through that infinitesimal element is $\rho\mathbf{v} \cdot d\mathbf{S}$. Thus the total flux of mass through S is given by the surface integral of that quantity.

$$\Phi_M = \int_S \rho\mathbf{v} \cdot d\mathbf{S}. \tag{2.2}$$

Conservation of mass states that the time rate of change of the mass in V plus the net flux through S must equal 0.

$$\frac{dM}{dt} + \Phi_M = 0 \tag{2.3}$$

Substituting Eqs. 2.1 and 2.2 into 2.3,

$$\int_V \frac{\partial \rho}{\partial t} dV + \int_S \rho \mathbf{v} \cdot d\mathbf{S} = 0. \tag{2.4}$$

Now using the divergence theorem on the second integral this equation can be expressed as

$$\int_V \left(\frac{\partial \rho}{\partial t} + \nabla \cdot (\rho \mathbf{v}) \right) dV = 0. \tag{2.5}$$

This equation must be true for all volumes V. Thus, the integrand must be equal to 0, and the equation of fluid continuity is obtained [41].

$$\frac{\partial \rho}{\partial t} + \nabla \cdot (\rho \mathbf{v}) = 0. \tag{2.6}$$

2.2.2 Energy Conservation

For general fluid dynamics problems, especially ones in which there is significant heat conduction due to temperature gradients, the full energy transport equation must be used to describe the spatial and temporal evolution of energy distributions in the system. However, this work is mostly concerned with the flow of air in the rodent vocal tract. Rats complete a full respi-

ration cycle approximately eight times per second. Thus, it is not a bad approximation to neglect heat conduction and assume the specific entropy s is constant and uniform throughout the fluid. This simplifies the analysis greatly by allowing the assumption that the fluid's pressure and density are related by a constitutive equation of the form

$$p = p(\rho, s). \tag{2.7}$$

Often times simply assuming the fluid to be an ideal gas is sufficient. The constitutive equation for an adiabatic ideal gas is

$$p = constant \times \rho^{\gamma}, \tag{2.8}$$

where γ is the ratio of the constant pressure specific heat to the constant volume specific heat of the gas. For the purposes of this analysis an even simpler relation will be use. Since this work is concerned with the production of sound, the fact that acoustic flow consists of small perturbations from a mean flow can be used to derive a constitutive equation. This relation is discussed more in the section on acoustic flow [42].

2.2.3 Momentum Conservation

The momentum conservation equation comes from similar considerations as mass conservation. An expression for the net momentum in a volume V will

be derived, and then its time rate of change will be related to the net flux of momentum through the volume's enclosing surface S. This process will be made somewhat more complicated by the fact that momentum is a vector quantity. This just means that a conservation law must be derived for each component of the momentum vector. The i^{th} component of the total linear momentum in volume V is given by

$$P_i = \int_V \rho v_i dV \tag{2.9}$$

Furthermore the rate at which momentum flows through the infinitesimal area $d\mathbf{S}$ is given by $\rho\mathbf{v}(\mathbf{v} \cdot d\mathbf{S})$. Integrating the i^{th} component of this vector over S gives the total flux of the i^{th} momentum component through the surface.

$$\Phi_i = \int_S \rho v_i v_j dS_j, \tag{2.10}$$

where summations are carried out over repeated indices. Finally, an expression for the net force on V is required. The i^{th} component of that force is given by

$$f_i = \int_V F_i dV + \int_S \sigma_{ij} dS_j, \tag{2.11}$$

where the left integral is the total contribution from body forces, such as gravity. The right integral is the total contribution from surface forces, such as those arising in shear flow. The matrix σ_{ij} is the stress tensor, which will be discussed more later. Conservation of momentum and Newton's second

law states that the time rate of change of momentum inside V plus the flux of momentum through S must equal the net force on V.

$$\frac{dP_i}{dt} + \Phi_i = f_i. \tag{2.12}$$

Inserting Eqs. 2.9, 2.10, and 2.11 into Eq. 2.12,

$$\int_V \frac{\partial(\rho v_i)}{\partial t} dV + \int_S \rho v_i v_j dS_j = \int_V F_i dV + \int_S \sigma_{ij} dS_j. \tag{2.13}$$

Now the divergence theorem can be used to convert the surface integrals into volume integrals.

$$\int_V \left(\frac{\partial(\rho v_i)}{\partial t} + \frac{\partial(\rho v_i v_j)}{\partial x_j} \right) dV = \int_V \left(F_i + \frac{\partial \sigma_{ij}}{\partial x_j} \right) dV. \tag{2.14}$$

Again this equation must be valid for arbitrary volumes V, so the integrands must equal each other.

$$\frac{\partial(\rho v_i)}{\partial t} + \frac{\partial(\rho v_i v_j)}{\partial x} = F_i + \frac{\partial \sigma_{ij}}{\partial x}. \tag{2.15}$$

Expanding the derivatives and rearranging the terms of this equation,

$$\left(\frac{\partial \rho}{\partial t} + v_j \frac{\partial \rho}{\partial x_j} + \rho \frac{\partial v_j}{\partial x_j} \right) v_i + \rho \left(\frac{\partial v_i}{\partial t} + v_j \frac{\partial v_i}{\partial x_j} \right) = F_i + \frac{\partial \sigma_{ij}}{\partial x_j}. \tag{2.16}$$

Now combining it with the continuity equation in tensor form,

$$\frac{\partial \rho}{\partial t} + v_j \frac{\partial \rho}{\partial x_j} + \rho \frac{\partial v_j}{\partial x_j} = 0. \tag{2.17}$$

The derivatives of density can be eliminated to obtain the equation of fluid motion.

$$\rho \left(\frac{\partial v_i}{\partial t} + v_j \frac{\partial v_i}{\partial x_j} \right) = F_i + \frac{\partial \sigma_{ij}}{\partial x_j}. \tag{2.18}$$

This can be expressed as

$$\frac{Dv_i}{Dt} = \frac{F_i}{\rho} + \frac{1}{\rho} \frac{\partial \sigma_{ij}}{\partial x_j}, \tag{2.19}$$

where

$$\frac{D}{Dt} = \frac{\partial}{\partial t} + v_j \frac{\partial}{\partial x_j} \tag{2.20}$$

is known as the convective derivative [41].

2.3 The Stress Tensor

The stress tensor σ_{ij} appearing in Eq. 2.19 represents the surface forces due to shearing of the fluid. Some additional assumptions can be introduced to relate σ_{ij} to the gradients of fluid velocity. This will allow the derivation of the infamous Navier-Stokes equation. This section discusses those additional assumptions and some general properties of the stress tensor.

2.3.1 Symmetry of the Stress Tensor

In this subsection an expression for the torque on a fluid of volume V will be derived. Once this is accomplished it can be shown that the stress tensor must be symmetric. The i^{th} component of the torque about the origin O from a body force on an infinitesimal volume element dV inside of V is $\varepsilon_{ijk}x_jF_kdV$. Similarly the i^{th} component of torque on an infinitesimal area element $d\mathbf{S}$ of the surface S is $\varepsilon_{ijk}x_j\sigma_{kl}dS_l$. In these expressions ε_{ijk} is the Levi-Civita tensor and is defined by

$$\varepsilon_{ijk} = \begin{cases} 1 & \text{i,j,k is an even permutation of 1,2,3} \\ -1 & \text{i,j,k is an odd permutation of 1,2,3} \\ 0 & \text{otherwise} \end{cases} \tag{2.21}$$

Integrating the first expression over V and the second over S an expression for the total torque on V about O is obtained.

$$\tau_i = \int_V \varepsilon_{ijk}x_jF_kdV + \int_S \varepsilon_{ijk}x_j\sigma_{kl}dS_l. \tag{2.22}$$

Using the divergence theorem to turn the area integral into a volume integral,

$$\tau_i = \int_V \varepsilon_{ijk}x_jF_kdV + \int_V \varepsilon_{ijk}\frac{\partial(x_j\sigma_{kl})}{\partial x_l}dV. \tag{2.23}$$

Now expanding the derivative in the second integral, this becomes

$$\tau_i = \int_V \varepsilon_{ijk} x_j F_k dV + \int_V \varepsilon_{ijk} \sigma_{kj} dV + \int_V \varepsilon_{ijk} x_j \frac{\partial \sigma_{kl}}{\partial x_l} dV. \tag{2.24}$$

Now it will be assumed the point O lies within V, and the volume will be allowed to tend to 0. If the volume is sufficiently small, then F_i, σ_{ij}, and $\frac{\partial \sigma_{ij}}{\partial x_j}$ will not vary significantly over the region of integration. From this it can be concluded the first, second, and third integrals in the above equation will scale as $V^{4/3}$, V, and $V^{4/3}$ respectively (since $x_j \propto V^{1/3}$). From Newton's second law for rotational motion, the time rate of change of angular momentum of the fluid volume must equal the torque applied to it. However, the rate of change of angular momentum should scale as $V^{4/3}$, since the net linear acceleration scales as V, and the rate of change of angular momentum scales as xV. This is inconsistent with the above result, which shows that the rate of change of angular momentum will be dominated by the second integral in the above equation, since it scales as V. The only way to resolve this inconsistency is for the second integral to be identically 0 for all choices of O and V. This is only possibly if

$$\varepsilon_{ijk} \sigma_{kj} = 0, \tag{2.25}$$

which implies that stress tensor must be symmetric [41]

$$\sigma_{ij} = \sigma_{ji}. \tag{2.26}$$

2.3.2 The Stress Tensor in a Static Fluid

It is a well known result from linear algebra that a symmetric matrix can be diagonalized by expressing its entries in a rotated coordinate system. The axes of this coordinate system are called the principle axes. Thus, from the result of the previous section a set of principle axes can be chosen to diagonalize the stress tensor at a single point in space. The diagonal elements of the rotated stress tensor will be referred to as σ'_{11}, σ'_{22}, and σ'_{33}. It is another well known result from linear algebra that the sum of the diagonals of a matrix is invariant under a change of basis. Thus, the trace of the stress tensor at the point in space can be expressed as

$$\sigma_{ii} = \sigma'_{11} + \sigma'_{22} + \sigma'_{33}, \tag{2.27}$$

regardless of the chosen basis.

Now consider the surface forces acting on an infinitesimal cubic volume in a static fluid. The cube is small enough such that the entries of the stress do not vary significantly throughout its volume. The cube can also be chosen so its sides are aligned parallel to the principle axes of the stress tensor, which will ensure its off diagonal elements are 0. Then the stress tensor can be

expressed as the sum of two matrices.

$$\boldsymbol{\sigma} = \begin{pmatrix} \frac{\sigma_{ii}}{3} & 0 & 0 \\ 0 & \frac{\sigma_{ii}}{3} & 0 \\ 0 & 0 & \frac{\sigma_{ii}}{3} \end{pmatrix} + \begin{pmatrix} \sigma'_{11} - \frac{\sigma_{ii}}{3} & 0 & 0 \\ 0 & \sigma'_{22} - \frac{\sigma_{ii}}{3} & 0 \\ 0 & 0 & \sigma'_{33} - \frac{\sigma_{ii}}{3} \end{pmatrix} \tag{2.28}$$

By definition $Tr(\boldsymbol{\sigma}) = \sigma_{ii}$, which by construction also equals the trace of the first matrix on the right hand side. Thus the trace of second matrix must be 0. From that it can be concluded that there are forces compressing the fluid volume in the direction of two principle axes and one force tensioning the fluid volume in the direction of the other axis. This force distribution has the tendency to elongate and deform the volume. These forces cannot be balanced out by internal volume forces, since volume forces tend to 0 faster than surfaces as the volume goes to 0. This presents an inconsistency, since a fluid is defined as a material that is incapable of withstanding a tendency of applied forces to change its shape. It follows that the diagonal components of the second matrix must all be 0. Therefore the principle stresses must all be equal to $\frac{\sigma_{ii}}{3}$. The static fluid pressure is defined as $p = -\frac{\sigma_{ii}}{3}$. Thus,

$$\sigma_{ij} = -p\delta_{ij}. \tag{2.29}$$

The stress tensor in a static fluid then has the interpretation of isotropically compressing all fluid volumes with force per unit area equal to the static pressure [41].

2.3.3 The Stress Tensor in a Moving Fluid

In a moving fluid there a shear forces in addition to the normal forces from the static pressure. To account for these shear forces the stress tensor is expressed as the sum of the static fluid part and a non-isotropic part which accounts for shear forces that arise from the fluid motion.

$$\sigma_{ij} = -p\delta_{ij} + d_{ij} \tag{2.30}$$

The tensor d_{ij} is called the deviatoric stress tensor. It is symmetric, since σ_{ij} must be symmetric. In addition, it has trace equal to 0, since the trace of $\boldsymbol{\sigma}$ must equal the sum of the normal stresses. Furthermore, the deviatoric stress cannot depend on the absolute velocity of the fluid. Since for a fluid traveling at constant velocity an inertial frame of reference can always be transformed to one comoving with the fluid, and this transformation should not affect the stresses present in the fluid. Therefore, it is reasonable to assume d_{ij} depends on gradients of fluid velocity. The simplest assumption for such a tensor is one for which it is a linear function of the velocity gradients.

$$d_{ij} = A_{ijkl}\frac{\partial v_k}{\partial x_l}. \tag{2.31}$$

Fluids that obey such a tensor relationship are known as Newtonian fluids. Although many fluids deviate from this assumption it will be more than sufficient for the purposes of this thesis. It is also common to assume the

fluid is isotropic, meaning the fluid has the same properties in all directions. For an isotropic fluid it is reasonable to expect the fourth order tensor A_{ijkl} is isotropic. Thus any anisotropy in d_{ij} is a result of the velocity gradients. The most general expression for an isotropic fourth order tensor is

$$A_{ijkl} = \mu\delta_{ij}\delta_{kl} + \mu'\delta_{ik}\delta_{jl} + \mu''\delta_{il}\delta_{jk} \tag{2.32}$$

Thus,

$$d_{ij} = \mu\frac{\partial v_k}{\partial x_k} + \mu'\frac{\partial v_i}{\partial x_j} + \mu''\frac{\partial v_j}{\partial x_i} \tag{2.33}$$

However, d_{ij} must also be symmetric and traceless which means $\mu' = \mu''$ and $3\mu = -2\mu'$. Therefore the deviatoric part of the stress tensor can be expressed as

$$d_{ij} = 2\mu\left(e_{ij} - \frac{1}{3}e_{kk}\delta_{ij}\right), \tag{2.34}$$

where

$$e_{ij} = \frac{1}{2}\left(\frac{\partial v_i}{\partial x_k} + \frac{\partial v_j}{\partial x_i}\right). \tag{2.35}$$

The quantity e_{ij} is known as the rate of strain tensor and the quantity μ has the interpretation of being the viscosity of the fluid [41].

2.4 The Navier-Stokes and Euler Equations

The momentum transport equation can be used in combination with the expression for the stress tensor in terms of the velocity gradients to obtain

the equation of motion for a isotropic, Newtonian, classical fluid. Combining Eqs. 2.19, 2.30, 2.34, and 2.35,

$$\rho \frac{Dv_i}{Dt} = F_i - \frac{\partial p}{\partial x_i} + \mu \left(\frac{\partial^2 v_i}{\partial x_j^2} + \frac{1}{3} \frac{\partial^2 v_j}{\partial x_i x_j} \right). \tag{2.36}$$

Writing this in vector form it becomes

$$\rho \frac{D\mathbf{v}}{Dt} = \mathbf{F} - \nabla p + \mu \left(\nabla^2 \mathbf{v} + \frac{1}{3} \nabla (\nabla \cdot \mathbf{v}) \right). \tag{2.37}$$

This is the Navier-Stokes equation [41]. Its three components, along with the continuity equation (Eq. 2.6), and a constitutive equation of the form Eq. 2.7 give the five equations of motion necessary to solve for the three velocity components v_i, the pressure p, and the density ρ for Newtonian homentropic flow in an isotropic fluid. In general this is a very difficult task and much work is done performing direct numerical simulations of these equations. In practice it is generally not necessary to use the equations of motion in their full form, and additional simplifying assumptions can be introduced. In the following sections the special types of flow used to model the rodent vocal tract will be discussed.

The first simplifying assumption is the neglecting of viscosity. In the Navier-Stokes equation, for flows with Reynold's numbers much greater than unity, the inertial terms become much greater than viscous terms. This allows one to neglect viscosity. The rat vocal folds have a radius of approximately $r = 1$ mm, and the flow through them has velocities on the order $U = 30 \frac{m}{s}$.

Thus, the Reynold's number, $Re = \frac{rU}{\nu}$, (where ν is the kinematic viscosity of air) of this flow is on the order of 2000. Therefore, viscosity will be neglected in much of the analysis of this flow. The equation of motion for inviscid flow is called the Euler equation [41].

$$\rho \frac{D\mathbf{v}}{Dt} = \mathbf{F} - \nabla p. \tag{2.38}$$

2.5 Linear Acoustic Flow

2.5.1 Introduction

This type of flow models the propagation of sound in an inviscid fluid. In later chapters, this type of flow will be used to model the the acoustics of the rodent upper vocal tract. The flows linear nature comes from the fact that it consists of small fluctuations superimposed on a quasi-steady mean flow. The decibel scale is helpful in understanding the magnitude of these fluctuations. The decibel value of a sound is calculated using the expression

$$20 \log_{10} \left(\frac{|p|}{p_{ref}} \right), \tag{2.39}$$

where the reference pressure $p_{ref} = 10^{-5} \frac{N}{m^2}$. An acoustic perturbation of $p = 1$ atm has an intensity of about 194 dB, which is deafening. Gauge pressure in the lungs of a rat during vocalization is between 1 and 1.5 kPa [38]. This is approximately 0.01 atm. Thus for flow through the rodent vocal

tract, it is a good approximation to consider linear perturbations from the mean flow.

2.5.2 The Acoustic Wave Equation

The acoustic wave equation will be derived in this section. To do so the pressure, density, and velocity can be written as the sum of a mean and small fluctuating component.

$$p = p_0 + p', \quad \mathbf{v} = \mathbf{v}_0 + \mathbf{v}', \quad \rho = \rho_0 + \rho' \tag{2.40}$$

The acoustic wave equation is a partial differential equation that describes the temporal and spatial evolution of these quantities. To derive an equation of motion for the perturbation quantities these assumptions are inserted into Eqs. 2.38 and 2.6,

$$\begin{aligned} \rho_0 \frac{\partial \mathbf{v}'}{\partial t} + \nabla p' &= \mathbf{F} \\ \frac{1}{\rho_0} \frac{\partial \rho'}{\partial t} + \nabla \cdot \mathbf{v}' &= q, \end{aligned} \tag{2.41}$$

In this step, products of primed quantities have been neglected. Since $\frac{v'}{v_0} \ll 1$, $\frac{p'}{p_0} \ll 1$, and $\frac{\rho'}{\rho_0} \ll 1$ the products of primed quantities will be even smaller and can be safely neglected. In addition, the fact that mean quantities must also satisfy the equations of motion has been used. The equations for the mean quantities have been subtracted off from the equations for the full

quantities. Lastly, a volume source term q has been introduced into the continuity equation to account for changes in fluid volume, which can be a source of sound. Eliminating $\mathbf{v}'$ between the linearized momentum and continuity equations,

$$\frac{\partial^2 \rho'}{\partial t^2} - \nabla^2 p' = \rho_0 \frac{\partial q}{\partial t} - \nabla \cdot \mathbf{F}. \tag{2.42}$$

Now a constitutive relation between p' and ρ' is needed. This relation for the undisturbed and disturbed states can be written

$$\begin{aligned} p_0 &= p(\rho_0, s) \\ p_0 + p' = p(\rho_0 + \rho', s) &\approx p(p_0, s) + \left(\frac{\partial p}{\partial \rho}(\rho, s)\right)_0 \rho' \end{aligned} \tag{2.43}$$

The derivative in parentheses has dimensions of velocity squared and has the interpretation of being the square speed of sound in the medium c. Inserting this interpretation into the above equations and using the first equation to eliminate p_0 and $p(p_0, s)$ from the second equation a relationship between p' and ρ' is obtained.

$$p' = c^2 \rho'. \tag{2.44}$$

Using this equation to eliminate ρ' from Eq. 2.42 the acoustic wave equation for pressure perturbations driven by volume sources q and body forces $\mathbf{F}$ is obtained.

$$\left(\frac{1}{c^2}\frac{\partial^2}{\partial t^2} - \nabla^2\right) p' = \rho_0 \frac{\partial q}{\partial t} - \nabla \cdot \mathbf{F} \tag{2.45}$$

If there are no body forces (i.e. $\mathbf{F} = 0$), then Eq. 2.41 implies the existence of a velocity potential ϕ' such that

$$\begin{aligned} \mathbf{v}' &= \nabla\phi' \\ p' &= -\rho_0 \frac{\partial \phi'}{\partial t} \end{aligned} \tag{2.46}$$

Acoustic flow is generally irrotational potential flow as long as there are no body forces introducing vorticity. In the upper vocal tract the only body force is gravity, which is negligible compared to other effects of the flow, so the approximation of $\mathbf{F} = 0$ is valid for this situation. Inserting this expression into Eq. 2.45 the acoustic wave equation for the velocity potential is obtained [42].

$$\left(\frac{1}{c^2}\frac{\partial^2}{\partial t^2} - \nabla^2\right)\phi' = -q(\mathbf{x}, t). \tag{2.47}$$

2.6 Acoustic Boundary Value Problems

2.6.1 Formulation of the Boundary Value Problem

The Eq. 2.47 is an initial-boundary value problem, meaning it requires both initial and boundary conditions to specify the solution. The initial conditions do not pose any special difficulty, and usually it is just assumed the system starts from rest ($\frac{\partial}{\partial x}\phi(\mathbf{x}, 0) = 0$). The boundary conditions, on the other hand, require a little more care in formulation. As discussed above the upper rat vocal tract will be modeled as a cylindrical pipe. Furthermore,

only the axial resonance modes are considered. The radial resonance modes only become significant at much higher frequencies than are exhibited in rat USVs. The azimuthal modes, while possibly important, are only excited by azimuthal driving forces and it is worthwhile to explore the axisymmetric system before trying to introduce azimuthal asymmetries. There is also experimental evidence in similar systems that only the axisymmetric modes are important in the production of sound. Chanaud and Powell observed that only axisymmetric modes were unstable enough to produce sound in hole and ring tone systems [43]. With this in mind, only the derivatives in the axial direction are important. Thus, the Laplacian operator reduces to $\nabla^2 \rightarrow \frac{\partial^2}{\partial x^2}$.

The driving force, which excites the resonance frequencies of the pipe, is air emerging from the vocal folds. This driving force will be treated as a pressure source at the origin of the pipe $p(0,t) = p_{src}(t)$. This will be the only driving force in the system so $q(\mathbf{x},t) = 0$. From Eq. 2.46 it is known $p = -\rho_0 \frac{\partial \phi}{\partial t}$. Using this equation the boundary condition at $x = 0$ for Eq. 2.47 can be written as

$$\dot{\phi}(0,t) = -\frac{p_{src}(t)}{\rho}. \tag{2.48}$$

This is an inhomogeneous boundary condition and it is helpful to transform it into a homogeneous boundary condition through a substitution. The substitution,

$$\phi(x,t) = \psi(x,t) + \frac{x-L}{L}\int_0^t \frac{p_{src}(t)}{\rho} dt, \tag{2.49}$$

transforms the inhomogeneous boundary condition into a inhomogeneous

driving term in the wave equation

$$\frac{\partial^2\psi}{\partial x^2} - \frac{1}{c^2}\frac{\partial^2\psi}{\partial t^2} = \frac{x-L}{L}\frac{\dot{p}_{src}}{\rho c^2}$$
$$\dot{\psi}(0,t) = 0 \tag{2.50}$$

The Eqs. 2.50 form an inhomogeneous initial value problem with one boundary condition determined. For the problem to be well posed, it requires a second boundary condition at the end of the pipe. Once the second boundary condition is formulated, the homogeneous version of the problem can be solved in the frequency domain to get a set of spatial eigenfunctions. The solutions of the inhomogeneous problem in the time domain can then be expanded on to the spatial eigenfunctions. This method can account for inhomogeneities and transients due to the pressure driving force. The boundary conditions at the end of the pipe are most easily formulated by transforming the problem to the frequency domain. A transformation to Fourier space is appropriate when studying standing wave solutions and a transformation to Laplace space when studying dissipative solutions. An important later part of the analysis is acoustic radiation from the mouth of the rat. This makes the problem inherently dissipative and suggests a solution in Laplace space. This transformation can effectively be done by assuming a solution of the form

$$\psi(x,t) = \phi_m(x)e^{s_m t}$$
$$s_m = i\omega_m - \alpha_m \tag{2.51}$$

The minus sign in front of α_m indicates the energy of the system is expected to dissipate over time due to radiation. Note if $\alpha_m = 0$ then the system becomes conservative, the eigenfunctions become elements of Fourier space, and the solutions reduce to standing wave solutions. Substituting Eq. 2.51 into the homogeneous form of Eq. 2.50 Helmholtz's equation is obtained [44].

$$\begin{aligned} \frac{\partial^2 \hat{\phi}_m}{\partial x^2} - \frac{s^2}{c^2}\hat{\phi}_m = 0 \\ \hat{\phi}_m(0) = 0 \end{aligned} \tag{2.52}$$

2.6.2 Impedance Boundary Conditions

Now that the problem is formulated in the frequency domain, the idea of impedance boundary conditions can be introduced. The impedance of surface S is defined as

$$Z(\mathbf{x}, \omega) = \frac{\hat{p}(\mathbf{x}, \omega)}{\hat{\mathbf{v}}(\mathbf{x}, \omega) \cdot \mathbf{n}_S(\mathbf{x})}. \tag{2.53}$$

Here $\hat{p}$ and $\hat{\mathbf{v}}$ are the pressure and velocity transformed into the frequency domain, and $\mathbf{n}_S$ is the outward normal vector to the surface S. In general the impedance depends not only on the properties of the surface S but also on the acoustic field passing through it. In this situation the impedance is of limited interest. However, if S is a special type of surface called a locally reacting surface, then $Z(\mathbf{x}, \omega)$ depends only on S and not on the acoustic field passing through it. In this case the impedance becomes very important because it allows the formulation of boundary conditions for the acoustic

field on that surface. Inserting the frequency transformed versions of Eqs. 2.46 into Eq. 2.53 a boundary condition for the acoustic wave equation on the surface S is obtained.

$$s_m \rho \hat{\phi}_m(\mathbf{x}, \omega_m) + Z(\mathbf{x}, \omega_m) \nabla \hat{\phi}_m(\mathbf{x}, \omega_m) \cdot \mathbf{n}_S(\mathbf{x}) = 0. \tag{2.54}$$

In this case S will be the disk that forms the exit of the pipe at $x = L$. In general the impedance of this surface will not depend on the radial or azimuthal coordinates and the boundary condition for Eq. 2.52 at $x = L$ can be written as

$$s_m \rho \hat{\phi}_m(L, \omega_m) + Z(\omega_m) \frac{\partial}{\partial x} \hat{\phi}_m(L, \omega_m) = 0. \tag{2.55}$$

To use this as a boundary condition the specific form of $Z(\omega)$ is required. To calculate this quantity extra assumptions about the flow through the pipe exit are required. In the next section a well known model for the acoustic flow through the exit of a cylindrical pipe is discussed [44].

2.6.3 Calculation of the Mouth Impedance

To calculate the spatial eigenmodes first an expression for the exit impedance $Z(\omega)$ must be derived. This calculation was first done by Rayleigh [45] and then later elaborated on by Pierce [46]. This can be done by assuming the exit of the pipe is a circular piston of radius a on which each infinitesimal

area acts as the infinitesimal source of a spherical wave. The pressure and velocity solutions of the free space spherical wave equation are.

$$\begin{aligned} p(r,t) &= \frac{A}{r} e^{i(\omega t - kr)} \\ v(r,t) &= \frac{Ak}{\rho\omega r}\left(1 - \frac{i}{kr}\right) e^{i(\omega t - kr)}, \end{aligned} \tag{2.56}$$

where r is the distance from the source, k is the wave number, ω is the angular frequency, and A is a constant that depends on the strength of the source. An expression for A can be determined by assuming the source is a sphere of radius ϵ vibrating with normal velocity $v(\epsilon)$. The volume flow generated at the surface of the sphere is $q = 4\pi\epsilon^2 v(\epsilon) e^{i\omega t}$. Combining this with Eq. 2.56 it is found $A = \frac{q\rho\omega}{4\pi}\frac{e^{ik\epsilon}}{k\epsilon - i}$. For $k\epsilon \ll 1$ this simplifies to $A \approx \frac{iq\rho\omega}{4\pi}$. Thus, the infinitesimal pressure generated by a small area dS on another area dS' is

$$dp_{dS'} = \frac{i\rho\omega}{4\pi}\frac{e^{i(\omega t - k|\mathbf{r}-\mathbf{r}'|)}}{|\mathbf{r}-\mathbf{r}'|} dq = \frac{iU_0\rho\omega}{4\pi}\frac{e^{i(\omega t - k|\mathbf{r}-\mathbf{r}'|)}}{|\mathbf{r}-\mathbf{r}'|} dS, \tag{2.57}$$

where $|\mathbf{r}-\mathbf{r}'|$ is the distance between dS and dS'. The second equality comes from the fact that the acoustic strength of the small piece of area is given by $dq = U_0 dS$, where U_0 is the velocity flowing through that area. The total pressure on dS' can be found by integrating Eq. 2.57 over the s coordinate.

$$p_{dS'} = \frac{iU_0\rho\omega}{4\pi}\int \frac{e^{i(\omega t - k|\mathbf{r}-\mathbf{r}'|)}}{|\mathbf{r}-\mathbf{r}'|} dS. \tag{2.58}$$

The infinitesimal force generated on the piston by the pressure on dS' is $df = p_{dS'}dS'$. Thus, the total force on the piston can be found by multiplying Eq. 2.58 by dS' and integrating over the s' coordinate.

$$f = \frac{iU_0\rho\omega}{4\pi}\int\int\frac{e^{i(\omega t-k|\mathbf{r}-\mathbf{r}'|)}}{|\mathbf{r}-\mathbf{r}'|}dSdS'. \tag{2.59}$$

Evaluating this integral,

$$f = \rho c\pi a^2 U_0 e^{i\omega t}\left(1-\frac{J_1(2ka)}{ka}+i\frac{H_1(2ka)}{ka}\right), \tag{2.60}$$

where J_1 is the Bessel function of the first kind of order 1 and H_1 is the Struve function of order 1. Recalling from the the previous section the specific acoustic impedance of the piston for a sinusoidal driving force of frequency ω is defined as

$$Z = \frac{p}{U_0 e^{i\omega t}} = \frac{f/\pi a^2}{U_0 e^{i\omega t}}. \tag{2.61}$$

Substituting in the expression for f,

$$Z(\omega) = \rho c\left(1-\frac{J_1(2ka)}{ka}+i\frac{H_1(2ka)}{ka}\right). \tag{2.62}$$

Thus, the end of the pipe can be thought of as an acoustic load with resistance $R = \rho c\left(1-\frac{J_1(2ka)}{ka}\right)$ and reactance $X = \rho c\frac{H_1(2ka)}{ka}$ [47]. Fig. 2.1 shows a plot of the real and imaginary parts of the impedance. Now that an expression for the exit impedance has been found, the spatial boundary value problem

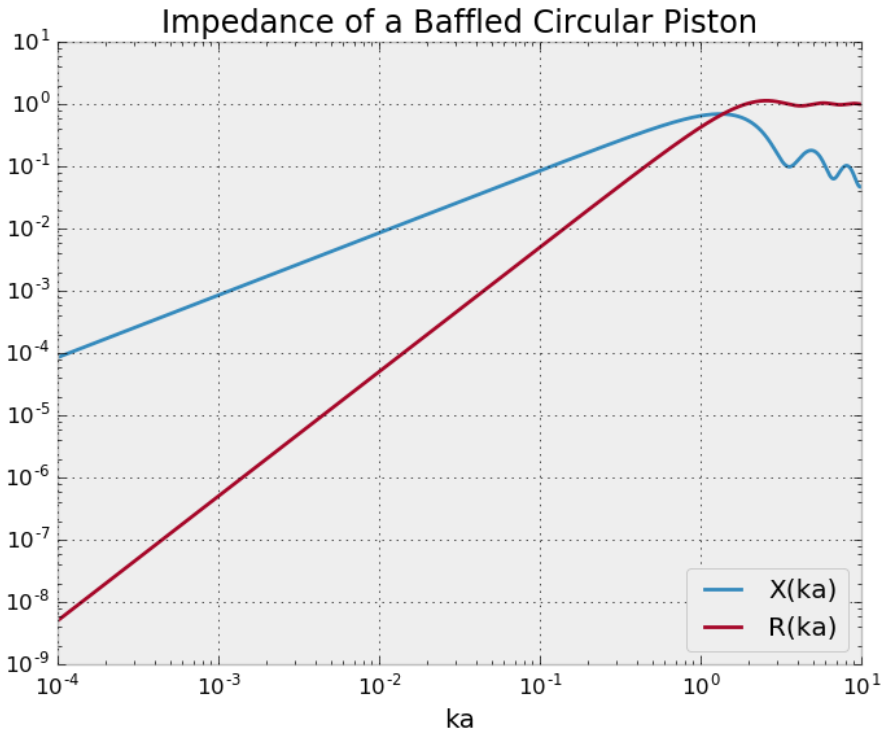

Figure 2.1: A log-log plot of the reactive and resistive parts of the mouth impedance in units such that $\rho c = 1$. At very low frequencies it can be seen that the impedance becomes primarily reactive and approaches a conservative system. At very high frequencies it becomes primarily resistive. In this regimes, its main effect will be to dissipate energy

is well determined, and the spatial eigenmodes the spatial eigenmodes can be calculated.

2.6.4 An Example

Now that an expression for the mouth impedance has been found,the boundary value problem determined by Eqs. 2.52 and 2.55 can be solved. However

first it should be acknowledged that the real parts of s and Z make this boundary value problem non hermitian. The non hermitian nature of this boundary value problem reflects the presence of radiation from the mouth. This results in complex eigenvalues and non-orthogonal eigenfunctions. For a physically realistic treatment of the rat vocal tract radiation from the mouth cannot be ignored. The difficulties of including this mechanism will be dealt with in a later chapter. In this section, as a simpler example, the boundary value problem in the low frequency approximation will be considered. This reduces to a hermitian problem and is an important historical result in acoustics. The low frequency approximation of $Z(\omega)$ can be derived by assuming the quantity $ka \ll 1$. In this limit Eq. 2.62 can be expanded in powers of ka and retain only linear terms. The impedance becomes

$$Z(\omega) \approx i\rho c \frac{2ka}{3\pi}. \tag{2.63}$$

Here the resistive part of the impedance has become negligible, and the reactive part only provides a linear contribution. Substituting this into Eq. 2.55, the boundary conditions becomes

$$s_m \hat{\phi}_m(L, s_m) + c\frac{2ka}{3\pi}\frac{\partial}{\partial x}\hat{\phi}_m(L, s_m) = 0. \tag{2.64}$$

Now solving Eq. 2.52 and applying the boundary condition at $x = 0$ the eigenfunctions of the problem (up to a constant factor) are

$$\hat{\phi}_m(x) = \sinh\left(\frac{s_m x}{c}\right) \tag{2.65}$$

Plugging the eigenfunctions into Eq. 2.64 the characteristic equation, which determines the eigenvalues, is obtained.

$$\tanh\left(\frac{s_m L}{c}\right) = -i\frac{2k_m a}{3\pi}. \tag{2.66}$$

The real part of this equation is

$$\sinh\left(\frac{2\alpha_m L}{c}\right) = 0. \tag{2.67}$$

This equation is only satisfied for $\alpha_m = 0$, which indicates energy is not dissipated from the pipe due to radiation and that the problem is hermitian. With $\alpha_m = 0$ Eq. 2.66 becomes

$$\tan\left(k_m L\right) + \frac{2k_m a}{3\pi} = 0. \tag{2.68}$$

This equation can be numerically solved for the eigenfrequencies. However, it is also instructive to expand the tan function out in a power series about

its roots $m\pi$. Retaining only the linear term of the power series,

$$k_m \left(L + \frac{2a}{3\pi} \right) = m\pi. \tag{2.69}$$

This is the same characteristic equation that is obtained from using the boundary condition $\hat{\phi}_m(L + \Delta L) = 0$ with $\Delta L = \frac{2a}{3\pi}$. The quantity ΔL is known as the end correction. So the additional reactance at the end of the pipe makes the resonance modes behave in the same way as that obtained by a zero stress boundary condition for a pipe of length $L + \Delta L$. The interpretation of this is that in addition to the oscillations of the air inside the resonator there is a small amount of air that lies directly beyond that mouth that also oscillates. The inertia of this air must be taken into account when computing the resonance frequencies of the system. Fig. 2.2 shows a plot of the characteristic equation and eigenfrequencies obtained using the end correction approximation. Fig. 2.3 shows a plot of the resonance modes given by Eq. 2.65. This is often the stopping point of classical acoustics. However, an important question of this work is how does an acoustic system switch between the different resonance modes. It is my belief that the frequency jumps of rat ultrasonic vocalizations are the result of these kinds of transitions. The frequency domain analysis of this section is insufficient to answer to this question. In a later chapter the problem will be formulated in the time domain

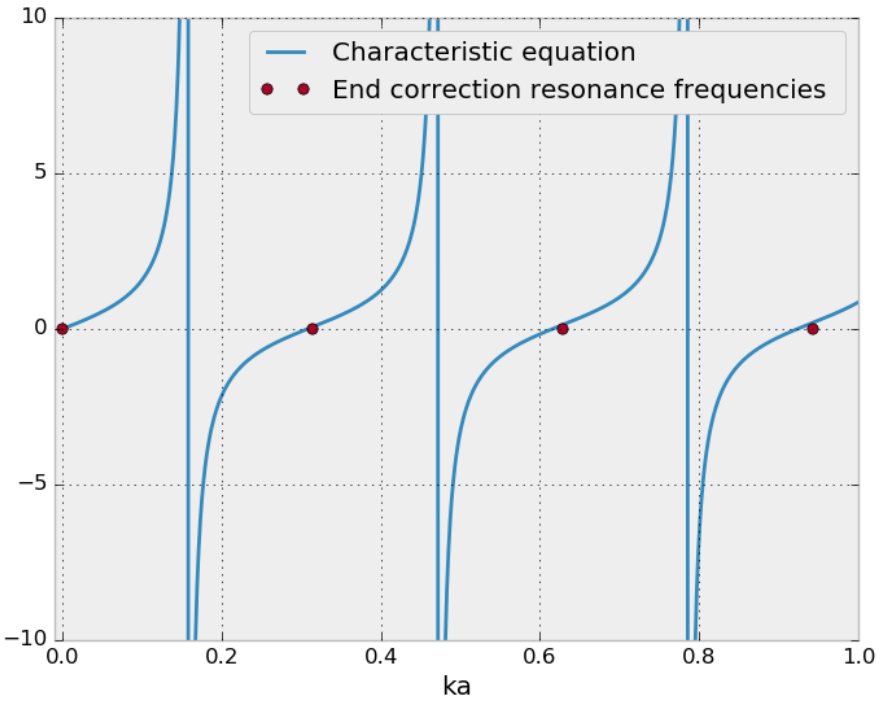

Figure 2.2: A plot of the left hand side of Eq. 2.68for $L = 10$ m and $a = 1$ m. The roots of this function give the eigenfrequencies and can be approximated in the low frequency limit by Eq. 2.69, which is to equivalent to finding the eigenfrequencies of the system using the boundary condition $\hat{\phi}_m(L+\Delta L) = 0$. It can be seen that the end correction approximation starts to deviate from the true roots of the systems as ka gets bigger.

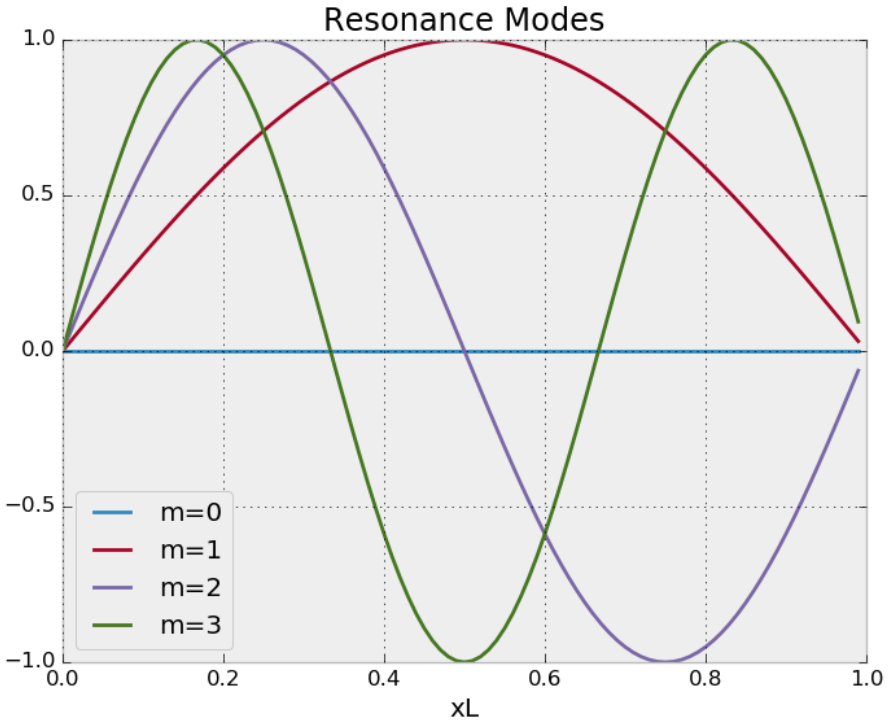

Figure 2.3: A plot of the first four resonance modes (Eq. 2.65) for $L = 10$ m and $a = 1$ m. It can be seen that eigenmodes almost perfectly fit into the spatial extent of the problem. This is a result of the inertia due to the end correction.

2.7 Inviscid, Incompressible, Potential Flow

2.7.1 Bernoulli's Equation

For this type of flow one simplifying assumption from acoustic flow will be relaxed and another simplifying assumption will be introduced. The flow will no longer be assumed to be linear, which was important in deriving the acoustic wave equation. However the inviscid and irrotational assumptions will be kept. These assumptions will allow the derivation of a conservation equation known as Bernoulli's equation. In addition it will be assumed the flow is incompressible, meaning variations in density can be neglected. This will simplify the continuity equation. In a later chapter this type of flow will be used to model the movement of air through the rat vocal folds throughout a vocalization. The relaxation of the linear assumption is important as it will allow turbulent losses due to viscosity to be taken into account, even though the motion of an inviscid fluid is being analyzed. The incompressible assumption will simplify the continuity equation, which will allow the flow to be analyzed without resorting to direct numerical simulations. In a previous section the equation of motion for an inviscid fluid was derived (Eq. 2.38).

$$\rho \frac{D\mathbf{v}}{Dt} = -\nabla p. \tag{2.70}$$

Writing out the convective derivative this becomes

$$\rho\left(\frac{\partial \mathbf{v}}{\partial t} + (\mathbf{v}\cdot\nabla)\mathbf{v}\right) = -\nabla p. \tag{2.71}$$

Now using the vector identity $(\mathbf{v}\cdot\nabla)\mathbf{v} = \frac{1}{2}\nabla(\mathbf{v}\cdot\mathbf{v})$ to write the Euler equation as

$$\rho\left(\frac{\partial \mathbf{v}}{\partial t} + \frac{1}{2}\nabla(\mathbf{v}\cdot\mathbf{v})\right) = -\nabla p. \tag{2.72}$$

Furthermore using the fact that the fluid is irrotational to write the velocity field as the gradient of a potential function $\mathbf{v} = \nabla\phi$. Substituting this into the above equation and factoring out the ∇ operator,

$$\nabla\left(\frac{\partial \phi}{\partial t} + \frac{1}{2}\mathbf{v}\cdot\mathbf{v} + \frac{p}{\rho}\right) = 0. \tag{2.73}$$

In this step the fact that the fluid is incompressible has been used, since it was assumed ρ is constant when the ∇ operator was factored out. Now this expression can be integrated between any two points in the fluid. The curve connecting these two points is irrelevant, since the fluid is irrotational. It is only the end points that matter.

$$\int_1^2 d\mathbf{s}\cdot\nabla\left(\frac{\partial \phi}{\partial t} + \frac{1}{2}\mathbf{v}\cdot\mathbf{v} + \frac{p}{\rho}\right) = 0. \tag{2.74}$$

Using the fundamental theorem of calculus Bernoulli's equation for an unsteady, inviscid, potential flow is obtained.

$$\frac{\partial \phi_1}{\partial t} + \frac{v_1^2}{2} + \frac{p_1}{\rho} = \frac{\partial \phi_2}{\partial t} + \frac{v_2^2}{2} + \frac{p_2}{\rho}, \tag{2.75}$$

where it has been defined $v^2 = \mathbf{v} \cdot \mathbf{v}$. The interpretation of this equation is that quantity on either side is the same throughout all points in the fluid [41].

2.7.2 The Continuity Equation

Bernoulli's equation describes conservation of energy between any two points in an inviscid irrotational fluid. In practice a conservation of mass equation is also needed to fully determine the flow variables. Eventually the rat vocal tract will be modeled as a series of cylindrical pipes. For this physical configuration the incompressible continuity equation takes an especially simple form. If variations in density are neglected in Eq. 2.6, the incompressible continuity equation is obtained

$$\nabla \cdot \mathbf{v} = 0. \tag{2.76}$$

Suppose there are two points 1 and 2, separated by an axial distance in a cylindrical pipe of varying area. The area of the pipe at point 1 is A_1, and the area of the pipe at point 2 is A_2. Integrating Eq. 2.76 over the volume

V of the pipe bounded by areas A_1 and A_2

$$\int_V dV\,(\nabla \cdot \mathbf{v}) = 0. \tag{2.77}$$

Now the divergence theorem can be used to write this integral as a surface integral over the surface area A of V.

$$\int_A d\mathbf{A} \cdot \mathbf{v} = 0. \tag{2.78}$$

Because of the zero penetration condition (i.e. there can not be any fluid flowing into the walls of the pipe) the quantity $d\mathbf{A} \cdot \mathbf{v} = 0$ on the walls of the pipe. So the above integral reduces to the sum of surface integrals over A_1 and A_2.

$$\int_{A_1} d\mathbf{A} \cdot \mathbf{v}_1 + \int_{A_2} d\mathbf{A} \cdot \mathbf{v}_2 = 0. \tag{2.79}$$

This equation states that the volume flow of fluid through surface A_1 must be balanced out by the flow of fluid through surface A_2. If it is assumed the fluid flows through the pipe in one direction (say from 1 to 2). Further it can also be assumed that flow velocity only varies axially, not radially or azimuthally, then the quantity $d\mathbf{A} \cdot \mathbf{v}$ is constant on A_1 and A_2. Thus,

$$A_1 \mathbf{v}_1 \cdot \mathbf{n}_1 + A_2 \mathbf{v}_2 \cdot \mathbf{n}_2 = 0, \tag{2.80}$$

where $\mathbf{n}_1$ and $\mathbf{n}_2$ are the outward normal vectors for surfaces A_1 an A_2. If further it is assumed the flow is axial, this simplifies even further.

$$A_1 v_1 = A_2 v_2. \tag{2.81}$$

This continuity equation for axial incompressible pipe flow. It will be used later the analysis of the flow through the rat vocal folds [41].

2.8 Nonlinear Energy Losses at an Orifice

In this section Bernoulli's equation will be used to analyze the energy losses of a fluid as it flows through a circular aperture of area A_f and length L. This is similar to the analysis done by Hirschberg and Rienstra [48] as well as the one done by Cummings [49]. In a later chapter the results from this section will be used to model the flow of air through the rat vocal folds. First the the flow will be analyzed using a linear approximation, and the shortcomings of this approximation will be discussed. Consider two points directly before and after the start of the aperture. These points will be called 1 and 2. The pressure at those points is p_1 and p_2 respectively. Now as first approximation, consider the air in the circular aperture as an incompressible cylindrical slug, which is accelerated by the pressure difference $\Delta p = p_2 - p_1$. From Newton's second law, the time rate of change of the velocity of the slug is

$$\rho_0 L A_f \dot{u}_f = p_1 A_f - p_2 A_f = -\Delta p A_f, \tag{2.82}$$

where $\rho_0 L A_f$ is the mass of the air in the aperture and u_f is its velocity (the subscript f is being used for these quantities because later this analysis will be used to model the flow through the vocal folds). If the slug of air is forced with a sinusoidal pressure difference of the form

$$\Delta p = |p| \cos \omega t, \tag{2.83}$$

the velocity of the slug of air can be calculated with Eq. 2.82.

$$u_f = -\frac{|p|}{\rho_0 L \omega} \sin \omega t. \tag{2.84}$$

Thus, the amplitude of the velocity oscillations is $\frac{|p|}{\rho_0 L \omega}$. This is exactly the relationship Ingard and Ising measured for low velocity flows through a circular orifice. They found as long as the velocities were below a threshold value value the, the relationship between pressure and velocity amplitudes was linear. However, they found something somewhat surprising. For velocities greater than that threshold value the relationship became quadratic [50]. The above analysis does not predict this relationship because in calculating the relationship between pressure and velocity amplitudes the formation of the air into a jet as it enters the orifice was neglected. This jet has kinetic energy per unit volume $\frac{\rho}{2} u_f^2$ associated with it, which is lost due to turbulent dissipation when the jet expands outward on the other side of the orifice.

Bernoulli's equation can be used to calculate this nonlinear energy loss. Writing down Bernoulli's Equation between points 1 and 2, where it is as-

sumed the air flowing through the aperture has already formed into a jet with velocity u_f at point 1. Furthermore, it is also assumed at point 2 the kinetic energy has been completely dissipated due to turbulence.

$$\Delta p - \frac{\rho_0}{2} u_f^2 + \rho_0 \frac{\partial}{\partial t} (\phi_2 - \phi_1) = 0. \tag{2.85}$$

The velocity potential difference is related to the velocity of the air in the aperture $u(x)$ through the equation $\phi_2 - \phi_1 = \int_1^2 u(x)dx$. As long as the radius of the aperture is constant the velocity of the air in the aperture can be approximated as constant, and the potential difference can be written as $\phi_2 - \phi_1 = u_f L$. The energy balance equation becomes

$$\Delta p - \frac{\rho_0}{2} u_f^2 + \rho_0 L \dot{u}_f = 0. \tag{2.86}$$

This equation gives the quadratic relationship, observed by Ingard and Ising, between the pressure drop across the orifice and the velocity of flow through the orifice. Furthermore, it reduces to Eq. 2.82 for low values of u_f. This result is actually quite interesting. Even though inviscid and irrotational flow through the aperture was assumed, an expression for the nonlinear energy losses due to viscous turbulent dissipation has been obtained. The relevance of this result will become more apparent in a later chapter when the pressure on the far side of the aperture is used to model the driving of resonance modes in the upper vocal tract of the rat. The nonlinear energy losses will serve to keep the time domain simulations bounded.

Chapter 3

Data Analysis of Rodent Ultrasonic Vocalizations

3.1 Introduction

This chapter discusses the procedures used to collect and analyze recordings of rat ultrasonic vocalizations (USVs). This analysis was done to infer information about the mechanism by which rat USVs are produced. First, this chapter will review aerodynamic whistles and the hole tone model proposed by Roberts [37]. Then descriptions of the data collection and analysis procedures will given. Finally, it will be concluded that the hole tone mechanism is not consistent with the results obtained from the analysis. This is likely because it does not take into account the resonance frequencies of the upper vocal tract. The data and a description of the analysis is also available at

https://gitlab.com/mdornfe1/vocalization_analysis. This chapter contains a summary of the analysis and its results. The Gitlab repository contains a description of how to use the code written for this analysis.

3.2 Aerodynamic Whistles

The mechanisms by which aerodynamic whistles operate can be somewhat varied. However, they all share two features in common. An aerodynamic whistle must have have an active amplifying mechanism by which it converts the energy of a laminar flow into acoustic oscillations. This mechanism is usually the natural instability of a jet of air or the instability caused by interaction of the jet with a sharp edge. If a stream of air is focused into a jet, even if it is initially laminar, small disturbances in the flow will grow in size exponentially until they reach a nonlinear saturation point. At low Reynold's numbers these disturbances resemble small fluctuations in the jet velocity. At higher Reynold's numbers they begin to resemble vortex ring (Fig. 3.4) or vortex line (Fig. 3.2) like structures. In either case, these disturbances are a result of the conversion of laminar flow energy into oscillatory flow energy. This growth mechanism is still not fully understood and is a current topic of research.

In some whistles, this is the primary mechanism by which sound is produced. These fluctuations radiate acoustic energy off into the far field, which can be recorded by laboratory equipment. However in other whistles, such

as most woodwind instruments, this active mechanism drives a passive resonance response, which is determined by the physical dimensions of the instrument. This passive resonance response is then the primary mechanism by which sound is radiated.

The second feature common to all acoustic whistles is a feedback mechanism by which part of the amplified oscillatory energy is returned to the source of the disturbances. This results in a frequency selection procedure, in which the most unstable disturbance frequency feedbacks the most energy to the source, which causes it to grow even further. By the time the system reaches steady state, most of the oscillatory energy is in this preferred frequency, which is the frequency observed by a listener. In some systems the vortex growth process is the feedback mechanism. Vorticity grows in the laminar stream of air as it is convected downstream. As the vortex structure reach its nonlinear saturation point, the velocity it induces in the surrounding fluid feeds back energy to the source of the disturbance, causing the next vortex structure to grow. Chanaud calls these type I whistles. Examples of this type of whistle include the flow of air pass a power line or an Aeolian harp. These whistles are not very relevant to the problem of ultrasonic vocalization generation, so they will not be discussed further. In other systems, the developed vorticity interacts with downstream structures, which results in induced flow velocity. This induced flow velocity is what is responsible for feeding back energy to the vorticity source. Chanaud calls these type II whistles. A few examples of this type of whistle will be discussed in this sec-

tion. Lastly, are systems in which the vorticity growth mechanism is coupled to a passive resonance cavity. In these systems the acoustic field generated by the resonance cavity is responsible for the feedback. These are type III whistles and correspond most closely to what are though of as woodwind instruments [16]. The hole tone mechanism proposed by Roberts to describe rodent USVs is a type II whistle. It is the purpose of this chapter to show this mechanism is inadequate to explain rodent USVs. This is possibly because the mechanism fails to take into account the resonance frequencies of the upper vocal tract. In the next chapter a type III whistle will be discussed that incorporates elements of the hole tone and the resonance frequencies of the upper vocal tract.

3.2.1 Cavity Tones

A shallow cavity tone consists of a laminar stream of air passing over a cavity of streamwise length L and depth d. When the stream of air passes over the upstream sharp edge of the cavity vortex lines are shed from the sharp edge. In the potential flow framework, this is the result of the Kutta condition, which requires that the fluid velocity remain finite as it pases around the sharp edge. The vortex lines travel toward the downstream edge of the cavity at velocity U_c. The interaction of the vortex line with this edge induces a flow, which feeds energy back to the upstream edge, which influences the shedding of further vortex lines. Thus, the vortex shedding frequency is determined by the travel time of a vortex line $\frac{L}{U_c}$ [51].

By studying vortex shedding in a cavity tone, Rossiter proposed a semi empirical formula to predict the observed acoustic frequencies f of the system. For low Mach numbers this formula is

$$\frac{fL}{U_c} = n - \gamma. \tag{3.1}$$

Here γ is an empirical constant, which lie in the interval $[-1, 1]$. It takes into account the travel time for a vortex line through the system [52]. Although this equation was originally empirically derived for cavity oscillations it also applies to acoustic whistles in general. In all systems U_c is the velocity at which the amplifying mechanism is convected, and γ takes into account the phase delays associated with the feedback mechanism. For example a deep cavity tone not only depends on the travel time of the vortex line but also on the acoustic field excited in the cavity. This will result in a different value of γ. The value of γ for the shallow and deep cavities are shown in Fig. 3.14 [51].

3.2.2 The Edge Tone

The edge tone is perhaps the best studied class II whistle (Fig. 3.1). It consists of a planar jet of air which emerges from a semi infinite rectangular slit. The planar jet of air impinges on a downstream edge. The jet is inherently unstable, and any small disturbance will cause the jet to oscillate above and below the edge. At higher Reynold's number the jet oscillations

reach an amplitude great enough to form discrete vortex lines, resulting in a Von Kármán vortex street 3.2. The flow oscillations from the jet or Von Kármán vortex street impart a force on the edge. The reaction force from the edge on the surrounding fluid results in an acoustic flow with a dipole like source. This acoustic flow provides the feedback mechanism to the source of instabilities in the jet. For the edge tone γ will be the result of the phase delay caused by the convection travel time of vorticity along the jet and the time it takes for sound to travel back towards the source. For the edge tone this quantity is also shown in Fig. [16].

3.2.3 The Hole Tone

The hole tone is in some sense an axisymmetric version of the edge tone (Fig. 3.3). It however is somewhat less understood than its planar counterpart. This is mainly because the planar symmetry of the edge tone makes analysis easier than the axial symmetry of the hole tone. This whistle consists of an axisymmetric jet emerging from a circular orifice. Like the planar jet of the edge tone, any velocity disturbance in axisymmetric jet of the hole tone will grow in size, causing an increase in vorticity of the jet. At high enough Reynold's numbers these velocity disturbances grow into discrete axisymmetric vortex structures called vortex rings. The vortex rings convect along the length of the system and impact upon a downstream aperture. This causes a periodic forcing of the air inside the downstream aperture, which creates an acoustic field similar to that of a monopole sound source. This acoustic

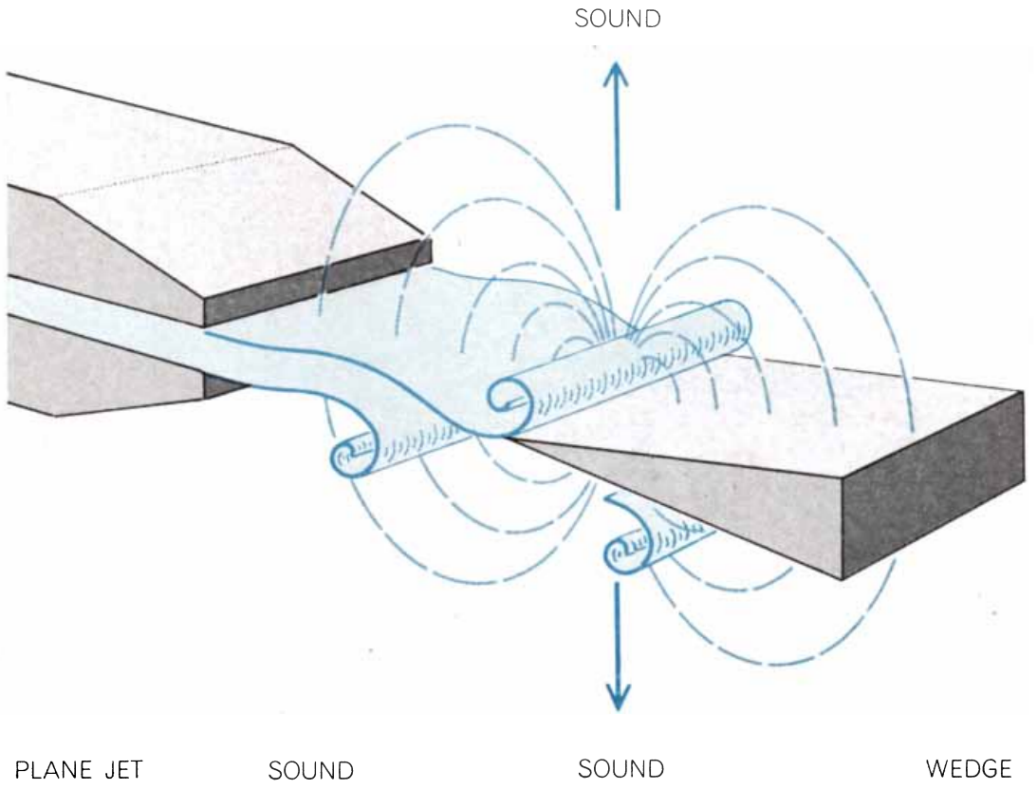

Figure 3.1: Illustration of the edge tone. A planar jet emerges from a rectangular slit. The jet impinges on a downstream edge. The natural instabilities of the jet will grow. Interactions between these instabilities and the downstream edge results in a dipole acoustic field, which feeds back energy to the jet source, and also radiates acoustic energy to observers **??**.

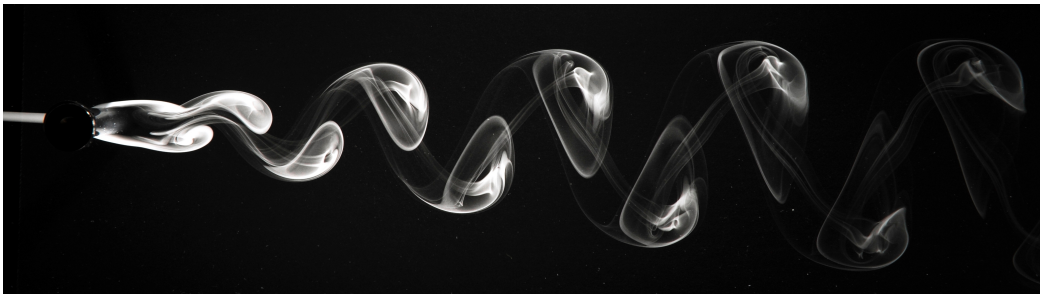

Figure 3.2: Photograph of a Von Kármán vortex street, which is generated by laminar flow passing over a circular cylinder. At higher Reynold's numbers jets with rectangular symmetry will destabilize and form these discrete vortex structures. Photograph by Jrgen Wagner, distributed under a CC BY-SA 4.0 license.

field feeds back energy to the first aperture, where the disturbances initially begin to grow. This feedback mechanism reinforces the strongest frequency disturbances, resulting in a selection procedure in which disturbances of a single frequency become much stronger than the rest. The hole tone will sound at this frequency [16]. Like the edge tone, the value of γ for the hole depends upon the convection time of the vortex structures and the time it takes for sound to travel from the downstream aperture to the upstream one. This value has been measured experimentally [51] and is shown in Fig. .

Roberts proposed the hole tone as a possible mechanism behind rat USVs. He believed the vocal folds may form the upstream aperture. However, he was uncertain which anatomical structure may form the downstream aperture. In support of this proposal Roberts constructed an artificial hole tone, consisting of two metallic plates, and was able to reproduce sounds qualitatively similar to rat USVs, using physiologically realistic blowing pressures [37]. While this

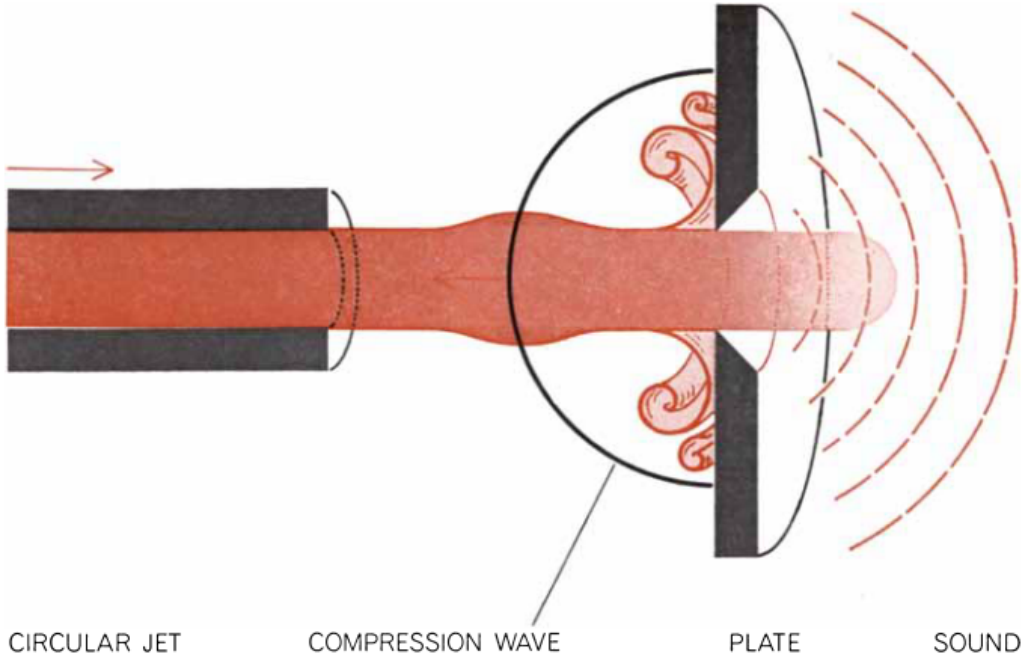

Figure 3.3: Illustration of the hole tone. An axisymmetric jet emerges from a circular hole. Disturbances in the velocity of the axisymmetric jet grow and result in a fluctuating flow through a downstream aperture. This fluctuating flow generates a monopole acoustic field, which provides feedback to the jet source and radiates sound to observers [16].

proposal is promising it is far from conclusive. Many aerodynamic whistles can reproduce sounds qualitatively similar to rat USVs. Furthermore, the hole tone does not take into the resonance frequencies of the rat upper vocal tract, and as already mentioned there is no known anatomical structure which functions as the downstream aperture. It is the purpose of the analysis of this chapter to show that the hole tone is inconsistent with recordings of rat USVs.

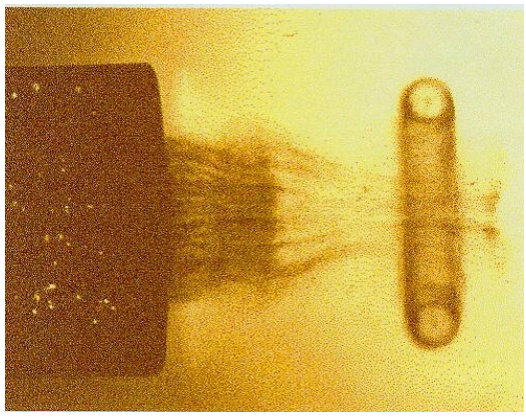

Figure 3.4: Photograph of a vortex ring. Axisymmetric jets naturally destabilize into a series of these structures at higher Reynold's numbers. This photograph is in the public domain and was taken by George Kenneth Lucey Jr, Dr. D. Lyon, and Frank Dindl.

3.2.4 Frequency Jumps

Many aerodynamic whistle systems exhibit a phenomenon known as a frequency jump, like those seen in Fig. . In a frequency jump, the system will be sounding at one frequency. A parameter of the system (such as length or driving velocity) is then varied continuously. The continuous variation of this parameter may continuously modulate the sounding frequency. However, it is also possible that variation of this parameter brings the system through a point of dynamical significance in which the stability of the underlying frequency disturbances is altered. The disturbances associated with the current sounding frequency may die out, and disturbances of another frequency can become unstable. This will result in a discontinuous jump of the sounding frequency. Chanaud and Powell have observed frequency jumps in hole tone

whistles [43]. Holger has discussed frequency jumps in edge tones [53], and Coltman has observed frequency jumps in organ pipes [54]. These jump happen so quickly that the bulk parameters of the system, such as length and convection velocity, can be thought of as constant before and after the jump. Thus, from Eq. 3.1 it can be inferred that it must be the mode number n which changes during a jump. In practice n usually goes up or down one integer value. Dividing the after jump instance of Eq. 3.1 by its before jump instance,

$$m(c,\gamma) = \frac{f_2}{f_1} = \frac{n \pm 1 - \gamma}{n - \gamma}, \tag{3.2}$$

where f_2 is the after jump frequency, f_1 is the before jump frequency, and n is the before jump mode number. This ratio is defined to be $m(c,\gamma)$, the slope of the mode line for cluster c and given value of γ.

3.3 Data Collection

Data collection consisted of recording USVs from rat pairs placed in a cage. In a given recording session, each rat was placed in their own section of the cage. The rats were allowed to sense and interact with each other but were separated by a thin mesh. Some sessions consisted of two male rats, and some sessions consisted of a male and female rat. All together nine males and two females were used. Each recording sessions lasted one hour. Audio was recorded using a condenser ultrasound Avisoft-Bioacoustics CM16/CMPA-5V microphone connected to a National Instruments data acquisition card at

a sampling rate of either 250 kHZ or 300 kHz. The recording sessions were then divided into 9598 individual call snippets, based on long quiescence times between the snippets. The analysis was done on these call snippets. (cite Diego here)

3.4 Analysis and Discussion

These recordings were analyzed through their reassigned spectrograms with the intention of elucidating the production mechanism of rat USVs. Fig. 3.5 shows an example of a reassigned spectrogram for a 50 ms segment of a rat USV. It can be seen that rat USVs largely consist of a single monotonal modulated sound. The time points such as the ones around $t = 23$ ms and $t = 43$ ms, where the frequency discontinuously jumps from 55 kHz to 35 kHz and back again, are particularly salient features. They were the focus of this analysis. To help identify the rat USV production mechanism a one dimensional curve is fit to the reassigned spectrograms of thousands of USVs recorded from nine different rats. From this curve the frequency jump points are extracted by identifying points where the curve rapidly increased or decreased. These frequency jump points are then fit to Eq. 3.2 using a clustering algorithm. In doing so a value of γ is determined for each rat. These values of γ are then used to help identify the production mechanism.

To fit a one dimensional curve to the reassigned spectrograms the mean frequency, weighted by the energy in each frequency bin, is calculated for

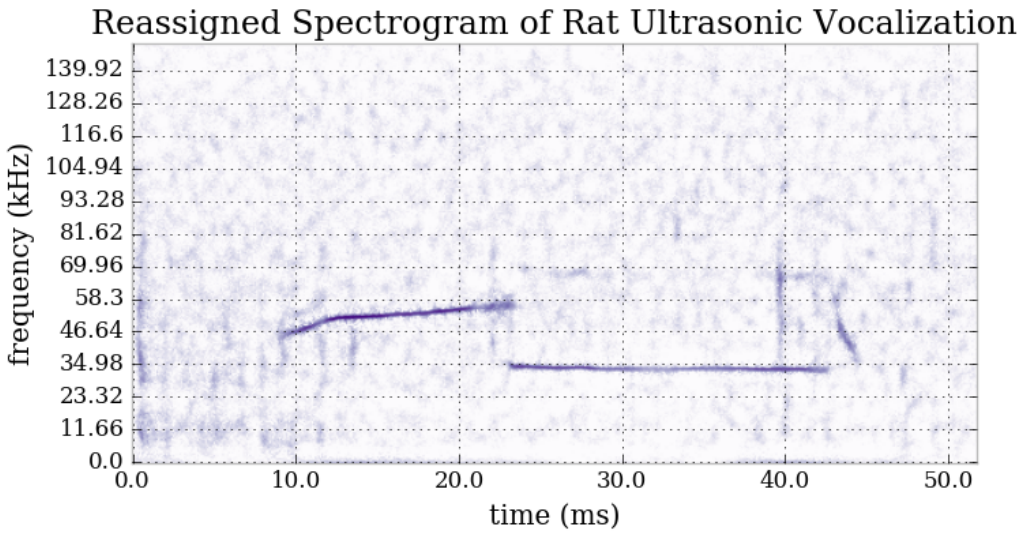

Figure 3.5: Reassigned spectrogram of rat USV. Frequency jumps can be seen at approximately 23.0 ms and 43.0 ms after the start of the recording.

each time time slice in spectrogram space. Fig. 3.6 illustrates the curve fitting algorithm at a few selected time points for the spectrogram in Fig. 3.5. At each time point the power distribution is treated as a probability distribution. The maximum of that distribution is found, then average of the three surrounding frequencies is computed weighted by the power in each frequency. This mean is then computed for every time point in the spectrogram. Fig. 3.8 shows the result of this algorithm by plotting the fitted curve on top of the spectrogram.

It can be seen that the fit to the recorded vocalization is rather good albeit imperfect. However it is only important that the fit corresponds well at the frequency jump points, which can be seen to be true. A feature extraction algorithm, which looks for points where the curve changes very

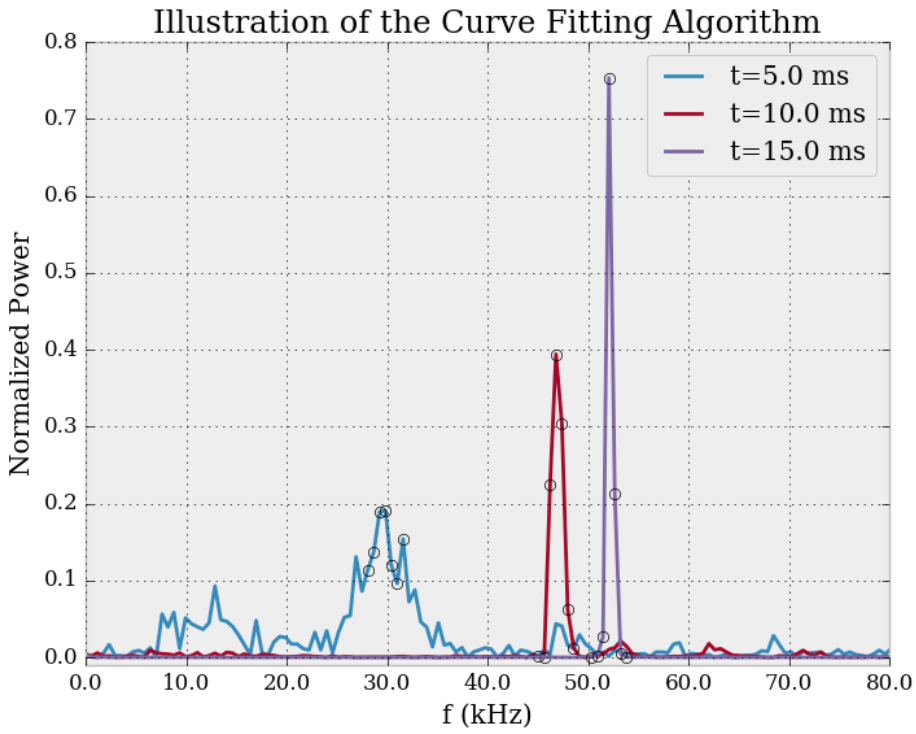

Figure 3.6: Power plotted against frequency for the time points 5.0 ms, 10.0 ms, 15.0 ms of the spectrogram shown in Fig. 3.5. The time point 5.0 ms shows the power distribution of noise. Although this particular time point has low entropy it will be ignored by the jump extraction algorithm because it is in a high entropy region.

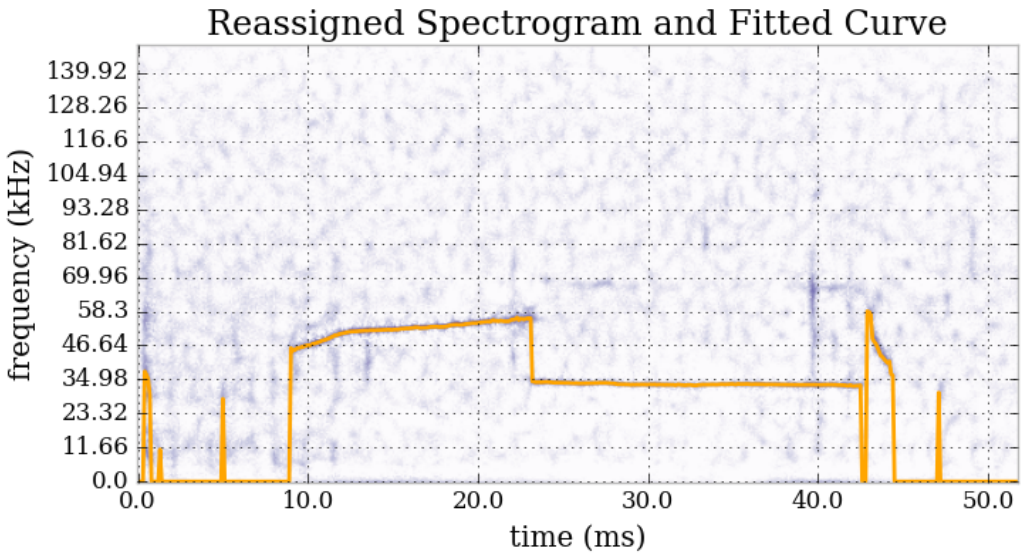

Figure 3.7: Spectrogram with fitted curve obtained by the fitting algorithm described in the text.

rapidly, is then used to calculate the frequency jump points from the curve. Fig. 3.8 shows the results of the extraction algorithm by plotting the jump points on top of the fitted curve and spectrogram. It can be seen that the jump extraction algorithm is quite accurate. It gives very few false positives. The algorithm rejects the jump point at $t = 43.0$ ms because the fitted curve varies to much in that region, but that does not pose a problem to the analysis since it is not a systemic error.

The values of thousands of frequency jumps can be calculated by applying the curve fitting and feature extraction algorithm to the spectrograms of all of the USV recordings in the dataset. Fig. 3.9 shows the results of this analysis for all of the recordings take from one of the rats in the experiment With a visual examination of Fig. 3.9 it can be seen that the jump points

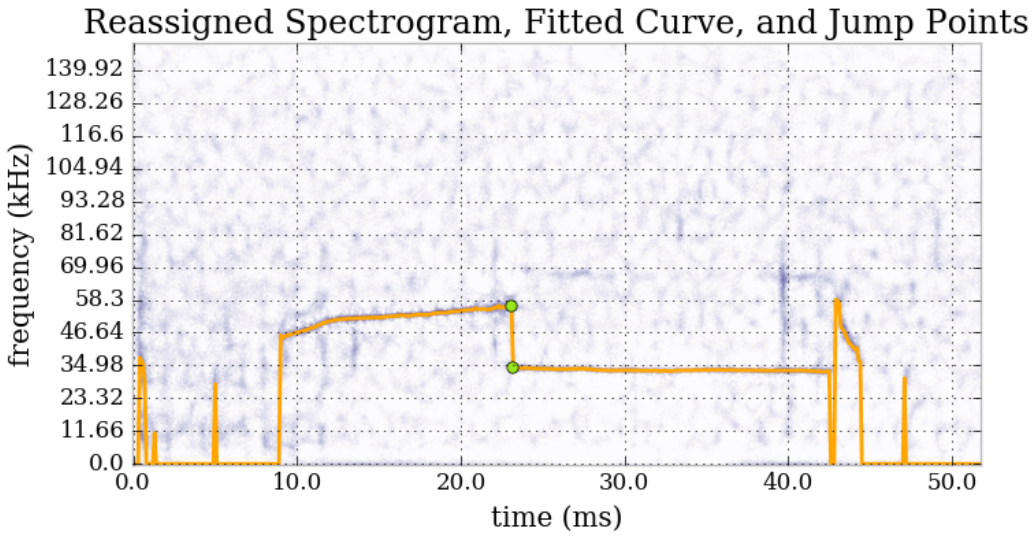

Figure 3.8: Spectrogram, fitted curve, and extracted jump points. The algorithm rejects the jump point at $t = 43.0$ ms because the fitted curve varies to much in that region, but that does not pose a problem to our analysis since it is not a systemic error.

are separated into two large groups. The upper group consists of upward frequency jumps, while the lower group consists of downward frequency jumps. Within these two large groups, it can be seen there are three subgroupings. Each subgrouping seems to consist of points clustered along a straight line. This is exactly what would be expected from Eq. 3.2, the interpretation begin that each subgroup corresponds to a mode transition $n \to n \pm 1$. From this perspective the slopes of each line that the points group themselves into is given by the right side of Eq. 3.2. By clustering these points according to this equation an estimation can be obtained for the parameter γ.

Fig. 3.10 shows the mode lines, for several values of n, with slopes given by Eq. 3.2 for a randomly chosen value of γ. The goal is to group the jump

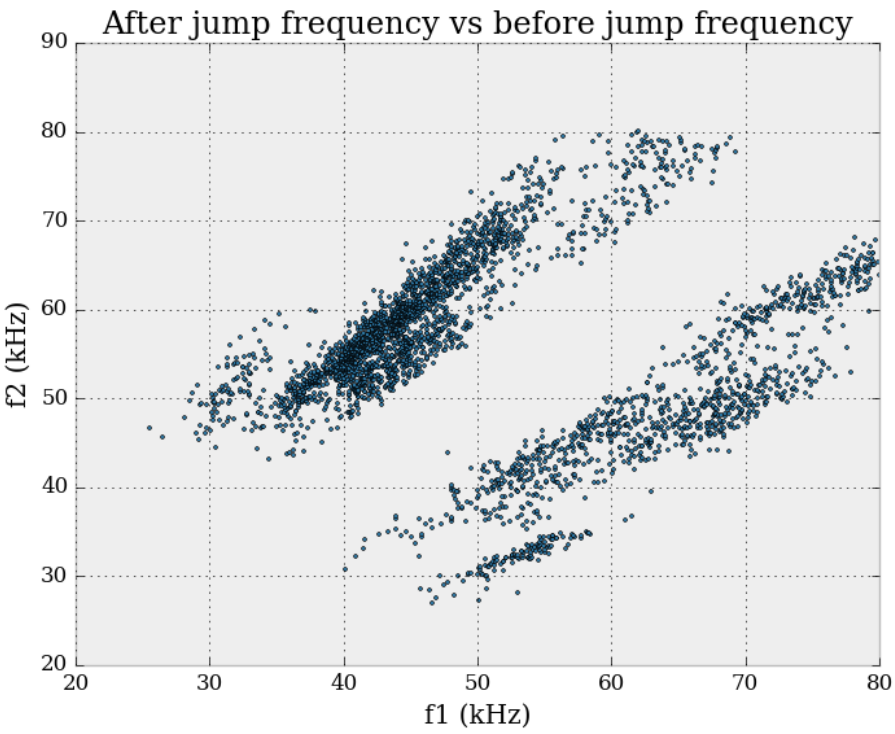

Figure 3.9: The results of the curve fitting and feature extraction algorithm are shown in this figure by plotting the after jump frequency against the before jump frequency for each data point.

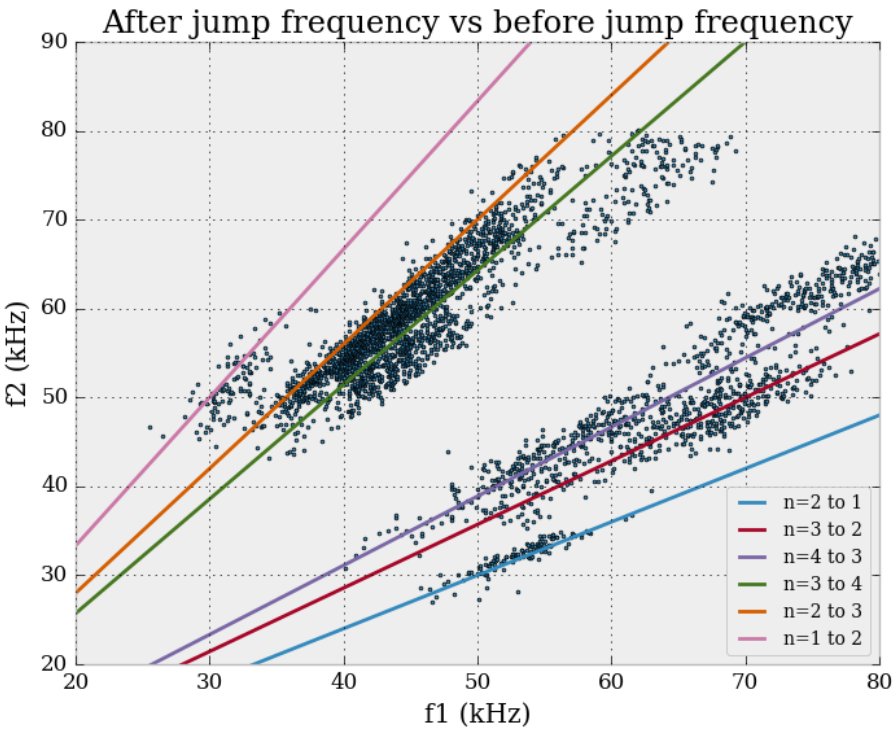

Figure 3.10: Extracted jump frequencies for rat V6. Mode lines from Eq. 3.2 are plotted over the jump frequencies. The goal is to assign each jump point to the closest mode line.

points into appropriate mode transition clusters. This is done by assigning a point to the line for which the perpendicular distance between the two objects is minimal. This is most easily done using the point in polygon algorithm. To do this the bisectors of the above lines are found and polygons are drawn so that their vertices lie on the bisecting lines. Fig. 3.11 shows the polygons that are constructed from the mode lines in this way. Points are then assigned to the polygon in which they lie.

By examining Figs. 3.10 and 3.11 it can be seen that the clustering

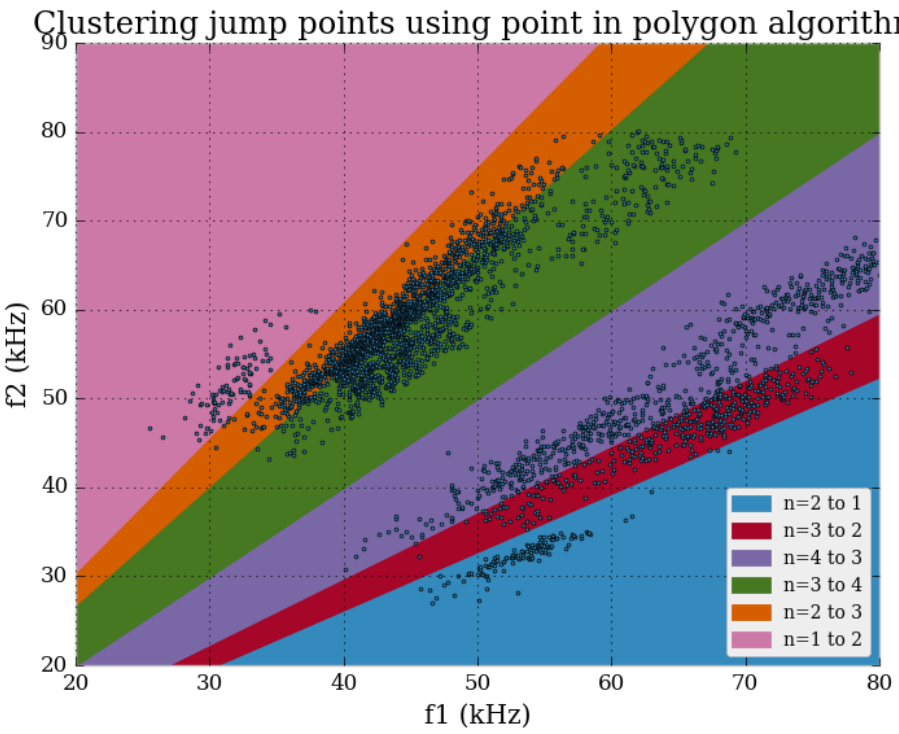

Figure 3.11: Illustration of how the point in polygon algorithm is used to cluster the jump points. Each polygon corresponds to a mode line from Eq. 3.2. The mode lines run down the center of their associated polygons. Jump points are assigned to the polygon in which they lie.

obtained for this value of γ roughly corresponds to the natural breaks in density of the points plotted in this space. However, a better clustering result can be obtained by finding an optimal value of γ. To do this a cost function is defined as the sum of the squares of the perpendicular distances of each point to its assigned cluster line divided by the number of points in each cluster.

$$C(\gamma) = \sum_{c} \frac{1}{N_c} \sum_{i_c=1}^{N_c} (\Delta x_{i_c})^2 + (\Delta y_{i_c})^2 \tag{3.3}$$

$$\Delta x_{i_c} = \left| f_{1,i_c} - \frac{f_{1,i_c} + m(c,\gamma)\, f_{2,i_c}}{m(c,\gamma)^2 + 1} \right| \tag{3.4}$$

$$\Delta y_{i_c} = \left| f_{2,i_c} - \frac{m(c,\gamma)\,(f_{1,i_c} + m(c,\gamma)\, f_{2,i_c})}{m(c,\gamma)^2 + 1} \right| \tag{3.5}$$

In this expression Δx_{i_c} and Δy_{i_c} are the respective horizontal and vertical distances of the i^{th} point in cluster c to its assigned line, and N_c is the number of points in cluster c. Each cluster c corresponds to one type of mode transition $n \to n \pm 1$. The quantities f_{2,i_c} and f_{1,i_c} are the after and before jump frequencies of the i^{th} point in cluster c. The quantity $m(c,\gamma)$ is the slope of the mode line for cluster c and given value of γ as defined in Eq. 3.2. Fig. 3.12 shows the function calculated from the points in Fig. 3.9. The minimum of this function is given by the value of γ that best fits the data. Fig. 3.13 shows the jump points clustered using this optimal value of γ.

The value of this result is two-fold. First, it gives an estimation for the parameter γ. This gives an indication of the mechanism which is being used

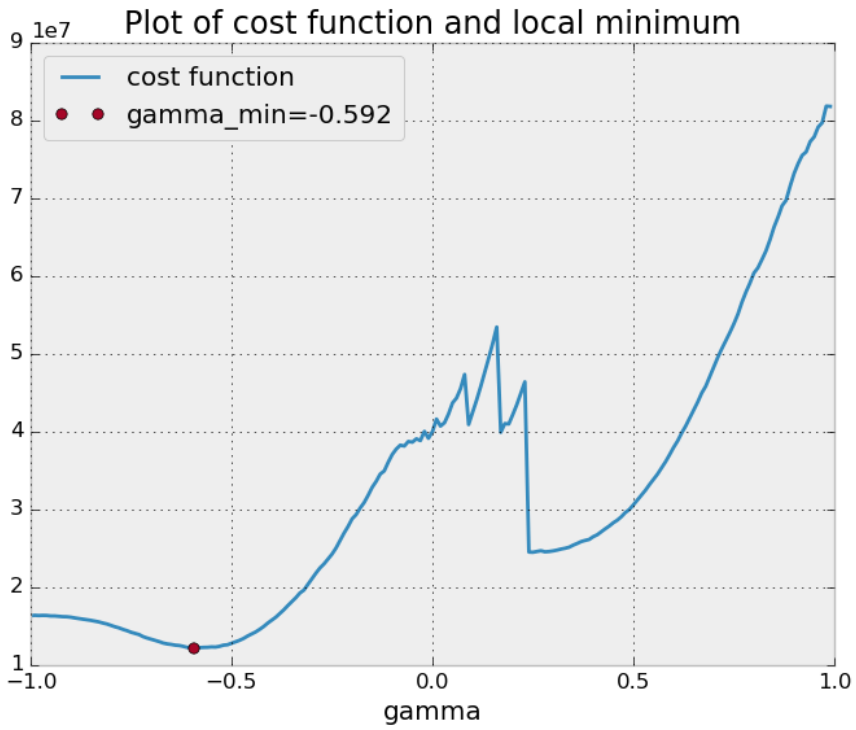

Figure 3.12: Plot of the cost function (for the frequency jump points in Fig. 3.9) defined in Eq. 3.3. The red circle marks the minimum of the function.

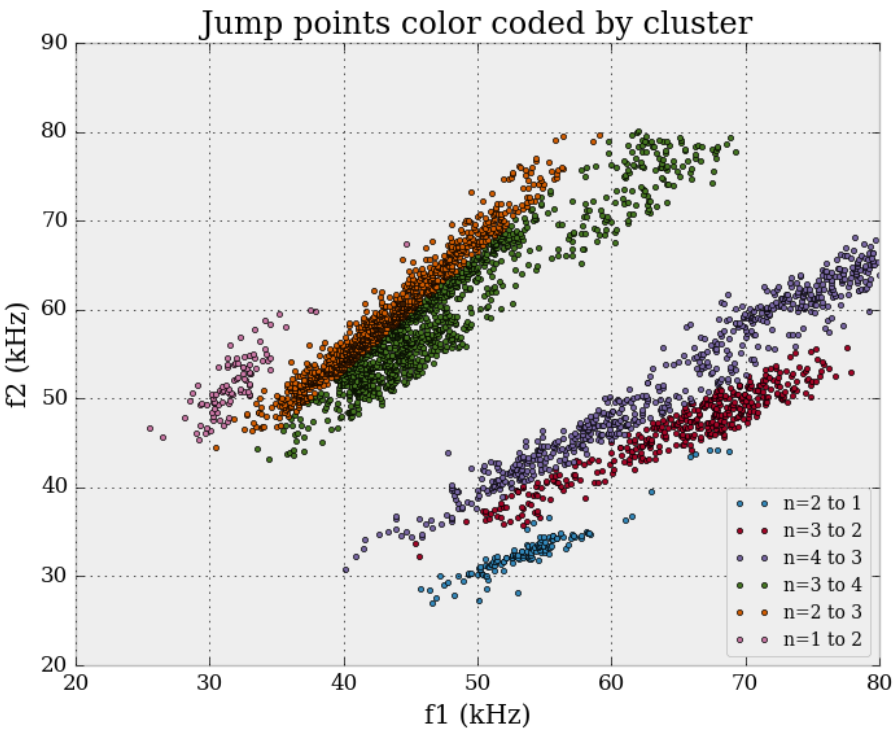

Figure 3.13: Jump points, for the rat V6, clustered using the optimal value of γ. The color coding of the points indicates their assigned cluster.

to produce the vocalization. This and how to obtain confidence intervals for these estimates is discussed more in a later section. Second, it gives a method for classifying ultrasonic vocalizations. Further exploration of the data shows that if vocalizations, with jump points in the same mode transition cluster, are compared it can be seen they are qualitatively similar. This is believed to be indicative of the fact that rats used different resonance modes to communicate different types of information. Although the actual informational content of rat ultrasonic vocalizations is largely unknown there is research to support this. As discussed in a previous chapter, it has been shown that vocalizations in the 22 kHz range are used as a warning call to other rats when a predator is detected [27, 28, 29, 30]. It is also been shown that calls in the 50-85 khZ range are associated with positive mental states and are used in playful and sexual situations [30]. The program point_browser, in the GitLab repository, can be used to interactively view the entire vocalization from which a jump point is extracted.

By computing confidence intervals on the estimation of γ for different rats information can be inferred about the mechanism by which the recorded vocalizations are produced. The bootstrapping method can be used to calculate these confidence intervals. Bootstrapping works by taking measurements from an experiment and randomly sampling those measurements with replacement to get a resampled set of measurements. The number of resampled measurements is equal to the original number of measurements, but some of them may be duplicates since sampling was done with replacement.

Measurements in this case are the extracted frequency jumps. The optimal value of γ can then be computed for the resampled measurements. This process can be done a large number of times (approximately 1000) to build a probability distribution for γ. This distribution can be used to calculate confidence intervals for on the calculated value of γ. Fig. 3.14 shows the results of this analysis for the nine rats in this experiment.

In the plot in Fig. 3.14 it can be seen that the values of γ for the different rats seem to group around -0.6. Some rats give a slightly different value for γ. This is probably because these rats did not exhibit vocalizations in mode regimes seen in other rats. The rat V1 for example only seemed to vocalize in the n=3 and n=4 modes. This may have affected the estimation of γ for this rat. Nevertheless the value of γ for the hole tone is well outside the confidence intervals for γ of the different rats. Thus, it is very unlikely that this is the source of their vocalizations. Also shown in this plot are known values of γ for different acoustic mechanisms. Based on this plot, the edge tone is a candidate for the true mechanism. However, the anatomy of the rat vocal tract makes this an unlikely source. The half open pipe is anatomically consistent with the rat vocal tract, but it still lies outside most of the calculated confidence intervals. Further theoretical work needs to be done on modeling the acoustics of the rat vocal tract. It is my view that the true mechanism is a combination of the hole tone and the half open pipe, where vorticity growth of an axisymmetric jet drives the resonance modes of a half open pipe.

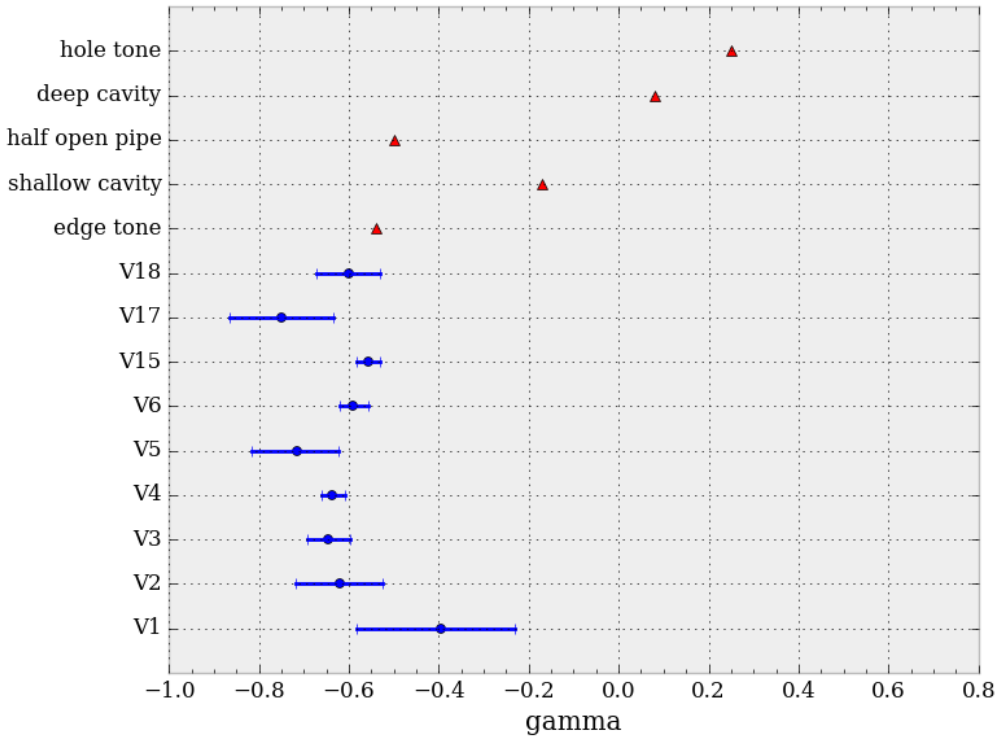

Figure 3.14: Estimates of γ for different rats along with 95 % confidence intervals computed using the bootstrapping method (blue). Also shown are known values of γ for different aerodynamic whistles. It can be seen that the value of γ for the hole tone falls well outside all computed confidence intervals. Therefore, it is very unlikely that this mechanism responsible for rodent USVs.

Chapter 4

Time Domain Model of the Rodent Vocal Tract

4.1 Introduction

Much of the study of sound has concerned itself with frequency domain analyses of acoustical systems. This is understandable since acoustics is very much a practical discipline that is used by engineers to construct better structures. When building a bridge the main acoustical concern is that the structure's resonance frequencies are not excited by the environment. Simply calculating the resonance frequencies in Fourier or Laplace space usually provides sufficient knowledge to prevent this. The transient behavior of how the structure might get to this resonance mode is a more challenging problem and of less interest to structural engineerss. Conversely, when constructing musical

instruments the builder wants to ensure that the resonance frequencies of the instruments are excited. Frequency domain calculations often provide enough knowledge to accomplish this task. Consideration of time domain transient behavior actually is important in the construction of musical instruments. However, consideration of this aspect is often much more of an art than a quantitative science. When quantiative time domain knowledge is needed by engineers they often resort to direct numerical simulations of the Navier-Stokes or wave equations. My goal is to understand the qualitative dynamics of rodent ultrasonic vocalizations (USVs). As discussed in chapter 3 frequency jumps are a notable feature of rodent USVs and are transient and dynamical in nature. Understanding this phenomenon is best accomplished by analyzing low dimensional time domain systems. Thus, the more common frequency domain approaches will be insufficient for me.

In chapter 3 I showed that the previously proposed hole tone model is insufficient to account for the rodent USV mechanism. I also discussed how the half open pipe is more consistent with the results from that chapter. In section 2.6 I discussed a frequency domain analysis of the half open pipe and how that analysis is insufficient to account for how the system may transition between different resonance modes. In this chapter I will derive a low dimensional time domain model for the half open pipe and discuss how it applies to the rodent upper vocal tract, but first I will discuss some low dimensional nonlinear time domain models for organ pipes, since they have been a great source of inspiration for this work.

4.2 Time Domain Models of Organ Pipes

An organ pipe consists of a resonant pipe driven by a planar jet. The planar jet emerges from a rectangular slit and interacts with a downstream edge, much like the edge tone discussed in chapter 3. However unlike the edge tone, the vortex shedding is not directly responsible for the production of sound heard by an observer. The shed vortices drive the resonance modes of the pipe, which then radiates acoustic energy to an observer. The resonance modes also control the jet feedback process, which is responsible for selecting the vortex shedding frequency. Fig. 4.1 shows an illustration of an organ pipe. Fletcher was one of the early researchers to develop a nonlinear time domain model of organ pipe acoustics [55]. He assumed that the normal modes of the pipe obeyed a set of damped oscillator equations coupled together by a nonlinear forcing $F(t)$.

$$\ddot{x}_i + k_i \dot{x}_i + n_i^2 x_i = \lambda_i F(t), \tag{4.1}$$

where x_i is the displacement of an acoustic particle in the i^{th} resonance mode at the mouth of the pipe. The quantity k_i is the damping of that mode. The quantity n_i is the natural frequency of that mode, and λ_i is a scaling constant for the forcing. The quantity $v = \sigma_i \dot{x}_i$ is the total flow velocity through the mouth of the pipe.

Fletcher assumed the forcing could be expanded as series on to the mouth

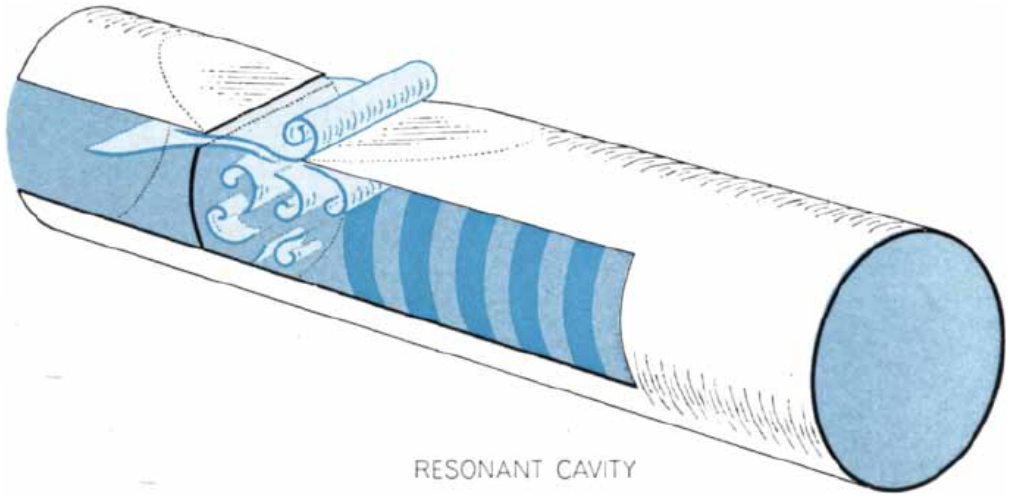

Figure 4.1: Illustration of an organ pipe. A planar jet emerges from a slit, which then interacts with a downstream edge. The interaction between the jet and the edge causes the jet to destabilize and roll up into vortex line structures. The vortex lines drive the resonant cavity, which radiates acoustic energy to observers, and controls the feedback process, which determines the vortex shedding frequency [16]. Awaiting permission.

velocity v.

$$F(t) = c_0 + c_1 v + c_2 v^2 + c_3 v^3 + ... \tag{4.2}$$

Here the constants c_i are functions of the blowing pressure p. In this expansion, Fletcher retained terms up to and including the cubic term. In doing so he was able to take into account two very important nonlinear mechanisms. The cubic term accounts for the unsteady flow caused by the driving jet oscillating above and below the entrance to the resonant pipe. The quadratic term accounts for dissipation of potential flow into vorticity as discussed in section 2.8. Fletcher also recognized that the acoustic velocity acts on the jet as it leaves the source slit, but this will only affect the resonance pipe some time later after this disturbance has traveled through the mouth. Thus, the forcing should include a time delay δ_i that is frequency dependent to account for dispersive effects

$$F(t) = \sum_{m=0}^{\infty} \sum_{i=1}^{\infty} \dot{x}_i \left(t - \delta_i\right)^m . \tag{4.3}$$

Using this relatively simple formulation Fletcher was able to account for many qualitative properties of organ flue pipe transients. The major drawback of this model is its phenomenological and ad hoc nature. In theory, it should not be necessary to assume the resonance modes can be described by a set of oscillators. This should be derivable from first principles. In addition, $F(t)$ should also be derivable from first principles, not from a power series expansions.

A more modern model initiated by Auvray et al. takes steps in this direction [56]. They assumed the acoustic admittance (the reciprocal of acoustic impedance) of the resonance pipe could be written as a summation of modal terms.

$$Y = \sum_{n=0}^{\infty} \frac{Y_n}{\omega_n^2 - \omega^2 + j\varepsilon_n \omega_n \omega}, \tag{4.4}$$

where Y_n, ε_n, and ω_n are the amplitude, damping coefficient, and pulsation of the n^{th} mode. Assuming $\omega \approx \omega_n$ and taking the inverse Fourier transform of this expression they obtained a set of time domain equations for the modal acoustic velocities driven by the pressure at the entrance of the resonator pipe Δp.

$$\ddot{v}_n + \varepsilon_n \omega_n \dot{v}_n + \omega_n^2 v_n = Y_n \frac{\partial \Delta p}{\partial t}, \tag{4.5}$$

where the acoustic velocity at the mouth is given by $v_{ac}(t) = \sum_n v_n(t)$.

They separated the driving pressure into two important mechanisms $\Delta p = \Delta p_{src} + \Delta p_{los}$. The quantity Δp_{src} is the unsteady driving pressure from the jet oscillating above and below the mouth. Fig. 4.2 show the planar jet impingining on the downstream edge. For this pressure source, they derived the semi-empirical expression

$$\Delta p_{src} = \frac{\rho \delta_d b U_B}{W} \tanh\left(\frac{h e^{\alpha_i W}}{U_B b} v_{ac}(t-\tau) - \frac{y_{off}}{b}\right). \tag{4.6}$$

The other pressure source accounts for nonlinear losses from the potential flow dissipating into vorticity. For this pressure source they use an expression

quadratic in acoustic velocity.

$$\Delta p_{los} = -\frac{\rho}{2}\left(\frac{{v_{ac}}^2}{\alpha_{vc}}\right) sgn\left(v_{ac}\right) \tag{4.7}$$

An expression like this can be derived from Bernoulli's equation as discussed in section 2.8. In these expressions, ρ is the density of air. The quantity δ_d is the effective acoustic distance between the two monopole sources on either side of the labium. h is the height of the flue exit (source of the jet). U_B is the centerline velocity of the jet. b is the half width of the jet. W is the distance between the jet source and the resonator pipe (it is also known as the window length). H_W is the window width. τ is the time it takes for a jet disturbance to travel along the window, y_{off} is the offset of the jet from the center of the flue, and α_{vc} is the vena contracta factor that accounts for the jet

Using these equations they were able to reproduce qualitative and quantitative features of real recorders. Most notable they were able to reproduce the bifurcation diagram of a recorder transitioning between the $n = 1$ and $n = 2$ modes, which is similar to my goal for the rat vocal system. Although this model is quite successful, it still has the drawback of being semi-empirical and ad hoc. Assuming the system obeys an equation of the form Eq. 4.4 is not equivalent to deriving a set of oscillator equations from the equations of motion. Furthermore, Eq. 4.5 is only valid when the frequency is near the resonance modes of the system. Caclulating the driving force on a resonance

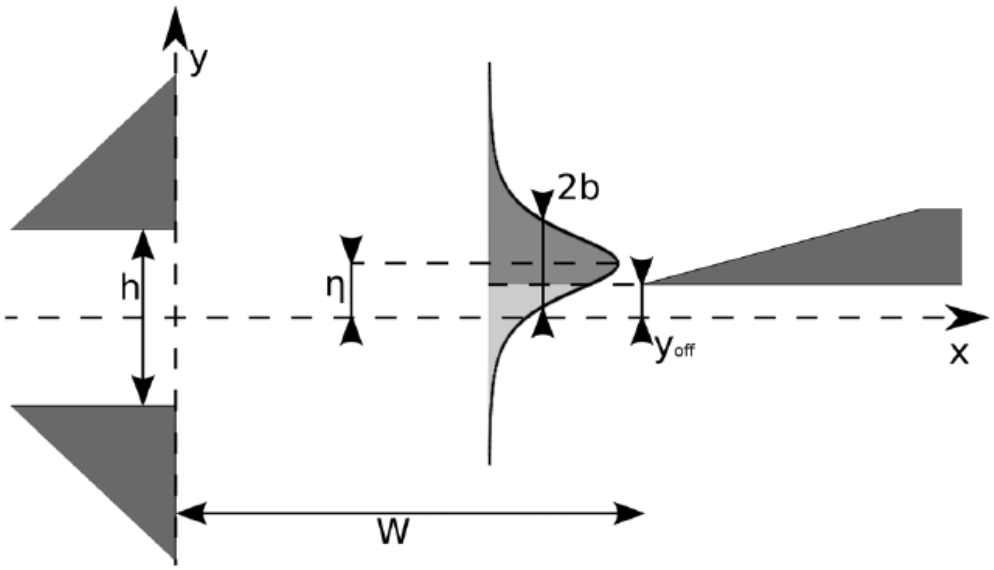

Figure 4.2: The interaction of the planar jet with the downstream edge in a recorder or an organ pipe. The quantity h is the height of slit from which the jet emerges. W is the distance between the slit and the entrance to the resonance pipe. y_{off} is the distance between the center of the slit and the height of the edge. b is the jet half-width. $\eta(t)$ is the time-dependent height of the center of the jet [17]. Reprinted with permission.

cavity due to jet oscillations is difficult. It is further complicated by the fact the resonance cavity provides feedback disturbances to the jet, which will grow as they convect along the jet and further drive the resonance cavity. An expression of the form of Eq. 4.6, although also semi empirical, is desirable. However, the analysis of this system is simplified by the presence of the window area, which allows the jet disturbances to grow before they interact with the resonance pipe. This allowed the authors to neglect nonlinearities in the jet equations. Their analysis was also simplified by the planar symmetry of the jet. My system is driven by an axisymmetric jet, which is somewhat more complicated. This is a current topic of research for me and will require a different approach that takes into account nonlinear saturation effects. In the rest of the chapter I will derive a set of time domain equations for the resonance modes of a one dimensional cylindrical resonator. I will also talk about where the driving force from the axisymmetric jet will be included in the model and how it is necessary to get stable oscillations of the resonance modes.

4.3 Derivation of the Model

Here I will derive a time domain set of equations that describe the evolution of the set of acoustic modes for a cylindrical pipe, which will be used to model the acoustics of the rodent upper vocal tract (Fig. 4.3). The flow in the pipe will be assumed to be described by the velocity potential wave equation.

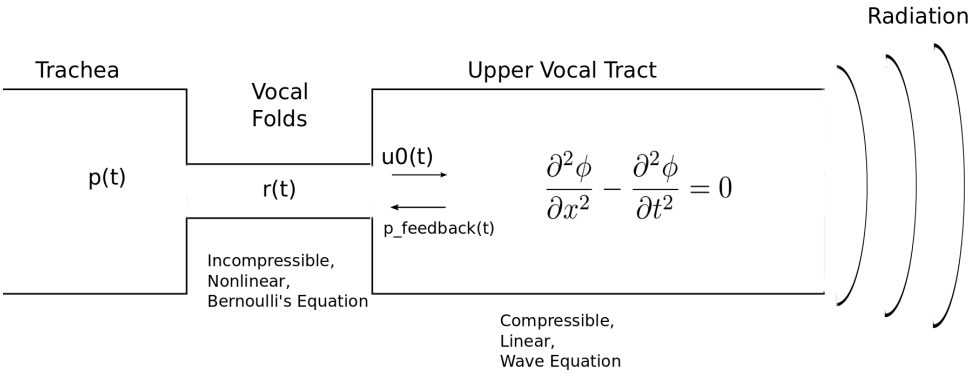

Figure 4.3: A schematic model of the rodent vocal tract. Subglottal pressure $p(t)$ drives flow through the vocal folds, which have radius $r(t)$. The flow $u_0(t)$, emerging from the vocal folds, along with any additional pressure sources, drives the acoustic flow in the upper vocal tract, which is described by the velocity potential $\phi(x,t)$. The acoustic flow provides feedback pressure $p_{feedback}(t) = p(0,t) = -\frac{\partial\phi(0,t)}{\partial t}$, which opposes $u_0(t)$.

The acoustic modes of the upper vocal tract are driven by flow emerging from the vocal folds. The flow through the vocal folds is driven by the subglottal pressure $p(t)$ in the trachea. This flow is the source of both linear and nonlinear driving forces as well as coupling between the different acoustic modes. The right exit of the pipe is assumed to have Robin type dissipative boundary conditions. These boundary conditions take into account the end correction and the acoustic radiation that linearly dissipates energy from the system. This derivation will be done in variables in which position, velocity, and pressure are non-dimensionalized by

$$x^* = \frac{x}{L}, \quad u^* = \frac{u}{c}, \quad p^* = \frac{p}{\rho c^2} \tag{4.8}$$

Here L is the length of the rat vocal tract, which has been measured to be approximately 4 mm. The quantities ρ and c are the density of air and speed of sound at STP. In the following paragraphs the stars will be dropped on the non dimensional variables.

I will first derive a time domain representation for the behavior of the upper vocal tract. To do this I will begin with the initial-boundary value problem for the velocity potential of the acoustic waves in the linear resonator. The first boundary condition indicates that the pipe is being driven with velocity u_0. The second boundary condition comes from the definition of specific impedance $p = Zu$. From the definition of velocity potential and the linear Euler equation $p = -\frac{\partial\phi(x,t)}{\partial t}$ and $u = \frac{\partial\phi(x,t)}{\partial x}$. Combining these two definitions results in the second boundary condition. Here Z is the impedance in the time domain. However, soon I will solve the spatial part of the problem in Laplace space. This way I can use the frequency domain impedance I discussed in subsection 2.6.3. The initial condition comes from assuming the system starts from rest.

$$\begin{aligned} \frac{\partial^2\phi}{\partial x^2} - \frac{\partial^2\phi}{\partial t^2} &= 0 \\ \frac{\partial\phi(0,t)}{\partial x} &= u_0(t, \phi(0,t), \dot{\phi}(0,t)) \\ \frac{\partial\phi(1,t)}{\partial t} + Z\frac{\partial\phi(1,t)}{\partial x} &= 0 \\ \frac{\partial}{\partial x}\phi(x,0) &= 0 \end{aligned} \tag{4.9}$$

The quantity $u_0(t, \phi(0,t), \dot{\phi}(0,t))$ is the driving velocity entering the upper

vocal tract from the vocal folds. It depends on the velocity potential in the vocal tract at $x = 0$ due to feedback. However from now on I will suppress these arguments and indicate its time derivative with $\dot{u_0}$. The inhomogeneous boundary condition at $x = 0$ can be removed with the substitution $\phi(x,t) = \psi(x,t) - u_0\frac{(x-1)^2}{2}$, where ψ is a function that satisfies the homogeneous boundary conditions but has an inhomogeneous driving term in the wave equation.

$$\begin{aligned} \frac{\partial^2\psi}{\partial x^2} - \frac{\partial^2\psi}{\partial t^2} &= u_0 - \ddot{u}_0\frac{(x-1)^2}{2} \\ \frac{\partial\psi(0,t)}{\partial x} &= 0 \\ \frac{\partial\psi(1,t)}{\partial t} + Z\frac{\partial\psi(1,t)}{\partial x} &= 0 \\ \frac{\partial}{\partial x}\psi(x,0) &= 0 \end{aligned} \tag{4.10}$$

Next expanding $\psi(x,t)$ onto a set of spatial eigenmodes $\phi_l(x)$. $\psi(x,t) = \sum_{m=0}^{\infty} q_m(t)\phi_m(x)$. The projections $q_m(t)$ vary with time and are called the modal participation factors. The eigenmodes $\phi_m(x)$ must satisfy the boundary conditions in Eq. 4.10, and for the case of nonzero radiation they will be complex and not orthogonal. In the next section I will derive their precise form. Substituting the modal projection of $\psi(x,t)$ into Eq. 4.10,

$$\sum_{m=0}^{\infty} q_m\phi_m''(x) - \ddot{q}_m\phi_m(x) = u_0 - \ddot{u}_0\frac{(x-1)^2}{2}. \tag{4.11}$$

Eq. 4.11 is a matrix equation, which can be solved for the modal participation

factors. To do so I will need a suitable set of spatial eigenmodes so the left hand side of the equation can be diagonalized

4.4 The Spatial Eigenmodes

A set of spatial eigenmodes can be found by solving the initial-boundary value problem

$$\begin{aligned} \frac{\partial^2 \psi_H}{\partial x^2} - \frac{\partial^2 \psi_H}{\partial t^2} &= 0 \\ \frac{\partial \psi_H(0,t)}{\partial x} &= 0 \\ \frac{\partial \psi_H(1,t)}{\partial t} + Z\frac{\partial \psi_H(1,t)}{\partial x} &= 0. \end{aligned} \tag{4.12}$$

Eq. 4.12 is the homogeneous version of Eqs. 4.9 and 4.10. I assume a solution of the form $\psi(x,t) = \phi_m(x)e^{s_m t}$, where $s_m = i\omega_m - \alpha_m$. The minus sign in front of α_m indicates the energy of the solutions is expected to decrease with time due the resistive part of Z. Substituting this assumption into Eq. 4.12 I get the boundary value problem

$$\begin{aligned} \phi_m''(x) - s_m^2\phi_m(x) &= 0 \\ \phi_m'(0) &= 0 \\ s_m\phi_m(1) + \hat{Z}(\omega)\phi_m'(1) &= 0 \end{aligned} \tag{4.13}$$

Now that the problem has been transformed to the frequency domain the exit impedance for a baffled cylindrical piston, discussed in subsection 2.6.3,

can be used. This will account for the effects of radiation and inertia at the end of the pipe.

$$\hat{Z}(\omega) = \left(1 - \frac{J_1(2\omega a)}{\omega a} + i\frac{H_1(2\omega a)}{\omega a}\right). \tag{4.14}$$

The impedance takes this form because in this non dimensionalization $k^* = \frac{2\pi L}{\lambda} = \frac{L}{c}\omega = \omega^*$.

After applying the boundary condition at $x = 0$, the solution to this system (up to a constant scaling factor) is

$$\phi_m(x) = \cosh(s_m x). \tag{4.15}$$

Substituting this solution into the $x = 1$ boundary condition two equations for ω_m and α_m are obtained, one for the real part of the boundary condition and one for the imaginary part.

$$\begin{aligned} \text{Real:} \quad & \cos(\omega)\cosh(\alpha) - X(\omega)\sin(\omega)\cosh(\alpha) - R(\omega)\cos(\omega)\sinh(\alpha) = 0 \\ \text{Imaginary:} \quad & R(\omega)\sin(\omega)\cosh(\alpha) - X(\omega)\cos(\omega)\sinh(\alpha) - \sin(\omega)\sinh(\alpha) = 0 \end{aligned} \tag{4.16}$$

These equations can be solved numerically. Fig. 4.4 shows a plot of the solutions for the real and imaginary equations for $a = 1$ mm. The intersections of those curves are the eigenvalues of the boundary value problem. It can be seen that the damping of the system α increases with ω. Thus only the first

two or three modes will be important in practical simulations. If the mouth radius a is allowed to go to 0, the zero stress boundary condition is obtained ($\phi_m(1) = 0$). The eigenvalues and eigenfunctions become

$$\begin{aligned} s_m &= i\omega_m = i(2m+1)\frac{\pi}{2} \\ \phi_m(x) &= \cosh(i\omega_m x) = \cos(\omega_m x). \end{aligned} \tag{4.17}$$

Now that the spatial eigenfunctions and eigenvalues have been calculated, I will return to Eq. 4.11 and continue the derivation of the time domain system. From Eq. 4.13, $\phi_m''(x) = s_m^2\phi_m(x)$. Substituting this into Eq. 4.11,

$$\sum_{m=0}^{\infty}(q_m s_m^2 - \ddot{q}_m)\phi_m(x) = u_0 - \ddot{u}_0\frac{(x-1)^2}{2}. \tag{4.18}$$

This can be written as a matrix equation by defining the vector $v_m = q_m s_m^2 - \ddot{q}_m$ and matrix $(\mathbf{\Phi})_{xm} = \phi_m(x)$.

$$\mathbf{\Phi}.\vec{v} = \vec{1}u_0 - \frac{(\vec{x}-1)^2}{2}\ddot{u}_0 \tag{4.19}$$

Because of the inclusion of radiation in the right boundary condition the rows of $\mathbf{\Phi}$ are not orthogonal to each other. They can be rotated into a basis in which they are orthogonal by diagonalizing the overlap matrix $S_{ij} = \int_0^1 \phi_i^*(x)\phi_j(x)dx$. This can be done numerically by computing the eigendecomposition of the overlap matrix $\boldsymbol{S} = \boldsymbol{T}\boldsymbol{\Lambda}\boldsymbol{T}^\dagger$. The matrix $\boldsymbol{T}$ possesses the eigenvectors of $\boldsymbol{S}$ as columns and is unitary. The matrix $\boldsymbol{\Lambda}$ is

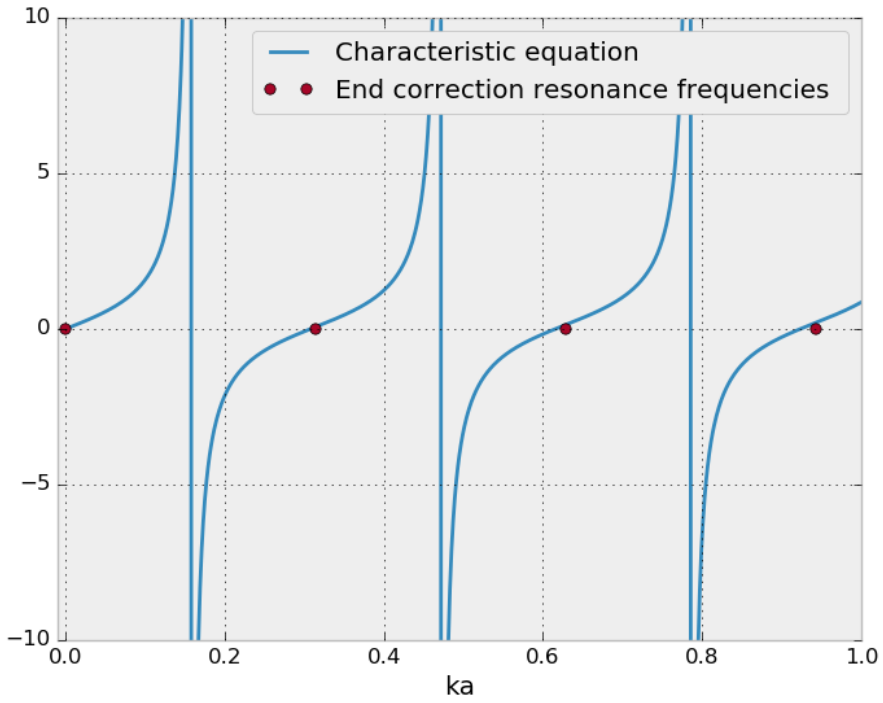

Figure 4.4: Solutions of Eq. 4.16 for $a = 4 \times 10^{-6}$ (1 mm in dimensional units). The purple and green curves show the zero isoclines for the real and imaginary parts of Eq. 4.16. The intersections of these curves are the eigenfrequencies of the half open pipe. The fsolve function, part of the scipy.optimize package, was used to solve this system. The blue circles show initial guesses supplied to fsolve. The red circles show the output of fsolve.

diagonal and has the eigenvalues of $\boldsymbol{S}$ as its nonzero entries. Hence, $\boldsymbol{T}$ rotates $\boldsymbol{S}$ into a basis in which it is diagonal and thus a basis in which the rows of $\boldsymbol{\Phi}$ are orthogonal. We write this new matrix with orthogonal rows as $\widetilde{\boldsymbol{\Phi}} = \boldsymbol{\Phi}.\boldsymbol{T}$. Since $\boldsymbol{T}$ is unitary Eq. 4.19 can be written as

$$\boldsymbol{\Phi}.\boldsymbol{T}.\boldsymbol{T}^{\dagger}.\vec{v} = \vec{1}u_0 - \frac{(\vec{x}-1)^2}{2}\ddot{u}_0 \tag{4.20}$$

Thus,

$$\widetilde{\boldsymbol{\Phi}}.\boldsymbol{T}^{\dagger}.\vec{v} = \vec{1}u_0 - \frac{(\vec{x}-1)^2}{2}\ddot{u}_0 \tag{4.21}$$

Now multiplying this equation by $\widetilde{\boldsymbol{\Phi}}^{\dagger}$,

$$\boldsymbol{\Lambda}.\boldsymbol{T}^{\dagger}.\vec{v} = \widetilde{\boldsymbol{\Phi}}^{\dagger}.\left(\vec{1}u_0 - \frac{(\vec{x}-1)^2}{2}\ddot{u}_0\right), \tag{4.22}$$

using the fact that $\widetilde{\boldsymbol{\Phi}}^{\dagger}.\widetilde{\boldsymbol{\Phi}} = \boldsymbol{\Lambda}$. Now multiplying this equation by $(\boldsymbol{\Lambda}.\boldsymbol{T}^{\dagger})^{-1}$,

$$\vec{v} = \boldsymbol{T}^{\dagger}.\boldsymbol{\Lambda}^{-1}.\widetilde{\boldsymbol{\Phi}}^{\dagger}.\left(\vec{1}u_0 - \frac{(\vec{x}-1)^2}{2}\ddot{u}_0\right). \tag{4.23}$$

Converting this equation back to component form it becomes

$$\ddot{q}_m - s_m^2 q_m = -(\boldsymbol{T}.\boldsymbol{\Lambda}^{-1}.\widetilde{\boldsymbol{\Phi}}^{\dagger}.\vec{1})_m u_0 + (\boldsymbol{T}.\boldsymbol{\Lambda}^{-1}.\widetilde{\boldsymbol{\Phi}}^{\dagger}.\frac{(\vec{x}-1)^2}{2})_m \ddot{u}_0. \tag{4.24}$$

Finally expanding out $s_m^2 = -(\omega_m^2 - \alpha_m^2)\left(1 + i\frac{2\alpha_m\omega_m}{\omega_m^2-\alpha_m^2}\right)$,

$$\ddot{q}_m + (\omega_m^2 - \alpha_m^2)\left(1 + i\frac{2\alpha_m\omega_m}{\omega_m^2 - \alpha_m^2}\right) q_m = -(\boldsymbol{T}.\boldsymbol{\Lambda}^{-1}.\widetilde{\boldsymbol{\Phi}}^{\dagger}.\vec{1})_m u_0 + (\boldsymbol{T}.\boldsymbol{\Lambda}^{-1}.\widetilde{\boldsymbol{\Phi}}^{\dagger}.\frac{(\vec{x}-1)^2}{2})_m \ddot{u}_0. \tag{4.25}$$

4.5 The Viscous Damping Approximation

The term with the imaginary constant in Eq. 4.25 is known as a hysteretic damping term. Although unproblematic in the frequency domain, hysteretic damping results in complications when included in time domain simulations. This is a result of Eq. 4.25 admitting non causal solutions, in addition to the physically meaningful ones. Attempting to enforce causality in numerical time domain simulations is difficult. An alternate method of dealing with this problem is to find an equation that possesses a viscous damping term that is equivalent to the hysteric damping term. This is similar to the procedure discussed by Henwood in [57]. That is if for an equation of the form

$$\ddot{q}_m + \beta_m\dot{q}_m + (\omega_m^2 - \alpha_m^2)q_m = -(\boldsymbol{T}.\boldsymbol{\Lambda}^{-1}.\widetilde{\boldsymbol{\Phi}}^{\dagger}.\vec{1})_m u_0 + (\boldsymbol{T}.\boldsymbol{\Lambda}^{-1}.\widetilde{\boldsymbol{\Phi}}^{\dagger}.\frac{(\vec{x}-1)^2}{2})_m \ddot{u}_0, \tag{4.26}$$

can constants β_m be found such that Eqs. 4.26 approximate Eqs. 4.25? To do this a harmonic solution is assumed, $q_m(t) = e^{i\omega t}$, for the undriven

versions of Eqs. 4.25 and 4.26.

$$\begin{aligned} -\omega_h^2 + (\omega_m^2 - \alpha_m^2)\left(1 + i\frac{2\alpha_m\omega_m}{\omega_m^2 - \alpha_m^2}\right) &= 0 \\ -\omega_v^2 + i\beta_m\omega_v + (\omega_m^2 - \alpha_m^2) &= 0, \end{aligned} \tag{4.27}$$

where the subscripts h and v denote the operating frequencies for the hysteretic and viscous equations respectively. The principle solutions of these equations are

$$\begin{aligned} \omega_h &= \sqrt{\omega_m^2 - \alpha_m^2}\sqrt{1 + i\frac{2\alpha_m\omega_m}{\omega_m^2 - \alpha_m^2}} \\ \omega_v &= \sqrt{\omega_m^2 - \alpha_m^2 - \beta_m^2} + i\frac{\beta_m}{2}. \end{aligned} \tag{4.28}$$

Ideally β_m would be chosen such that $\omega_h = \omega_v$, but this results in an equation with no solution. However a measure of the distance between them can be minimized by solving the equation

$$\frac{\partial}{\partial\beta_m}|\omega_h - \omega_v|^2 = 0, \tag{4.29}$$

which is satisfied when

$$\beta_m = 2\sqrt{\omega_m^2 - \alpha_m^2}\sin\left(\frac{1}{2}\arctan\left(\frac{2\alpha_m\omega_m}{\omega_m^2 - \alpha_m^2}\right)\right) \tag{4.30}$$

Fig. 4.5 shows a comparison of the operating frequencies for the hysteretically and viscously damped oscillator equations. It can be seen that for the first

few mode numbers the approximation is very good, but it starts to diverge at higher mode numbers. This should not pose a problem for my simulations, since I expect only the first few modal equations to be necessary.

Thus, if Eq. 4.30 is used for β_m, the viscous damping in Eq. 4.26 approximate the hysteretic damping in Eq. 4.25. Additionally the viscous damping approximation decouples the real and imaginary parts of Eq. 4.25. Defining $a_m = Re((\boldsymbol{T}.\boldsymbol{\Lambda}^{-1}.\widetilde{\boldsymbol{\Phi}}^{\dagger}.\vec{1})_m)$ and $b_m = Re((\boldsymbol{T}.\boldsymbol{\Lambda}^{-1}.\widetilde{\boldsymbol{\Phi}}^{\dagger}.\frac{(\vec{x}-1)^2}{2})_m)$, the time domain equations can be written as

$$\ddot{q}_m + \beta_m \dot{q}_m + (\omega_m^2 - \alpha_m^2) q_m = -a_m u_0 + b_m \ddot{u}_0. \tag{4.31}$$

This is a time domain representation for the acoustics of the upper vocal tract, with radiation, driven by velocity u_0. The next section will focus on deriving a relationship between u_0, the subglottal pressure p, and the feedback pressure from the upper vocal tract.

4.6 The Flow Through the Vocal Folds

The system given by Eq. 4.25 is a set of time domain damped oscillator equation, whose driving term depends on u_0 and its derivatives. For the system to be a set of fully solvable ODEs, the driving velocity must be expressed in terms of the tracheal pressure and the geometry of the vocal folds. The velocity of the vocal fold flow is on the order of 30 $\frac{m}{s}$, and the

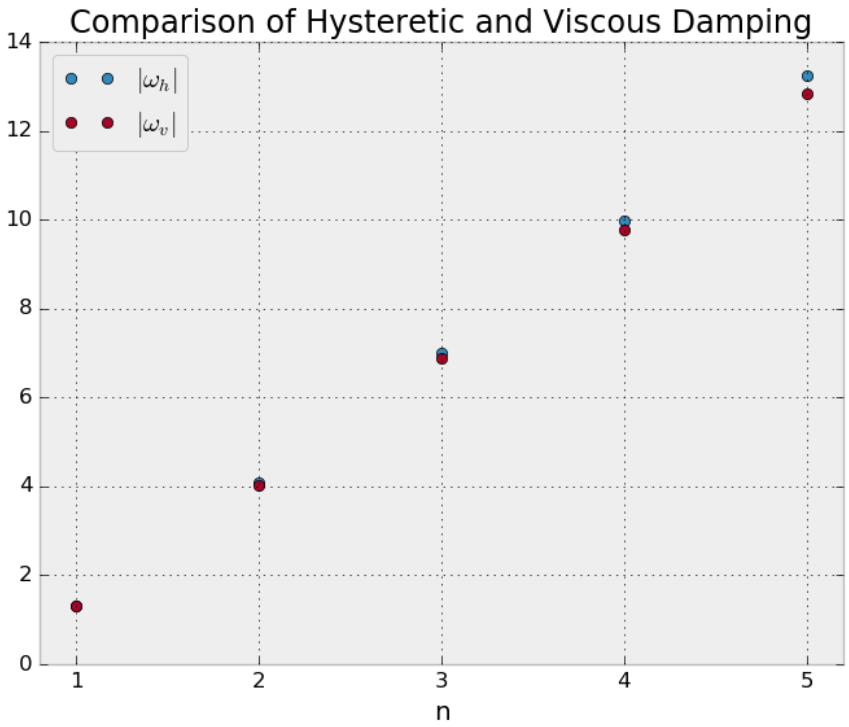

Figure 4.5: A comparison of the operating frequencies for a hysteretically damped oscillator and its viscous damping approximation. Shown is the modulus of the operating frequencies, for the two cases, plotted against mode number. It can be seen that viscous approximation is very good at low mode numbers but starts to diverge at higher ones. This does not pose a problem since only the first few modal equations are used in simulations.

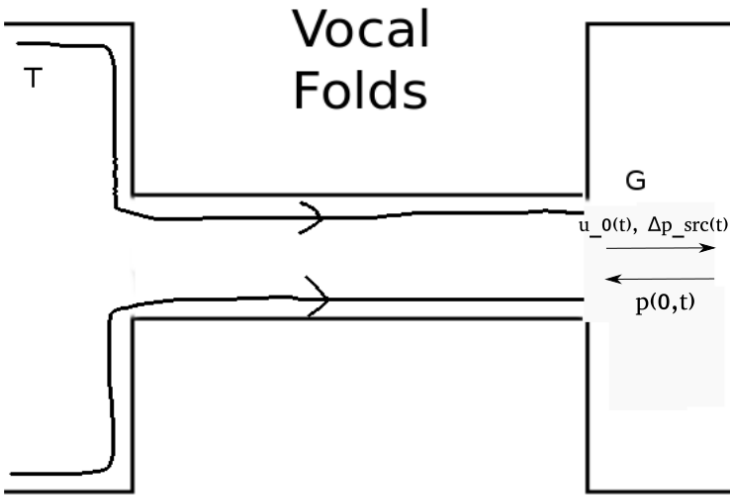

Figure 4.6: Schematic of the flow through the vocal folds. The subglottal pressure focuses air into a jet as it is forced through the vocal folds. The velocity u_0, along with additional pressure sources Δp_{src} emerging from the folds drives resonances in the upper vocal tract. The pressure, at the origin, $p(0,t)$associated with these resonances provides a feedback mechanism that opposes u_0.

vocal radius is on the order of $1\,mm$. So the Reynold's number of the vocal fold flow is on the order of 2000. Thus, it's valid to expect the flow through the vocal folds to be conservative. Therefore it is valid to use Bernoulli's equation to express energy conservation of the flow between the trachea (T) and pharyngeal end of the glottis (G). Fig. 4.6 shows a diagram of the flow through the vocal folds, with the points T and G marked.

$$(p_G - p_T) + \frac{1}{2}(u_G^2 - u_T^2) + \frac{\partial}{\partial t}(\phi_G - \phi_T) = 0. \tag{4.32}$$

The flow through the vocal folds is also assumed to be incompressible. There are no precise measurements for the thickness of the vocal folds. However the shortest acoustic wavelengths emitted by the rodent vocal tract are on the order of $4\,mm$. Incompressibility is a good assumption as long the vocal fold thickness is less than half that. Since the vocal fold radius is about $1\,mm$, this is reasonable even for the highest frequency modes. Thus, from continuity of mass and the incompressibility of the flow, $u_T = \frac{A_G}{A_T} u_G$. Furthermore, the change in velocity potential can be expressed as $\phi_G - \phi_T = \int_T^G u(x)dx$, where $u(x)$ is the axially varying flow velocity inside the folds. Using conservation of mass again this can be written in terms of the velocity at the glottal end $\phi_G - \phi_T = A_G u_G \int_T^G \frac{dx}{A(x)}$, where $A(x)$ is the axially varying area of the folds. Inserting these equations into Eq. 4.32,

$$(p_G - p_T) + \frac{1}{2}u_G^2 \left(1 - \left(\frac{A_G}{A_T}\right)^2\right) + \frac{\partial}{\partial t}\left(A_G u_G \int_T^G \frac{dx}{A(x)}\right) = 0. \tag{4.33}$$

The velocity u_G will be fed into the upper vocal tract exciting acoustic resonances. This is the feed-forward element of the system.

After a short distance the flow emerging from the vocal folds will mix with the acoustic flow of the upper vocal tract. Conservation of mass can be used again to relate the flow emerging from the vocal folds to u_0, the driving

velocity in Eqs. 4.31 and 4.25, $A_G u_G = u_0 A_0$. Inserting this into Eq. 4.33,

$$(p_G - p_T) + \frac{1}{2}u_0^2 \left(\left(\frac{A_0}{A_G} \right)^2 - \left(\frac{A_0}{A_T} \right)^2 \right) + \frac{\partial}{\partial t} \left(A_0 u_0 \int_T^G \frac{dx}{A(x)} \right) = 0. \quad (4.34)$$

By continuity of pressure p_G must equal the acoustic pressure response generated in the upper vocal tract at $x = 0$ plus the pressure from any additional sources driving the acoustic flow. Thus, $p_G = \Delta p_{src} + p(0,t) = \Delta p_{src} - \frac{\partial \phi(0,t)}{\partial t} = \Delta p_{src} - \sum_l \dot{q}_l + \frac{\dot{u}_0}{2}$. This is the feedback condition, since the driving velocity u_0 will excite a pressure response in the resonator, which will impede further flow. The nature of Δp_{src} will be discussed more later. Again by continuity of pressure p_T must equal the pressure in the trachea. This is the input to the system, and it will just be called p, with the understanding that it can be made to vary in time. Inserting these equations into Eq. 4.34,

$$\Delta p_{src} - \sum_l \dot{q}_l + \frac{\dot{u}_0}{2} - p + \frac{1}{2}u_0^2 \left(\left(\frac{A_0}{A_G} \right)^2 - \left(\frac{A_0}{A_T} \right)^2 \right) + \frac{\partial}{\partial t} \left(A_0 u_0 \int_T^G \frac{dx}{A(x)} \right) = 0. \quad (4.35)$$

This equation can be simplified by defining the defining the area rations $C_E = \frac{A_0}{A_G}$ (expansion coefficient) and $C_C = \frac{A_G}{A_t}$ (contraction coefficient.

$$\Delta p_{src} - \sum_l \dot{q}_l + \frac{\dot{u}_0}{2} - p + \frac{C_E^2}{2}u_0^2 \left(1 - C_C^2\right) + \frac{\partial}{\partial t} \left(A_0 u_0 \int_T^G \frac{dx}{A(x)} \right) = 0. \quad (4.36)$$

The derivative term can also be simplified by assuming a profile for the vocal folds. Since detailed measurements of the geometry of the rat vocal folds don't exist, there is little point at this time to attempt to provide precise

numerical predictions. Instead it is of more value to provide mechanistic understanding of the acoustic production mechanism. With this in mind the vocal folds can be assumed to have a linear converging profile. In this case, the axially varying area can be written as

$$A(x) = \left(\sqrt{A_G} - \sqrt{A_{GT}}\right)^2 \left(\frac{x}{l}\right)^2 - 2\sqrt{A_{GT}}\left(\sqrt{A_{GT}} - \sqrt{A_G}\right)\frac{x}{l} + A_{GT}, \tag{4.37}$$

where l is the length of the vocal folds and A_{GT} is the area of the vocal folds on the tracheal side. Eq. 4.37 simplifies somewhat if it is written in terms of $C_F = \frac{A_{TG}}{A_G}$ (the fold coefficient), the area ratio of the tracheal and pharyngeal sides of the vocal folds.

$$\frac{A(x)}{A_G} = \left(1 - \sqrt{C_F}\right)^2 \left(\frac{x}{l}\right)^2 + 2\left(\sqrt{C_F} - C_F\right)\frac{x}{l} + C_F. \tag{4.38}$$

Evaluating the integral in Eq. 4.35

$$A_0 \int_T^G \frac{dx}{A(x)} = C_E \frac{l}{\sqrt{C_F}} = C_E l_e \tag{4.39}$$

where $l_e = \frac{l}{\sqrt{C_F}}$ (the effective length of the vocal folds). An even further simplification is to assume to the profile of the vocal folds is constant. In this case, $C_F = 1$, and the effective length equals the actual length of the vocal folds, $l_e = l$. Inserting these expressions into Eq. 4.35,

$$\Delta p_{src} - \sum_l \dot{q}_l + \frac{\dot{u}_0}{2} - p + \frac{1}{2}u_0^2 C_E^2\left(1 - C_C^2\right) + \frac{\partial}{\partial t}(u_0 C_E l) = 0. \tag{4.40}$$

Is is also reasonable to assume the time derivatives of C_E and l_e are negligible compared to those of u_0 and q_n, since the acoustic oscillations have a much higher frequency than is physically possible for the vocal folds to maintain. Thus, we can take them out of the time derivative in Eq. 4.36

$$\Delta p_{src} - \sum_l \dot{q}_l - p + \frac{1}{2} u_0^2 C_E^2 \left(1 - C_C^2\right) + \left(C_E l + \frac{1}{2}\right) \dot{u}_0 = 0. \tag{4.41}$$

4.41 is a feedback condition, which puts an energy constraint on the solutions of Eq. 4.25. It has the effect of introducing a nonlinearity into the system through its quadratic term, which is responsible for limiting the amplitude of acoustic oscillations. The nonlinear terms has the interpretation of representing the energy loss due to vortex formation as the flow passes around sharp edges.

4.7 The Time Domain ODEs

Eqs. 4.31 and 4.41 form a differential algebraic system that must be solved for a set of ODEs. To do this first solve Eq. 4.41 for $\dot{u}_0$,

$$\dot{u}_0 = \mu^{-1} \left(p - \Delta p_{src} + \sum_l \dot{q}_l - \frac{\gamma}{2} u_0^2 \right), \tag{4.42}$$

where the substitutions $\mu = C_E l + \frac{1}{2}$ and $\gamma = C_E^2(1 - C_C^2)$ have been made. Now differentiating Eq. 5.75 with respect to time,

$$\ddot{u}_0 = \mu^{-1}\left(-\frac{\partial \Delta p_{src}}{\partial t} + \sum_l \ddot{q}_l - \gamma u_0 \dot{u}_0\right), \tag{4.43}$$

where it has been assumed the pressure varies slowly enough to be treated quasi statically. This assumption may need to be relaxed at some point.

Now substituting Eq. 4.43 into Eq. 4.31,

$$\ddot{q}_m + \beta_m \dot{q}_m + (\omega_m^2 - \alpha_m^2) q_m = -a_m u_0 + \frac{b_m}{\mu}\left(-\frac{\partial \Delta p_{src}}{\partial t} + \sum_l \ddot{q}_l - \gamma u_0 \dot{u}_0\right). \tag{4.44}$$

Moving the $\sum_l \ddot{q}_l$ term to the left hand side,

$$\sum_l \left(\delta_{ml} - \frac{b_m}{\mu}\right)\ddot{q}_l + \beta_m \dot{q}_m + (\omega_m^2 - \alpha_m^2) q_m = -a_m u_0 + \frac{b_m \gamma}{\mu}\left(-\frac{\partial \Delta p_{src}}{\partial t} - u_0 \dot{u}_0\right). \tag{4.45}$$

This is a matrix equation, which must be solved for $\ddot{q}_n$. To do this multiply by the matrix $\mathbf{M}$, where $M_{ml}^{-1} = \delta_{ml} - \frac{b_m}{\mu}$,

$$\ddot{q}_n + \sum_m M_{nm}\beta_m \dot{q}_m + \sum_m M_{nm}(\omega_m^2 - \alpha_m^2) q_m = -A_n u_0 + \frac{B_n \gamma}{\mu}\left(-\frac{\partial \Delta p_{src}}{\partial t} - u_0 \dot{u}_0\right), \tag{4.46}$$

where $A_n = \sum_m M_{nm} a_m$ and $B_n = \sum_m M_{nm} b_m$. Finally, we substitute Eq. 5.75 into Eq. 4.46 to get Eq. 4.46. Our set of time domain ODEs for the

variables $(u_0, ..., q_n, ...\dot{q}_n, ...)$ is then

$$\dot{u}_0 = \mu^{-1}\left(p - \Delta p_{src} + \sum_l \dot{q}_l - \frac{\gamma}{2}u_0^2\right) \tag{4.47}$$

$$\ddot{q}_n + \sum_m M_{nm}\beta_m\dot{q}_m + \sum_m M_{nm}(\omega_m^2 - \alpha_m^2)q_m = \\ -\frac{B_n\gamma}{\mu}\frac{\partial\Delta p_{src}}{\partial t} + B_n\frac{\gamma}{\mu^2}u_0\Delta p_{src} - \left(A_n + B_n\frac{\gamma}{\mu^2}p\right)u_0 - B_n\frac{\gamma}{\mu^2}\left(u_0\sum_m \dot{q}_m - \frac{\gamma}{2}u_0^3\right). \tag{4.48}$$

Bringing the nonlinear dissipation term to the left side

$$\ddot{q}_n + \sum_m (M_{nm}\beta_m + B_n\frac{\gamma}{\mu^2}u_0)\dot{q}_m + \sum_m M_{nm}(\omega_m^2 - \alpha_m^2)q_m = \\ -\frac{B_n\gamma}{\mu}\frac{\partial\Delta p_{src}}{\partial t} + B_n\frac{\gamma}{\mu^2}u_0\Delta p_{src} - \left(A_n + B_n\frac{\gamma}{\mu^2}p\right)u_0 + B_n\frac{\gamma^2}{2\mu^2}u_0^3. \tag{4.49}$$

Writing this in vector form it becomes

$$\vec{\ddot{q}} + \boldsymbol{D}\vec{\dot{q}} + \frac{\gamma}{\mu^2}u_0\vec{B}\cdot\vec{\dot{q}} + \boldsymbol{K}\vec{q} = -\vec{B}\frac{\gamma}{\mu}\frac{\partial\Delta p_{src}}{\partial t} + \vec{B}\frac{\gamma}{\mu^2}u_0\Delta p_{src} - \left(\vec{A} + \vec{B}\frac{\gamma}{\mu^2}p\right)u_0 + \vec{B}\frac{\gamma^2}{2\mu^2}u_0^3, \tag{4.50}$$

where the matrices $D_{nm} = M_{nm}\beta_m$ and $K_{nm} = M_{nm}(\omega_m^2 - \alpha_m^2)$.

To gain some understanding of the system it is helpful to consider the situation in which $\Delta p_{src} = 0$. In this case, the resonance modes are only driven by the laminar flow emerging from the vocal folds. The governing

equations become

$$\begin{aligned} \dot{u}_0 &= \mu^{-1}\left(p + \sum_l \dot{q}_l - \frac{\gamma}{2}u_0^2\right) \\ \ddot{\vec{q}} + \boldsymbol{D}\dot{\vec{q}} + \frac{\gamma}{\mu^2}u_0\vec{B}\cdot\dot{\vec{q}} + \boldsymbol{K}\vec{q} &= -\left(\vec{A} + \vec{B}\frac{\gamma}{\mu^2}p\right)u_0 + \vec{B}\frac{\gamma^2}{2\mu^2}u_0^3. \end{aligned} \tag{4.51}$$

This system has fixed points given by

$$\begin{aligned} u_0^* &= \pm\sqrt{\frac{2p}{\gamma}} \\ q_n^* &= \mp\frac{a_n}{\omega_n^2 - \alpha_n^2}\sqrt{\frac{2p}{\gamma}} \end{aligned} \tag{4.52}$$

Only the fixed point with positive u_0^* is relevant to this analysis. When considering the flow through the vocal folds it was assumed that air flowed in one direction. The fixed point with negative u_0^* contradicts this assumption, and any conclusions drawn about it should be suspect. Fig. 4.7 shows the behavior of the real part of the least stable eigenvalue of the Jacobian for the fixed point with positive u_0^*. The eigenvalue is plotted against subglottal pressure p for different values of the mouth radius a. This plot extends beyond the physiological realistic range of subglottal pressures, since it has been measured that p takes values between $1 - 1.5$ kPa during vocalizations [38]. It can be seen that the system is stable for values of these parameters. Increasing subglottal pressure actually makes the system more stable. Decreasing a makes the system less stable, which is to be expected since this decreases radiation losses. However, even when energy losses due to radiation

are allowed to be zero ($a = 0$) the system remains stable. This is because the nonlinear damping caused by dissipation of potential flow due to vorticity always overcomes the driving due to laminar flow. This highlights the importance of a time-dependent Δp_{src}, similar to Eq. 4.6. The modeling of this pressure source is an ongoing area of research for me. A first attempt is discussed in the next chapter.

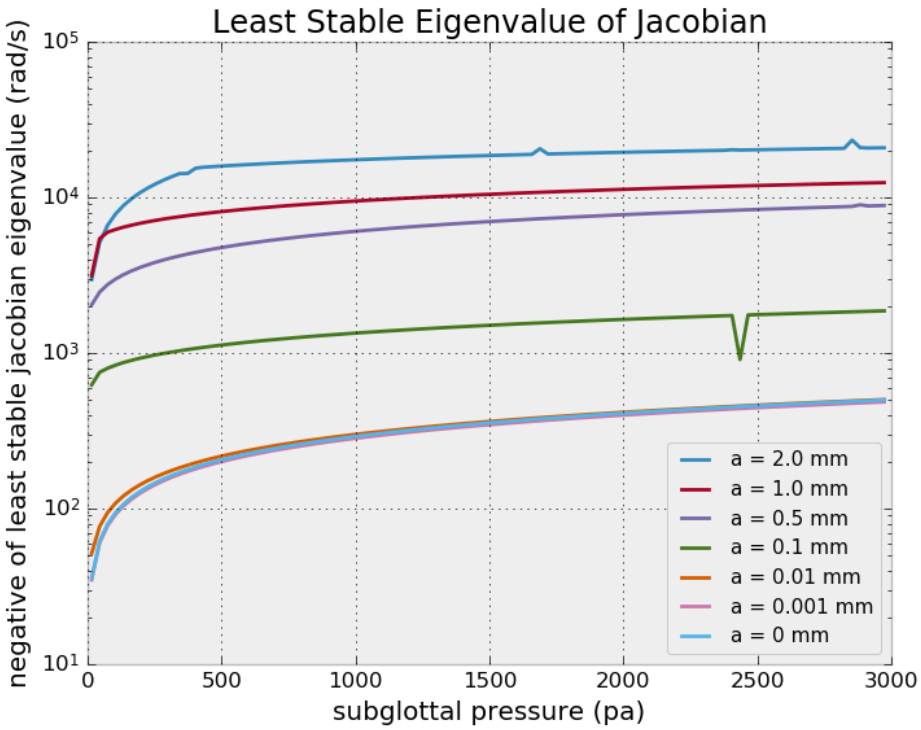

Figure 4.7: The negative of the least stable eigenvalue of the Jacobian of Eq. 4.49, evaluated at the system's stable fixed point. The eigenvalue is plotted against subglottal pressure for $\Delta p_{src} = 0$ for different values of a, the radius of the far end of the pipe, which corresponds to the mouth of a rat. Decreasing a causes a decrease in stability of the fixed point. As a decreases the fixed point becomes less stable but never crosses the stability axis. It can be seen without any unsteady p_{src}, an increase in subglottal pressure makes the fixed point more stable.

Chapter 5

The Force Due to Vorticity

5.1 Introduction

In chapter 4 a set of time domain equations, which describe the acoustic oscillations of a one dimensional pipe, were derived. It was found that, if the pipe is driven by a laminar potential jet, oscillations will decay exponentially. This is not what would be expected from an actual acoustic system, since it is quite clear that musical instruments and vocal systems are capable of sustaining steady oscillations as long as air is supplied from a source, such as the lungs.

A pertinent question is then what physical mechanism is missing from the derivation of the previous chapter? In the work performed by Auvray et al on the acoustics of recorders and organ pipes[56], this mechanism is the unsteady force supplied by a jet oscillating above and below the edge of

the entrance to the resonance pipe. However, in the axisymmetric system no such edge exists. The entire volume of the jet expands and mixes with the acoustic flow of the resonance pipe. Thus, it must be another mechanism which provides this unsteady force. It is the hypothesis of this chapter that the growth in vorticity of the boundary of the potential jet is the source of this force. This was neglected in the derivation of the previous chapter, in which the jet flow was assumed to irrotational. Modeling of this force is an ongoing area of research. This chapter will discuss some first attempts at quantifying this force. First, it will be discussed how the force follows from the definition of vortical impulse. Second, the force will be approximated using the linearized equations of motion for a fluid. Last, the shortcomings of this approach will be discussed, and a nonlinear approach will be taken.

5.2 The Force Due to Unsteady Vorticity

Again thinking of the upper vocal tract as a pipe of volume V. Defining the vorticity in the pipe and flow velocity $\mathbf{v}$ to be $\boldsymbol{\omega}(\mathbf{r},t) = \nabla \times \mathbf{v}(\mathbf{r},t)$. Vladimirov defined the impulse required to generate the observed motion from rest to be

$$\mathbf{P} = \frac{\rho}{2}\int_V dV\,(\mathbf{r}\times\boldsymbol{\omega}(\mathbf{r},t))\,, \tag{5.1}$$

where the volume integral is taken over the pipe plus the fluid exterior to the exit, which goes off to infinity [58]. The flow exterior to the pipe exit mostly consists of acoustic radiation, which decays as it travels through space

according to an inverse square law. Thus, this flow is practically negligible and for practical purposes the integral can be taken over the volume of the pipe. The force required to generate this motion is the time derivative of the impulse

$$\mathbf{F}_\omega = \frac{\partial \mathbf{P}}{\partial t} = \frac{\rho}{2}\frac{\partial}{\partial t}\int_V dV\left(\mathbf{r}\times\boldsymbol{\omega}(\mathbf{r},t)\right). \tag{5.2}$$

Since energy flow into the upper vocal tract comes from air emerging from the vocal folds. In the one dimensional treatment of chapter 4 it is reasonable to think of $\mathbf{F}_\omega$ as a surface force localized at the entrance to the pipe. This force is then associated with a pressure source at the entrance to the pipe

$$\Delta p_{src} = \frac{\mathbf{F}_\omega}{\pi r_0^2} = \frac{\rho}{2\pi r_0^2}\frac{\partial}{\partial t}\int_V dV\left(\mathbf{r}\times\boldsymbol{\omega}(\mathbf{r},t)\right), \tag{5.3}$$

where πr_0^2 is the cross sectional area of the upper vocal tract. Hence, the problem has been transformed to modeling the time domain behavior of $\boldsymbol{\omega}(\mathbf{r},t)$, the vorticity inside the upper vocal tract. The growth of jet vorticity is usually analyzed by considering the linearized momentum and mass conservation equations in the frequency domain. This approach will be discussed in the next section. Following that it's shortcomings will be discussed and why it is incompatible with the time domain equations of chapter 4.

5.3 Linear Vorticity Evolution in a Pipe

This section focuses on calculating the linear behavior of the azimuthal vorticity ω_ϕ in an axisymmetric, incompressible, high Reynold's number flow in an infinite long pipe of radius r_0. First the linearized flow equations must be derived. To do this the flow is separated into mean and fluctuating parts. The mean flow will be assumed to have a hyperbolic tangent profile, which is a good approximation for the flow of a circular jet.

$$\mathbf{U} = \frac{U_0}{2} \tanh\left(\frac{r_f}{4\delta}\left(\frac{r_f}{r} - \frac{r}{r_f}\right)\right)\hat{r} \tag{5.4}$$

In this expression U_0 is the centerline velocity of the jet. The quantity r_f is the radius of the jet. If the jet is thought of as emerging from the vocal folds then the radius of the jet is equal to the radius of the vocal folds. The quantity δ is the half-width of the vorticity layer. The vocal fold radius is taken to be $r_f = 1$ mm. The upper vocal tract radius is taken to be $r_0 = 3$ mm, and the half-width of the vorticity region is taken to be $\delta \approx 0.16$ mm, which experimentally has been shown to be a good approximation to an actual jet with that radius [59]. Fig. 5.1 shows a plot of the axial component of the mean flow over the radial coordinate in nondimensional units. It can be seen that hyperbolic tangent profile captures the behavior of a jet, which has approximately constant velocity in the center. The velocity of the jet then decreases through a vorticity region and is zero outside that region.

In the rest of this chapter the following nondimensionalized units will be

used.

$$u^* = \frac{u}{U_0}, \quad r^* = \frac{2r}{r_0}, \quad p^* = \frac{p}{\rho U_0^2} \tag{5.5}$$

So all velocities will be nondimensionalized by the centerline velocity of the mean flow U_0. Distances will be nondimensionalized by the radius of the pipe r_0. Pressure is nondimensionalized by the density of air and the centerline velocity of the mean flow. The factor of 2 in the distance nondimensionalization is to transform the radial coordinates to the interval $[0, 2]$, which will allow the use of the spectral collocation to solve boundary value problems. This will be discussed more later. From now on the stars will be dropped, and all quantities will be understood to be nondimensional. In these units, the mean flow becomes

$$\mathbf{U} = \frac{1}{2} \tanh \left(\frac{r_f}{4\delta} \left(\frac{2r_f/r_0}{r} - \frac{r}{2r_f/r_0} \right) \right) \hat{r} \tag{5.6}$$

5.3.1 The Linearized Flow Equations

The incompressible Euler equations in these units are

$$\begin{aligned} \frac{D\mathbf{u}}{Dt} &= -\nabla p \\ \nabla \cdot \mathbf{u} &= 0 \end{aligned} \tag{5.7}$$

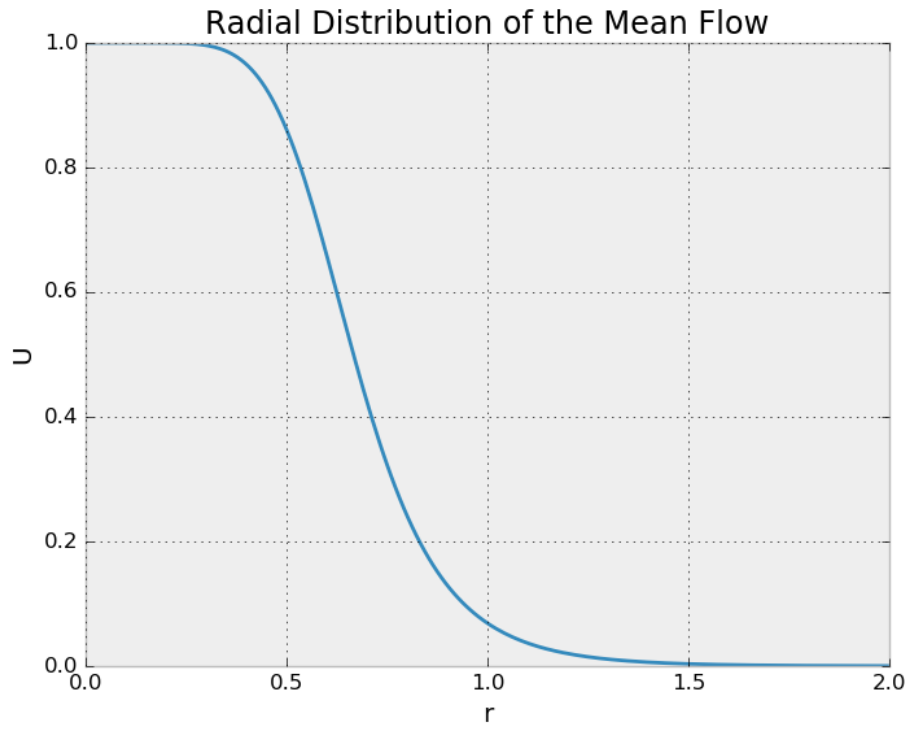

Figure 5.1: Mean flow profile of the jet.

Splitting the flow variables into a mean and fluctuating part,

$$\begin{aligned} \mathbf{u} &= \mathbf{U} + \mathbf{u}' \\ p &= P + p' \end{aligned} \tag{5.8}$$

Here $\mathbf{u}' = u\hat{x} + v\hat{r}$ is the axisymmetric disturbance velocity. Substituting Eqs. 5.8 into Eq. 5.7, subtracting off the mean flow equation, and neglecting terms nonlinear in the fluctuating quantities, the linear disturbance equation is obtained.

$$\begin{aligned} \frac{\partial \mathbf{u}'}{\partial t} + U\frac{\partial \mathbf{u}'}{\partial x} + v\frac{\partial \mathbf{U}}{\partial r} &= -\nabla p' \\ \nabla \cdot \mathbf{u}' &= 0 \end{aligned} \tag{5.9}$$

Taking the divergence of the linear momentum equation and using the linear continuity equation an equation for the pressure for the pressure is obtained

$$\nabla^2 p = -2U'\frac{\partial v}{\partial x}. \tag{5.10}$$

In component form Eq. 5.9 is

$$\begin{aligned} \frac{\partial v}{\partial t} + U\frac{\partial v}{\partial x} &= -\frac{\partial p}{\partial r} \\ \frac{\partial u}{\partial t} + U\frac{\partial u}{\partial x} + vU' &= -\frac{\partial p}{\partial x} \\ \frac{\partial v}{\partial r} + \frac{\partial u}{\partial x} &= 0 \end{aligned} \tag{5.11}$$

Taking the derivative with respect to r of Eq. 5.10 and using the first of Eqs. 5.11 the equation, which describes the linear behavior of the radial velocity v, is obtained. The analysis can be completely done on the radial velocity, and the behavior of the other flow variables can be obtained from that result.

$$\left[\left(\frac{\partial}{\partial t}+U\frac{\partial}{\partial x}\right)\left(\nabla^2-\frac{1}{r^2}\right)-\left(U''-\frac{U'}{r}\right)\frac{\partial}{\partial x}\right]v=0 \tag{5.12}$$

Two separate approaches are taken in calculating the linearized behavior of flow disturbances: the temporal approach and the spatial approach. In the temporal approach the system is prepared in an initial state $v(r,x,0)$. The response of the fluctuations are then calculated as they grow in time. In the spatial approach the system is driven by a source at the origin $v(r,0,t)$. The response of the fluctuations is then calculated as they grow and convect along in space. These two approaches will now be discussed in more depth. The code required to run these simulations can be found at https://gitlab.com/mdornfe1/linear_growth.git

5.3.2 The Chebyshev Method

In the next section Eq. 5.12 will be analyzed using the Chebyshev method, which can be used to approximate the solutions to continuous boundary eigenvalue problems, such as Eqs. 5.26 and 5.50. So as a brief aside the basics of the Chebyshev method will be discussed. To perform this analysis the spatial coordinate is discretized by N points according to the following

scheme.

$$r_j = \cos\left(\frac{j\pi}{N}\right) \quad j = 0, 1, ..., N \tag{5.13}$$

Derivatives $\frac{\partial}{\partial r}$ are then approximated with differentiation matrices D_N, which are defined by

$$(D_N)_{ij} = \begin{cases} \frac{2N^2+1}{6} & i = j = 0 \\ -\frac{2N^2+1}{6} & i = j = N \\ -\frac{x_j}{2(1-x_j^2)} & i = j = 1, ..., N-1 \\ \frac{c_i}{c_j}\frac{(-1)^{i+j}}{x_i - x_j} & i \neq j \quad i, j = 1, ..., N-1 \end{cases} \tag{5.14}$$

where

$$c_i = \begin{cases} 2 & i = 0, N \\ 1 & \text{otherwise} \end{cases} \tag{5.15}$$

With the derivatives approximated by matrices the eigenvalue problems can be solved using functions available for solving matrix eigenvalue problems, which are available in most scientific computing packages. An in depth review of the Chebyshev method has been written by Trefethen [60].

5.3.3 The Temporal or Initial Value Problem

In the temporal problem the evolution of the initial state of the system $v(r, x, 0)$ is calculated based on the linear filtering properties of the pipe. To calculate this behavior the system is Fourier transformed in the x coordinate

and Laplace transformed in the t coordinate.

$$\hat{v}(r,x,\omega) = \int_0^\infty v(r,x,t)e^{i\omega t}dt \quad v(r,x,t) = \frac{1}{2\pi}\int_{C_\omega} \hat{v}(r,x,\omega)e^{-i\omega t}d\omega, \quad (5.16)$$

$$\tilde{v}(r,\alpha,\omega) = \int_{-\infty}^\infty \hat{v}(r,x,\omega)e^{-i\alpha x}dx \quad \hat{v}(r,x,\omega) = \frac{1}{2\pi}\int_{-\infty}^\infty \tilde{v}(r,\alpha,\omega)e^{i\alpha x}d\alpha, \quad (5.17)$$

Using Eq. 5.16 to transform the t coordinate in Eq. 5.12,

$$\left[\left(i\omega + U\frac{\partial}{\partial x}\right)\left(\nabla^2 - \frac{1}{r^2}\right) - \left(U'' - \frac{U'}{r}\right)\frac{\partial}{\partial x}\right]\hat{v} = f_0(r,x), \quad (5.18)$$

where the inhomogeneous term represents the effects of the initial conditions.

$$f_0(r,x) = \left(\nabla^2 - \frac{1}{r^2}\right)v(r,x,0). \quad (5.19)$$

The inhomogeneous term enters the expression due to the derivative properties of the Laplace transform.

$$\hat{v}(r,x,\omega) = \int_0^\infty \frac{\partial v(r,x,t)}{\partial t}e^{i\omega t}dt = i\omega\hat{v}(r,x,\omega) - v(r,x,0). \quad (5.20)$$

Now using Eq. 5.17 to perform the Fourier transform of the x coordinate,

$$\left[(\omega - \alpha U)\left(D^2 + \frac{D}{r} - \frac{1}{r^2} - \alpha^2\right) + \alpha\left(U'' - \frac{U'}{r}\right)\right]\tilde{v}(r,\alpha,\omega) = -i\tilde{f}_0(r,\alpha), \quad (5.21)$$

where the inhomogeneous driving term is defined as

$$\tilde{f}_0(r,\alpha) = \left(D^2 - \frac{D}{r} - \frac{1}{r^2} - \alpha^2\right)\tilde{v}(r,\alpha,0). \tag{5.22}$$

Now defining the operator

$$\mathbf{L}(\alpha,\omega) = (\omega - \alpha U)\left(D^2 + \frac{D}{r} - \frac{1}{r^2} - \alpha^2\right) + \alpha\left(U'' - \frac{U'}{r}\right), \tag{5.23}$$

the boundary value problem in Fourier-Laplace space can be written as

$$\begin{aligned} \mathbf{L}(\alpha,\omega)\tilde{v}(r,\alpha,\omega) &= -i\tilde{f}_0(r,\alpha) \\ \tilde{v}(0,\alpha,\omega) &= 0 \\ \tilde{v}(2,\alpha,\omega) &= 0 \end{aligned} \tag{5.24}$$

The boundary condition at $r = 2$ comes from the no penetration condition at the pipe wall. The boundary condition at $r = 0$ comes from considerations discussed by Batchelor [61].

The response of the system to the initial conditions $v(r,x,0)$ can be expressed in terms of the eigenfunctions of $\mathbf{L}(\alpha,\omega)$, but first the dispersion relation $\mathbf{D}(\alpha,\omega) = 0$, which gives the relationship between α and ω, must be found. This can be accomplished by solving the homogeneous version of Eq.

5.24.

$$\begin{aligned} \mathbf{L}(\alpha,\omega)\tilde{v}_h(r,\alpha,\omega) &= 0 \\ \tilde{v}_h(0,\alpha,\omega) &= 0 \\ \tilde{v}_h(2,\alpha,\omega) &= 0 \end{aligned} \tag{5.25}$$

For the temporal problem, this procedure consists of choosing a real α from an interval, solving Eq. 5.25 for a complex ω, then repeating that procedure for a finite number of α from that interval. Eq. 5.25 can be rewritten as a generalized eigenvalue problem in which ω is the eigenvalue.

$$\begin{aligned} \alpha\left[U\left(D^2+\frac{D}{r}-\frac{1}{r^2}-\alpha^2\right)-\alpha\left(U''-\frac{U'}{r}\right)\right]\tilde{v}_h(r,\alpha,\omega) &= \omega\left(D^2+\frac{D}{r}-\frac{1}{r^2}-\alpha^2\right)\tilde{v}_h(r,\alpha,\omega) \\ \tilde{v}_h(0,\alpha,\omega) &= 0 \\ \tilde{v}_h(2,\alpha,\omega) &= 0 \end{aligned} \tag{5.26}$$

This problem can be solved numerically using the Chebyshev method. To do this the operator D is a approximated using the Chebyshev differentiation matrix. The homogeneous boundary conditions are taken into account by deleting the outer most rows and columns. The eigenvalues ω and eigenvectors $\tilde{v}_h(r,\alpha,\omega)$ are then computed using the function for solving generalized eigenvalue problems, which are available in most scientific programming software. Fig. 5.2 shows the eigenvalues of Eq. 5.26 for the most unstable value of $\alpha \approx 35.2$. These are the values of ω that satisfy $\mathbf{D}(\alpha,\omega)=0$ for that value

of α. This distribution of eigenvalues is characteristic of temporal stability problems. Generally most eigenvalues are real and do not contribute to the instability of the flow. There is usually one complex conjugate pair of eigenvalues, that lie off the real axis. By examining the definition of the inverse Laplace transform in Eq. 5.16 it can be seen the eigenvalue with positive imaginary part contributes to the instability of the flow. This eigenvalue will be denoted $\omega_{unstable}(\alpha)$ Fig. 5.3 shows the real and imaginary parts of the most unstable ω for a sampling of α in the range $[-49.8, 49.8]$. The system is neutrally stable for $\alpha < 0$. It is most unstable for $\alpha \approx 35.2$ the decreases back to 0. The system remains approximately neutrally stable for values of α greater than this.

Now that the solution method of $\mathbf{D}(\alpha, \omega) = 0$ has been discussed the solution of Eq. 5.24 can be formulated in terms of the eigenvectors of $L(\alpha, \omega)$ and the problem can be transformed back into x and t coordinates. The eigenvalue problem for the operator $L(\alpha, \omega)$ can be written as

$$\mathbf{L}(\alpha, \omega)\tilde{v}_n(\alpha, \omega) = \lambda_n(\alpha, \omega)\tilde{v}_n(\alpha, \omega), \tag{5.27}$$

where $\lambda_n(\alpha, \omega)$ are its eigenvalues and $\tilde{v}_n(\alpha, \omega)$ are its eigenvectors.Expanding the solutions and driving term of Eq. 5.24 on to the eigenvectors,

$$\begin{aligned} \tilde{v} &= \sum_n a_n \tilde{v}_n \\ \tilde{f}_0 &= \sum_n f_n \tilde{v}_n, \end{aligned} \tag{5.28}$$

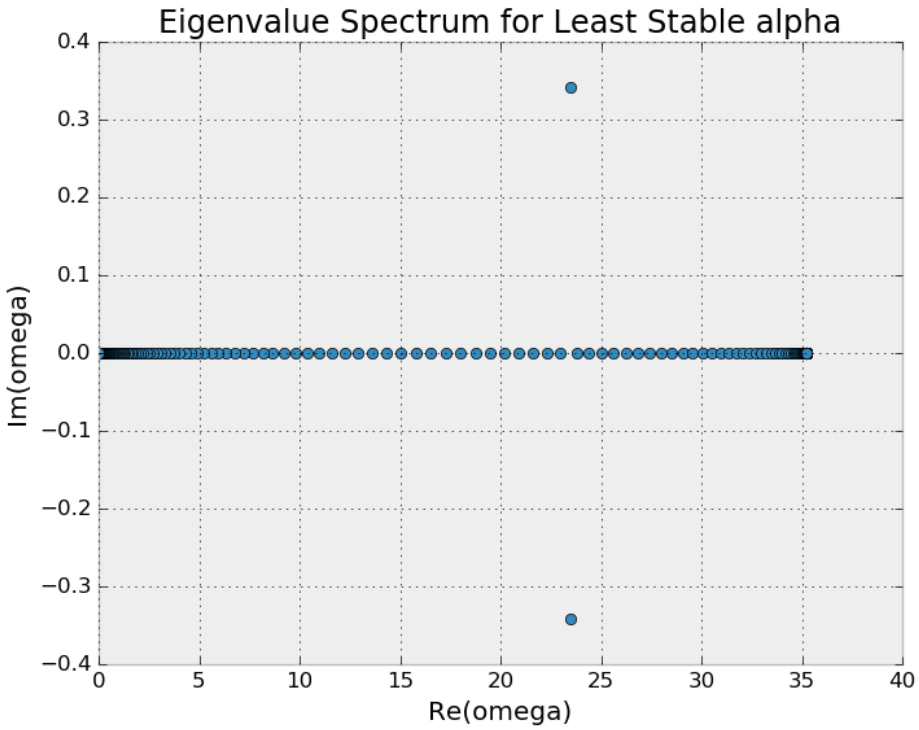

Figure 5.2: The eigenvalues of the generalized eigenvalue problem Eq. 5.26 for the most unstable value of $\alpha \approx 35.2$. This distribution of eigenvalues is characteristic of temporal stability problems. Generally most eigenvalues are real and do not contribute to the instability of the flow. There is usually one complex conjugate pair of eigenvalues, that lie off the real axis. The eigenvalue with positive imaginary part contributes to the instability of the flow.

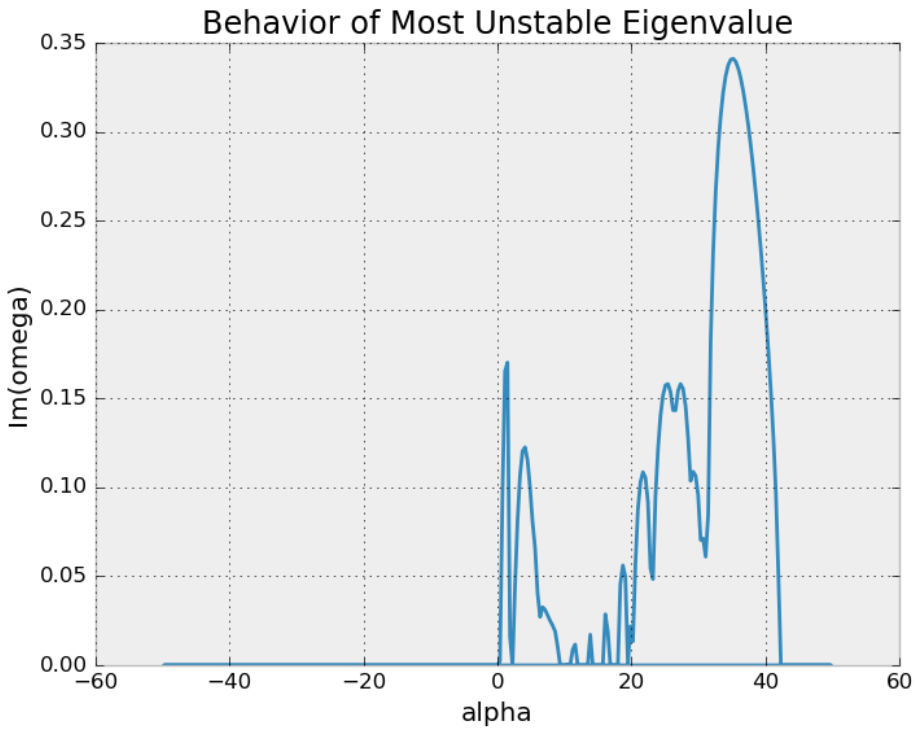

Figure 5.3: Real and imaginary parts of the most unstable ω as a function of α. The system is neutrally stable for $\alpha < 0$. It is must unstable for $\alpha \approx 35.2$ the decreases back to 0. The system remains approximately neutrally stable for values of α greater than this.

where is the inner product of $\tilde{f}_0(r,\alpha)$ and the n^{th} eigenvector.

$$f_n = (\tilde{f}_0(r,\alpha), \tilde{v}_n(r,\alpha)) = \int_0^2 dr \tilde{f}_0^*(r,\alpha)\tilde{v}_n(r,\alpha) \tag{5.29}$$

Plugging these back into the original problem

$$\sum_n a_n \lambda_n \tilde{v}_n = \sum_n f_n \tilde{v}_n. \tag{5.30}$$

The operator $\mathbf{L}(\alpha,\omega)$ is hermitian, so its eigenvectors will be orthogonal. Hence,

$$a_n = \frac{f_n}{\lambda_n} = \frac{(\tilde{f}_0(r,\alpha), \tilde{v}_n(r,\alpha))}{\lambda_n(\alpha,\omega)} \tag{5.31}$$

and,

$$\tilde{v}(r,\alpha,\omega) = \sum_n \frac{(-i\tilde{f}_0(r,\alpha), \tilde{v}_n(r,\alpha))}{\lambda_n(\alpha,\omega)} \tilde{v}_n(r,\alpha,\omega) \tag{5.32}$$

Now performing the inverse Laplace transform on the ω coordinate,

$$\hat{v}(r,\alpha,t) = \frac{1}{2\pi}\int_{C_\omega} d\omega \left(\sum_n \frac{(-i\tilde{f}_0(r,\alpha), \tilde{v}_n(r,\alpha))}{\lambda_n(\alpha,\omega)} \tilde{v}_n(r,\alpha) \right) e^{-i\omega t}. \tag{5.33}$$

At this point the utility of computing the dispersion relation $\mathbf{D}(\alpha,\omega) = 0$ is becoming more apparent. The curve C_ω is a closed contour, and by the residue theorem only poles enclosed by this contour should contribute to the integral. From Eq. 5.33 it can be seen that the poles enclosed by the contour are the values ω that corresponds to zero eigenvalues of the operator $\mathbf{L}(\alpha,\omega)$. Furthermore, the values of ω that result in $\lambda_n(\alpha,\omega) = 0$ have already been

computed, and they are the solutions of the dispersion relation $\mathbf{D}(\alpha, \omega) = 0$, since when the dispersion relation is satisfied, by definition from Eq. 5.25 the eigenvalue problem becomes homogeneous. Denoting the discrete solutions of the dispersion relation in the ω plane as ω_m, the solution in the (α, t) coordinate system can be written as

$$\hat{v}(r, \alpha, t) = \sum_m (\tilde{f}_0(r, \alpha), \tilde{v}_h(r, \alpha, \omega_m))\tilde{v}_h(r, \alpha, \omega_m)e^{-i\omega_m(\alpha)t}. \tag{5.34}$$

Now performing the inversion in the alpha coordinate,

$$v(r, x, t) = \frac{1}{2\pi}\sum_m \int_{-\infty}^{\infty} d\alpha(\tilde{f}_0(r, \alpha), \tilde{v}_h(r, \alpha, \omega_m))\tilde{v}_h(r, \alpha, \omega_m)e^{i(\alpha x - \omega_m(\alpha)t)}. \tag{5.35}$$

Thus, it can be the seen the response is the discrete sum of continuous wave packets. Furthermore, as t increases only the disturbances with an unstable value of omega will make a noticable contribution to the flow. Thus, only the terms with $\omega_m(\alpha) = \omega_u(\alpha)$ and $\tilde{v}_h(r, \alpha, \omega_m(\alpha)) = \tilde{v}_h(r, \alpha, \omega_u(\alpha)) = \tilde{v}_u(r, \alpha)$ will make appreciable contributions to the sum.

$$v(r, x, t) = \frac{1}{2\pi}\int_{-\infty}^{\infty} d\alpha(\tilde{f}_0(r, \alpha), \tilde{v}_u(r, \alpha))\tilde{v}_u(r, \alpha)e^{i(\alpha x - \omega_u(\alpha)t)}. \tag{5.36}$$

The stream function can immediately be calculated from $v = -\frac{1}{r}\frac{\partial \psi}{\partial x}$.

$$\psi(r, x, t) = \frac{ri}{2\pi}\int_{-\infty}^{\infty} d\alpha \frac{(\tilde{f}_0(r, \alpha), \tilde{v}_u(r, \alpha))}{\alpha}\tilde{v}_u(r, \alpha)e^{i(\alpha x - \omega_u(\alpha)t)}. \tag{5.37}$$

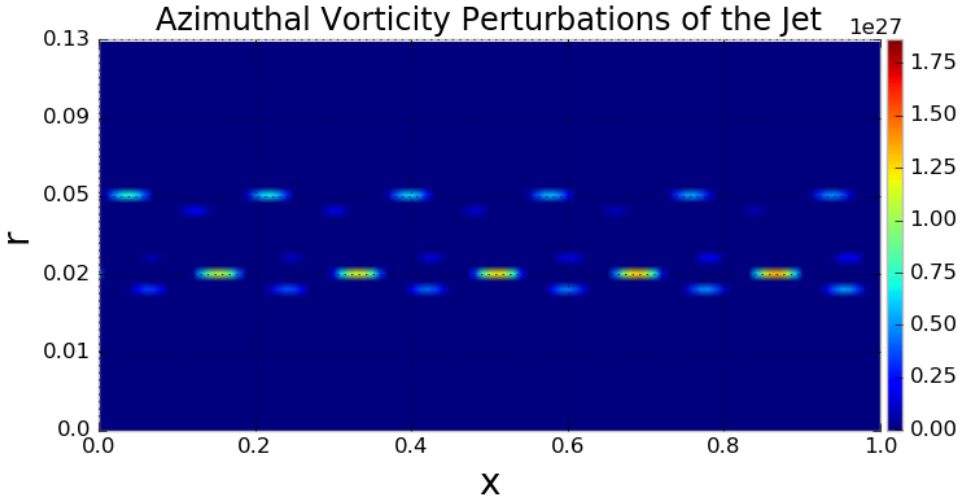

Figure 5.4: A heat map of the azimuthal vorticity perturbations at time $t = 200$, for an axisymmetric jet with a hyperbolic tangent mean flow profile. Gaussian noise was used as the initial condition for the radial velocity perturbation $v(r, x, t)$. It can be seen that the vorticity concentrates itself into discrete structures resembling vortex rings.

The azimuthal vorticity can then be calculated from $\omega_\phi = -\nabla^2\psi$. Fig. 5.4 shows a heat map of the azimuthal vorticity at time $t = 200$ of the vorticity perturbations of an axisymmetric jet with a hyperbolic tangent mean flow profile. Gaussian noise was used as the initial condition for the radial velocity perturbation $v(r, x, t)$. It can be seen that the vorticity concentrates itself into discrete structures resembling vortex rings.

5.3.4 The Spatial or Signaling Problem

The spatial problem, also known as the signaling problem, is in some ways the converse of the temporal problem. In this problem the temporal frequency ω is assumed to be real and the spatial wavenumber α is allowed to be complex. Defining the Laplace transform with respect to x by

$$\tilde{v}(r,\alpha,t) = \int_0^\infty v(r,x,t)e^{-i\alpha x}dx \quad v(r,x,t) = \frac{1}{2\pi}\int_{C_\alpha} \tilde{v}(r,\alpha,t)e^{i\alpha x}d\alpha, \quad (5.38)$$

where the bottom of the contour C_α lies below all singularities of the integrand and is closed by semi circle, which encloses the singularities, and goes off to infinity. The Fourier transform with respect to t is defined by

$$\hat{v}(r,\alpha,\omega) = \int_{-\infty}^\infty \tilde{v}(r,\alpha,t)e^{i\omega t}dt \quad \tilde{v}(r,\alpha,t) = \frac{1}{2\pi}\int_{-\infty}^\infty \hat{v}(r,\alpha,\omega)e^{-i\omega t}d\omega, \quad (5.39)$$

Writing Eq. 5.12 in component form,

$$\left[\left(\frac{\partial}{\partial t} + U\frac{\partial}{\partial x}\right)\left(D^2 + \frac{D}{r} - \frac{1}{r^2} + \frac{\partial^2}{\partial x^2}\right) - \left(U'' - \frac{U'}{r}\right)\frac{\partial}{\partial x}\right] v = 0. \quad (5.40)$$

Then applying the Laplace transform, defined in Eq. 5.38,

$$\left[\left(\frac{\partial}{\partial t} + i\alpha U\right)\left(D^2 + \frac{D}{r} - \alpha^2 - \frac{1}{r^2}\right) - i\alpha\left(U'' - \frac{U'}{r}\right)\right]\tilde{v}(r,\alpha,t) = f_0(r,t), \quad (5.41)$$

where the inhomogenous term is defined by

$$f_0(r,t) = \left[\left(i\alpha\frac{\partial}{\partial t} + i\alpha U\frac{\partial}{\partial x} + \frac{\partial^2}{\partial x \partial t} + U\frac{\partial^2}{\partial x^2}\right) + U\left(D^2 + \frac{D}{r}\right) - \left(U'' - \frac{U'}{r} + U\left(\frac{1}{r^2} + \alpha^2\right)\right)\right] v(r,0,t). \tag{5.42}$$

In the spatial problem the inhomogeneous driving term comes from the time varying boundary conditions on $v(r,x,t)$ at $x = 0$. It enters into the Laplace transformed equation because of the action of the transform on the x derivatives.

$$\begin{aligned}
\int_0^\infty \frac{\partial v(r,x,t)}{\partial x} e^{-i\alpha x} dx &= i\alpha\tilde{v}(r,\alpha,t) - v(r,0,t) \\
\int_0^\infty \frac{\partial^2 v(r,x,t)}{\partial x^2} e^{-i\alpha x} dx &= -\alpha^2\tilde{v}(r,\alpha,t) - \left[i\alpha + \frac{\partial}{\partial x}\right] v(r,0,t) \\
\int_0^\infty \frac{\partial^3 v(r,x,t)}{\partial x^3} e^{-i\alpha x} dx &= -i\alpha^3\tilde{v}(r,\alpha,t) + \left[\alpha^2 - i\alpha\frac{\partial}{\partial x} - \frac{\partial^2}{\partial x^2}\right] v(r,0,t)
\end{aligned} \tag{5.43}$$

Now applying the Fourier transform, defined in Eq. 5.39, to Eq. 5.41.

$$\left[(\omega - \alpha U)\left(D^2 + \frac{D}{r} - \frac{1}{r^2} - \alpha^2\right) + \alpha\left(U'' - \frac{U'}{r}\right)\right]\hat{v}(r,\alpha,\omega) = i\hat{f}_0(r,\omega), \tag{5.44}$$

where the Fourier transform of the inhomogenous term is

$$\hat{f}_0(r,\omega) = \left[\left(\alpha\omega + i\alpha U\frac{\partial}{\partial x} - i\omega\frac{\partial}{\partial x} + U\frac{\partial^2}{\partial x^2}\right) + U(D^2 + \frac{D}{r}) - \left(U'' - \frac{U'}{r} + U\left(\frac{1}{r^2} + \alpha^2\right)\right)\right]\hat{v}_0(r,0,\omega), \tag{5.45}$$

and the time Fourier transform of the bondary condition on the radial velocity

perturbation is

$$\hat{v}_0(r,0,\omega) = \int_{-\infty}^{\infty} v(r,0,t)e^{i\omega t}dt. \tag{5.46}$$

As in the previous section the operator on the left hand side of Eq. 5.44 is defined as

$$\mathbf{L}(\alpha,\omega) = (\omega - \alpha U)\left(D^2 + \frac{D}{r} - \frac{1}{r^2} - \alpha^2\right) + \alpha\left(U'' - \frac{U'}{r}\right). \tag{5.47}$$

The radial boundary conditions are the same as they are for the temporal problem. Thus, the problem has been converted to solving the inhomogeneous boundary value problem

$$\begin{aligned} \mathbf{L}(\alpha,\omega)\hat{v}(r,\alpha,\omega) &= i\hat{f}_0(r,\omega) \\ \hat{v}(0,\alpha,\omega) &= 0 \\ \hat{v}(2,\alpha,\omega) &= 0 \end{aligned} \tag{5.48}$$

To find the dispersion relation the corresponding homogeneous problem must be solved.

$$\begin{aligned} \mathbf{L}(\alpha,\omega)\hat{v}_h(r,\alpha,\omega) &= 0 \\ \hat{v}_h(0,\alpha,\omega) &= 0 \\ \hat{v}_h(2,\alpha,\omega) &= 0 \end{aligned} \tag{5.49}$$

In the temporal problem a real wave number alpha was selected and the generalized eigenvalue problem Eq. 5.26 was solved for ω. For the spatial

problem a real frequency ω is selected, and Eq. 5.49 is solved as a polynomial eigenvalue problem in α. Gathering the power $\mathbf{L}(\alpha, \omega)$ in powers of α,

$$\begin{aligned} \left[\mathbf{A}_0 + \alpha\mathbf{A}_1 + \alpha^2\mathbf{A}_2 + \alpha^3\mathbf{A}_3\right] \hat{v_h}(r, \alpha, \omega) &= 0 \\ \hat{v}_h(0, \alpha, \omega) &= 0 \\ \hat{v}_h(2, \alpha, \omega) &= 0 \end{aligned} \tag{5.50}$$

Here the operators $\mathbf{A}_n$ are defined by

$$\begin{aligned} \mathbf{A}_0 &= \omega\left(r^2D^2 + rD - 1\right) \\ \mathbf{A}_1 &= -U\left(r^2D^2 + rD - 1\right) - rU' + r^2U'' \\ \mathbf{A}_2 &= -\omega r^2 \\ \mathbf{A}_3 &= r^2U \end{aligned} \tag{5.51}$$

The polynomial eigenvalue problem can then be solved for eigenvalues α and eigenfunctions $\hat{v_h}(r, \alpha, \omega)$. The scientific computing package Octave contains the function polyeig, which solves eigenvalue problems of this type. Fig. 5.5 and Fig. 5.6 show the eigenvalue spectrum for $\omega = 1$. The script spatial_problem.py, in the Gitlab repository, contains the code necessary to generate these figures. The eigenvalues α are the solutions of the dispersion relation $\mathbf{D}(\alpha, \omega) = 0$ for a given ω.

To solve the inhomogeneous problem the eigenfunctions and eigenvalues of the operator $\mathbf{L}(\alpha, \omega)$ must be found. Once this is done the inhomogeneous solution can be expressed as an expansion of the eigenfunctions. The

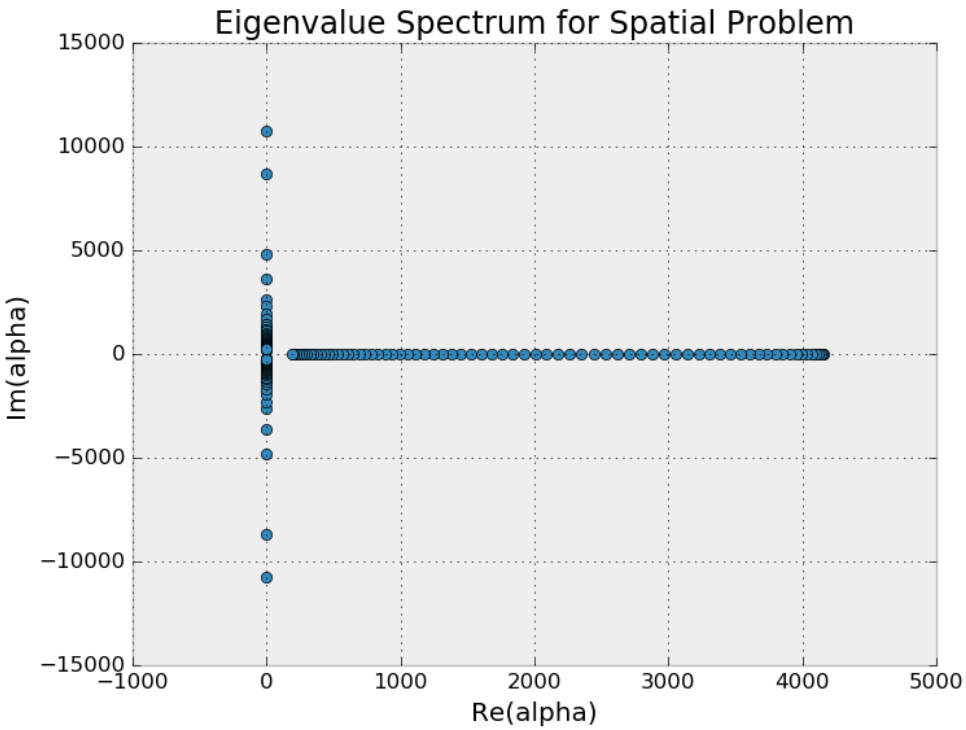

Figure 5.5: Eigenvalue spectrum for the spatial problem for $\omega = 1$. The neutrally stable eigenvalues obscure the view of the more interesting structure closer to the origin. Fig. 5.6 shows the spectrum without the mutually stable modes.

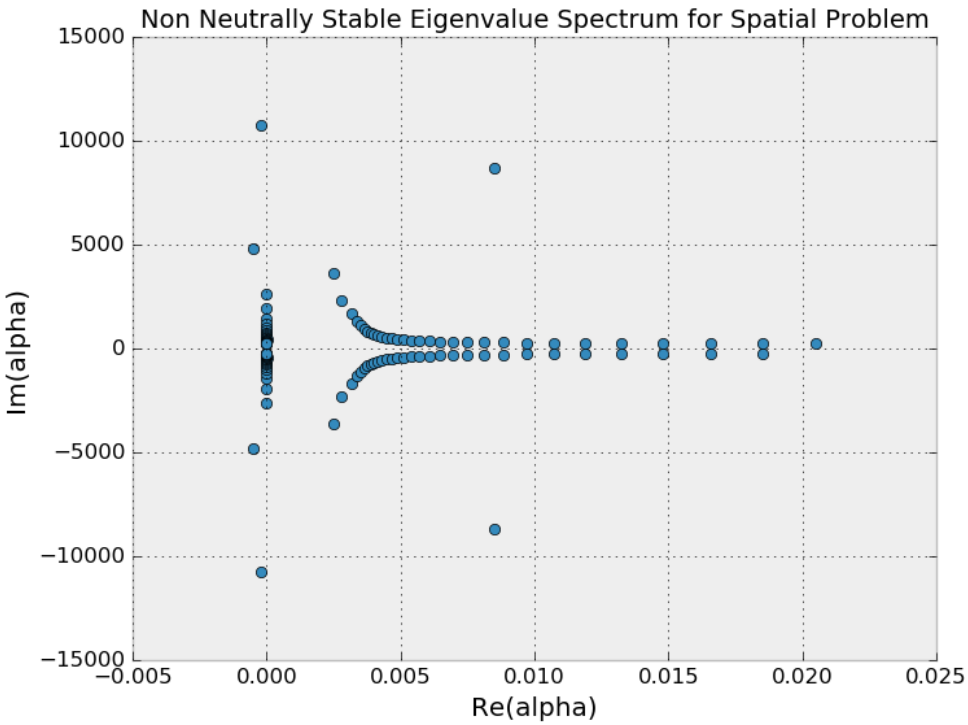

Figure 5.6: Eigenvalue spectrum for the spatial problem without the neutrally stable modes shown. The structure of spectrum for the spatial problem is more complex than that for the temporal problem. In addition many of these eigenvalues are acausal and thus must be ignored when computing the velocity response given by Eq. 5.59.

eigenvalue problem can be expressed as

$$\mathbf{L}(\alpha,\omega)\hat{v}_n(\alpha,\omega) = \lambda_n(\alpha,\omega)\hat{v}_n(r,\omega) \tag{5.52}$$

Expanding the solutions and driving term of Eq. 5.21 on to the eigenfunctions,

$$\begin{aligned} \hat{v} &= \sum_n a_n \hat{v}_n \\ \hat{f}_0 &= \sum_n f_n \hat{v}_n, \end{aligned} \tag{5.53}$$

where $f_n = (\hat{f}_0(r,\omega), \hat{v}_n(r,\omega))$. Plugging these expansions back into the original problem

$$\sum_n a_n \lambda_n \hat{v}_n = i \sum_n f_n \hat{v}_n. \tag{5.54}$$

Since the eigenvectors $\{\hat{v}_1, \hat{v}_2, ...\}$ are linearly independent,

$$a_n = \frac{f_n}{\lambda_n} = \frac{(i\hat{f}_0(r,\omega), \hat{v}_n(r,\omega))}{\lambda_n(\alpha,\omega)}. \tag{5.55}$$

Thus,

$$\hat{v}(r,\alpha,\omega) = \sum_n \frac{(i\hat{f}_0(r,\omega), \hat{v}_n(r,\omega))}{\lambda_n(\alpha,\omega)} \hat{v}_n(r,\omega). \tag{5.56}$$

Thus, for a given forcing $\hat{f}_0$ the inhomogenous problem has been solved in (α,ω) space. Now the solutions must be inverted back to (x,t) space. First

performing the spatial inversion,

$$v(r,x,\omega) = \frac{1}{4\pi^2}\int_{C_\alpha} d\alpha \left(\sum_n \frac{(i\hat{f}_0(r,\omega), \hat{v}_n(r,\omega))}{\lambda_n(\alpha,\omega)} \hat{v}_n(r,\omega) \right) e^{i\alpha x)} \tag{5.57}$$

The quantity $\lambda_n(\alpha,\omega)$ is an analytic function expect at its poles, which are given by the solutions of $\mathbf{D}(\alpha,\omega) = 0$, and a branch cut, which is given by the solutions of $(\omega - \alpha U) = 0$. The branch cut does not pose a problem, since the contour can be deformed around it. For a given ω the discrete solutions of the dispersion relation in the α plane are denoted as α_m. Hence, the residue theorem can be used to evaluate the integral in Eq. 5.57.

$$v(r,x,\omega) = -\sum_m (\hat{f}_0(r,\omega), \hat{v}_h(r,\alpha_m(\omega),\omega))\hat{v}_h(r,\alpha_m(\omega),\omega)e^{i\alpha_m(\omega)x} \tag{5.58}$$

Finally applying the inverse Fourier transform to invert the ω coordinate back to t.

$$\begin{aligned} &v(r,x,t) = \\ &\quad -\frac{1}{2\pi}\sum_m \int_{-\infty}^{\infty} d\omega (\hat{f}_0(r,\omega), \hat{v}_h(r,\alpha_m(\omega),\omega))\hat{v}_h(r,\alpha_m(\omega),\omega)e^{i(\alpha_m(\omega)x-\omega t)}. \end{aligned} \tag{5.59}$$

It can be seen the radial velocity perturbations have been expressed as the discrete sum of a series of integrals over ω.

5.3.5 Discussion

In theory the spatial problem should have a most unstable frequency the way the temporal problem has a most unstable wavelength. However, many of the eigenvalues obtained from the polynomial eigenvalue problem represent non causal modes of propagation. These eigenvalues need to be classified before the velocity response in the pipe can be computed from Eq. 5.59. This may be a future avenue of research. However, it is important to question the utility of further investigating the eigenvalue spectrum of the linear spatial problem, since it is likely that nonlinear effects are important in vorticity generation in the rat vocal tract. Furthermore, the velocity response given by Eq. 5.59 is calculated in Fourier space then transformed back to temporal space. This requires knowledge of the driving velocity at the origin $v(r, 0, t)$ for all time. This drawback makes the frequency domain approach of this chapter incompatible with the time domain simulations of chapter 4. I believe the correct approach to modeling the nonlinear time domain behavior of the vorticity in the upper vocal tract is to expand the flow solutions of the Euler or Navier-Stokes equations on to spatial eigenfunctions with time varying coefficients, similar to what was done in chapter 4. This will result in a nonlinear time domain system of which the low dimensional dynamics can be investigated. An approach similar to this was taken by Horwitz in investigating the nonlinear stability of axisymmetric jets [62].

5.4 Nonlinear Time Domain Approach

As discussed in the previous section the problem with the frequency domain approach taken thus in far in this chapter is it is difficult to reconcile it with the time domain approach of chapter 4. Furthermore, by neglecting nonlinear terms in the fluid equations the analysis predicts that any perturbation will grow without bound. Thus, in the section a nonlinear time domain approach will be taken to modeling the force due to vortex ring formation. To make the analysis tractable it will be assumed the vortex flow to be axisymmetric. This assumption is justified by Chanaud and Powell, who observed vortex ring formation in the generation of hole tone whistles to be axisymmetric [43]. While it is possible that azimuthal perturbations are important in the formation of acoustic tones, it is worthwhile to first investigate axisymmetric perturbations before including this complication. The flow will be assumed to be inviscid. This is also to make the problem tractable, and this assumption may need to be relaxed at a later point. The general approach of this section will be similar to the one taken in chapter 4. A set of suitable spatial eigenfunctions will be found. The solutions of the fluid equations of motion will then be expanded onto the spatial eigenfunctions in the form of a truncated series. The spatial part of the problem will be integrated out, and a set of time domain ODEs, which govern the behavior of the time varying coefficients, will then be derived.

The axisymmetric velocity of the jet will be written in cylindrical coor-

dinates as $\mathbf{u} = (u, v, 0)$, where u and v are the axial and radial components of the velocities. Due to the incompressible axisymmetric nature of the flow the velocities can be expressed in terms of the Stoke's stream function.

$$u = \frac{1}{r}\frac{\partial \Psi}{\partial r} \quad v = -\frac{1}{r}\frac{\partial \Psi}{\partial x} \tag{5.60}$$

Substituting Eqs. 5.60 into the incompressible Euler equation. The fluid equations of motion can be written in stream function form.

$$\frac{\partial}{\partial t} G\Psi + \frac{1}{r}\left(D_r \Psi D_x - D_x \Psi H\right) G\Psi = 0 \tag{5.61}$$

where $G = D_r^2 - \frac{D_r}{r} + D_x^2$ and $H = D_r - \frac{2}{r}$. Here the derivatives with respect to x and r are written as D_x and D_r. The boundary conditions are

$$\begin{aligned} &D_r \Psi(r, 0, t) = u_f(t) r P(r) \quad D_r D_x \Psi(r, 1, t) = 0 \\ &D_x \psi(r_0, x, t) = 0 \quad \frac{1}{r} D_r \psi(0, x, t) \quad \text{finite} \end{aligned} \tag{5.62}$$

Here $P(r) = \frac{1}{2}\left(1 - \tanh\left(\frac{1-r}{2\theta}\right)\right)$ is the hyperbolic tangent jet profile. It takes into the account that the velocity at the vocal folds is $u_f(t)$ for $r < r_f$ and approximately 0 outside that radius.

To perform the analysis, first the inhomogeneity in the boundary conditions must be transferred to the equation itself. This can be done with the

substitution

$$\begin{aligned}\Psi(r,x,t) &= \psi(r,x,t) + u_0(t)\chi_0(r,x) \\ \chi_0(r,x) &= C_E(x-1)^2 \int rP(r)dr\end{aligned} \tag{5.63}$$

Here $u_0(t)$ is the velocity entering the pharynx as it was defined in chapter 4. This quantity will be important in connecting the vortical flow of this chapter back to the acoustic of chapter 4. With this substitution the equation of motion becomes

$$\begin{aligned}&\left(D_t + \frac{1}{r}(D_r u_0(t)\chi_0 D_x - D_x u_0(t)\chi_0 H)\right) G\psi \\ &+ \frac{1}{r}(D_x G u_0(t)\chi_0 D_r - HG u_0(t)\chi_0 D_x)\psi \\ &+ \frac{1}{r}\left(D_r\psi D_x G\psi - D_x\psi HG\psi\right) \\ &+ \frac{1}{r}\left(D_r u_0(t)\chi_0 D_x G u_0(t)\chi_0 - D_x u_0(t)\chi_0 HG u_0(t)\chi_0\right) \\ &+ \dot{u}_0(t)G\chi_0 = 0\end{aligned} \tag{5.64}$$

The boundary conditions become.

$$\begin{aligned}&D_r\psi(r,0,t) = 0 \quad D_r D_x\psi(r,1,t) = 0 \\ &D_x\psi(r_0,x,t) = 0 \quad \frac{1}{r}D_r\psi(0,x,t) \quad \text{finite}\end{aligned} \tag{5.65}$$

Because of it's position in Eq. 5.64 the solutions of the eigenvalue problem associated with the operator G are a good choice for the required spatial eigenfunctions. The eigenfunctions can be obtained by solving the Sturm-

Liouville boundary value problem.

$$\begin{aligned} &G\psi_{ij}(r,x) = \lambda_{ij}\psi_{ij}(r,x) \\ &\psi_{ij}(r,0,t) = 0 \quad \frac{\partial \psi_{ij}(r,1,t)}{\partial x} = 0 \\ &\psi_{ij}(r_0,x,t) = 0 \quad \frac{1}{r}D_r\psi_{ij}(0,x,t) = \text{finite} \end{aligned} \tag{5.66}$$

It should be noted that the eigenfunctions of G are chosen as a basis because of algebraic convenience. There most likely exists a basis, which more efficiently captures the dynamics of the solutions of Eq. 5.64. The solutions of the eigenvalue problem are given by

$$\begin{aligned} \psi_{ij}(r,x) &= rJ_1(j_{1,i}\frac{r}{r_0})\sin\left(\left(j-\frac{1}{2}\right)\pi x\right) \\ \lambda_{ij} &= \left(\frac{j_{1,i}}{r_0}\right)^2 + (2j-1)^2\frac{\pi^2}{4} \quad i,j \geq 1 \end{aligned} \tag{5.67}$$

The eigenfunctions are indexed by two subscripts, one for the axial modes and one for the radial ones. For notational convenience these two subscripts will be combined together with the following transformation. If the number of modes are truncated to N_x axial modes and N_r radial modes. The subscripts i and j can be expressed as a function of a single subscript n, such that

$$\begin{aligned} \psi_n(r,x) &= rJ_1(j_{1,i(n)}\frac{r}{r_0})\sin\left(\left(j(n)-\frac{1}{2}\right)\pi x\right) \\ \lambda_n &= \left(\frac{j_{1,i(n)}}{r_0}\right)^2 + (2j(n)-1)^2\frac{\pi^2}{4} \\ i(n) &= floor(n/N_r)+1, \quad j(n) = n - i(n)N_r + 1, \quad n \geq 0 \end{aligned} \tag{5.68}$$

The orthogonality relation for the eigenfunctions is

$$< \psi_n(r,x), \psi_m(r,x) >= \int_0^{r_0} \int_0^1 \frac{1}{r} \psi_n(r,x)\psi_m(r,x) dr dx = \Lambda_n \delta_{nm}, \quad (5.69)$$

where $\Lambda_n =< \psi_n, \psi_n >$.

Now revisiting Eq. 5.64, after some reorganization it can be written as

$$\begin{aligned} & D_t G\psi + \frac{u_0(t)}{r}(D_r\chi_0 D_x G - D_x\chi_0 HG + D_x G\chi_0 D_r - HG\chi_0 D_x)\psi \\ & + \frac{1}{r}\left(D_r\psi D_x G\psi - D_x\psi HG\psi\right) \\ & + \frac{u_0(t)^2}{r}\left(D_r\chi_0 D_x G\chi_0 - D_x\chi_0 HG\chi_0\right) + \dot{u}_0(t)G\chi_0 = 0 \end{aligned} \quad (5.70)$$

Expanding the solutions onto the eigenfunctions of G,

$$\psi(r,x,t) = \sum_m a_m(t)\psi_m(r,x) \quad (5.71)$$

and substituting this expression into 5.70,

$$\begin{aligned} & \sum_m \lambda_m \dot{a}_m(t)\psi_m \\ & + \frac{u_0(t)}{r}\sum_m a_m(t)(D_r\chi_0 D_x G - D_x\chi_0 HG + D_x G\chi_0 D_r - HG\chi_0 D_x)\psi_m \\ & + \frac{1}{r}\sum_{m,l} a_m(t)a_l(t)(D_r\psi_m D_x G\psi_l - D_x\psi_m HG\psi_l) \\ & + \frac{u_0(t)^2}{r}\left(D_r\chi_0 D_x G\chi_0 - D_x\chi_0 HG\chi_0\right) + \dot{u}_0(t)G\chi_0 = 0 \end{aligned} \quad (5.72)$$

Taking the inner product of this equation with ψ_n the time domain set of equations governing the evolution of $a_n(t)$ are obtained.

$$\dot{a}_n(t) + u_0(t)\sum_{m=0}^{N_a} B_{mn}a_m(t) + \sum_{l,m=0}^{N_a} C_{lmn}a_m(t)a_l(t) + u_0(t)^2 d_n + \dot{u}_0(t)f_n = 0 \tag{5.73}$$

In this set of equations the constants encode the spatial information of the problem and are written as

$$\begin{aligned}
\Lambda_n &= < \psi_n, \psi_n > \\
B_{mn} &= \frac{1}{\lambda_n \Lambda_n} < \psi_n, \frac{1}{r}(\lambda_m D_r \chi_0 D_x - \lambda_m D_x \chi_0 H + D_x G \chi_0 D_r - HG\chi_0 D_x)\psi_m > \\
C_{lmn} &= \frac{1}{\lambda_n \Lambda_n} < \psi_n, \frac{\lambda_l}{r}(D_r \psi_m D_x \psi_l - D_x \psi_m H \psi_l) > \\
d_n &= \frac{1}{\lambda_n \Lambda_n} < \psi_n, \frac{1}{r}(D_r \chi_0 D_x G \chi_0 - D_x \chi_0 HG\chi_0) > \\
f_n &= \frac{1}{\lambda_n \Lambda_n} < \psi_n, G\chi_0 >
\end{aligned} \tag{5.74}$$

5.4.1 Connection to Acoustic Flow

Now that a set of time domain equations that govern the evolution of $a_n(t)$ has been obtained the vortical flow of this chapter will be connected to the acoustic flow of chapter 4. Recall from the previous chapter the time domain equations governing the the velocity of the flow u_0, entering the pharynx, and the modal participation factors $\vec{q}(t)$, which describe the temporal behavior

of the acoustic oscillations are given by

$$\dot{u}_0 = \mu^{-1}\left(p - p_{src} + \sum_i^{N_q} \dot{q}_i - \frac{\gamma}{2}u_0^2\right) \tag{5.75}$$

$$\ddot{\vec{q}} + \boldsymbol{D}'\dot{\vec{q}} + \frac{\gamma}{\mu^2}u_0\vec{B}'\cdot\dot{\vec{q}} + \boldsymbol{K}'\vec{q} = \vec{B}'\frac{\gamma}{\mu^2}u_0 p_{src} - \vec{B}'\frac{\gamma}{\mu}\dot{p}_{src} - \left(\vec{A}' + \vec{B}'\frac{\gamma}{\mu^2}p\right)u_0 + \vec{B}'\frac{\gamma^2}{2\mu^2}u_0^3, \tag{5.76}$$

Examining Eqs. 5.73 and 5.76 it can be seen that the velocity u_0 drives both the acoustic and vortical flow. Additionally the change in vorticity associated with Eq. 5.73 induce a pressure on the acoustic flow. From Eq. 5.2, this pressure source due to vorticity is given by

$$p_{src} = \frac{1}{2\pi r_0^2}\int_V \left(\mathbf{r}\times\frac{\partial\boldsymbol{\omega}}{\partial t}\right)_x dV \tag{5.77}$$

Writing out the cross product and volume element in cylindrical coordinates,

$$p_{src} = \frac{1}{2\pi r_0^2}\int_0^{r_0}\int_0^1 r^2\frac{\partial\omega_\phi(r,x,t)}{\partial t}drdx \tag{5.78}$$

In the previous section recall the stream function was expressed as

$$\Psi(r,x,t) = \sum_n a_n(t)\psi_n(r,x) + u_0(t)\chi(r,x) \tag{5.79}$$

The azimuthal component of the vorticity is given by $\omega_\phi = -\nabla^2\Psi(r,x,t)$. Thus, its time derivative is given by

$$\frac{\partial \omega_\phi}{\partial t} = -\sum_n \dot{a}_n(t)\nabla^2\psi_n(r,x) - \dot{u}_0(t)\nabla^2\chi(r,x) \tag{5.80}$$

Thus the pressure source can be expressed as

$$\begin{aligned} p_{src} &= -\sum_i \zeta_i \dot{a}_i - \dot{u}_0\eta \\ \zeta_i &= \frac{1}{r_0^2}\int_0^{r_0}\int_0^1 r^2\nabla^2\psi_i(r,x)drdx \\ \eta &= \frac{1}{r_0^2}\int_0^{r_0}\int_0^1 r^2\nabla^2\chi(r,x)drdx \end{aligned} \tag{5.81}$$

Substituting Eq. 5.73 into the expression for the pressure source,

$$p_{src} = u_0\sum_{m,n=0}^{N_a} B_{mn}\zeta_n a_m + \sum_{l,m,n=0}^{N_a} C_{lmn}\zeta_n a_m a_l + u_0^2\sum_{n=0}^{N_a} d_n\zeta_n + \dot{u}_0\left(\eta + \sum_{n=0}^{N_a} f_n\zeta_n\right) \tag{5.82}$$

The substituting in Eq. 5.75 for the $\dot{u}_0$ term and solving for p_{src}.

$$\begin{aligned} p_{src} = u_0\sum_{m,n=0}^{N_a} B_{mn}\zeta_n a_m + \sum_{l,m,n=0}^{N_a} C_{lmn}\zeta_n a_m a_l + u_0^2\sum_{n=0}^{N_a}\left(d_n\zeta_n + \frac{\gamma}{2\mu}\left(\eta + \sum_{n=0}^{N_a} f_n\zeta_n\right)\right) + \\ \mu^{-1}\left(p - p_{src} + \sum_i^{N_q}\dot{q}_i\right)\left(\eta + \sum_{n=0}^{N_a} f_n\zeta_n\right) \end{aligned} \tag{5.83}$$

Solving this for p_{src} and writing it in vector form

$$p_{src} = \frac{u_0}{1+\frac{\eta+\vec{f}.\vec{\zeta}}{\mu}}\mathbf{B}.\vec{a}.\vec{\zeta}+\frac{u_0^2}{1+\frac{\eta+\vec{f}.\vec{\zeta}}{\mu}}\left(\left(\vec{d}+\frac{\gamma}{2\mu}\vec{f}\right).\vec{\zeta}+\frac{\gamma}{2\mu}\eta\right)+\frac{\eta+\vec{f}.\vec{\zeta}}{\mu+\eta+\vec{f}.\vec{\zeta}}\left(p+\sum_i^{N_q}\dot{q}_i\right) + \frac{1}{1+\frac{\eta+\vec{f}.\vec{\zeta}}{\mu}}\sum_{l,m,n=0}^{N_a} C_{lmn}\zeta_n a_m a_l \quad (5.84)$$

Now taking the time derivative of this expression

$$\dot{p}_{src} = \frac{\dot{u}_0\mathbf{B}.\vec{a}.\vec{\zeta}}{1+\frac{\eta+\vec{f}.\vec{\zeta}}{\mu}}+\frac{u_0\mathbf{B}.\dot{\vec{a}}.\vec{\zeta}}{1+\frac{\eta+\vec{f}.\vec{\zeta}}{\mu}}+\frac{2u_0\dot{u}_0\left(\frac{\gamma\eta}{2\mu}+\left(\vec{d}+\frac{\gamma}{2\mu}\vec{f}\right)\right).\vec{\zeta}}{1+\frac{\eta+\vec{f}.\vec{\zeta}}{\mu}}+\frac{\eta+\vec{f}.\vec{\zeta}}{\mu+\eta+\vec{f}.\vec{\zeta}}\sum_i^{N_q}\ddot{q}_i + \frac{1}{1+\frac{\eta+\vec{f}.\vec{\zeta}}{\mu}}\sum_{l,m,n=0}^{N_a} C_{lmn}\zeta_n(\dot{a}_m a_l + a_m\dot{a}_l) \quad (5.85)$$

The notation can be simplified by defining

$$F(u_0,\dot{u}_0,\vec{a},\dot{\vec{a}},r_f,p) = \frac{\dot{u}_0\mathbf{B}.\vec{a}.\vec{\zeta}}{1+\frac{\eta+\vec{f}.\vec{\zeta}}{\mu}}+\frac{u_0\mathbf{B}.\dot{\vec{a}}.\vec{\zeta}}{1+\frac{\eta+\vec{f}.\vec{\zeta}}{\mu}}+\frac{2u_0\dot{u}_0\left(\frac{\gamma\eta}{2\mu}+\left(\vec{d}+\frac{\gamma}{2\mu}\vec{f}\right)\right).\vec{\zeta}}{1+\frac{\eta+\vec{f}.\vec{\zeta}}{\mu}} + \frac{1}{1+\frac{\eta+\vec{f}.\vec{\zeta}}{\mu}}\sum_{l,m,n=0}^{N_a} C_{lmn}\zeta_n(\dot{a}_m a_l + a_m\dot{a}_l). \quad (5.86)$$

The derivative of the source pressure can then be written as. The $\ddot{q}_i$ terms are left out of the function F because they are dependent variables, and they must be solved for algebraically before the equations can be input into a numerical solver.

$$\dot{p}_{src} = F(u_0,\dot{u}_0,\vec{a},\dot{\vec{a}},r_f,p) + \frac{\eta+\vec{f}.\vec{\zeta}}{\mu+\eta+\vec{f}.\vec{\zeta}}\sum_i^{N_q}\ddot{q}_i. \quad (5.87)$$

Substituting this expression into Eq. 5.76

$$\mathbf{R}^{-1}\ddot{\vec{q}} + \left(\boldsymbol{D}' + \vec{B}'\frac{\gamma}{\mu^2}u_0\right)\dot{\vec{q}} + \boldsymbol{K}'\vec{q} = \vec{B}'\frac{\gamma}{\mu^2}u_0 p_{src} - \vec{B}'\frac{\gamma}{\mu}F(u_0, \dot{u}_0, \vec{a}, \dot{\vec{a}}, r_f, p) - \left(\vec{A}' + \vec{B}'\frac{\gamma}{\mu^2}p\right)u_0 + \vec{B}'\frac{\gamma^2}{2\mu^2}u_0^3, \tag{5.88}$$

where

$$R_{jk}^{-1} = \delta_{jk} - B_j'\frac{\gamma(\eta + \vec{f}.\vec{\zeta})}{\mu(\mu + \eta + \vec{f}.\vec{\zeta})} \tag{5.89}$$

Multiplying Eq. 5.88 by the matrix $\mathbf{R}$, the differential algebraic equations can be solved for $\ddot{\vec{q}}$.

$$\ddot{\vec{q}} + \left(\boldsymbol{D} + \vec{B}\frac{\gamma}{\mu^2}u_0\right)\dot{\vec{q}} + \boldsymbol{K}\vec{q} = \vec{B}\frac{\gamma}{\mu^2}u_0 p_{src} - \vec{B}\frac{\gamma}{\mu}F(u_0, \dot{u}_0, \vec{a}, \dot{\vec{a}}, r_f, p) - \left(\vec{A} + \vec{B}\frac{\gamma}{\mu^2}p\right)u_0 + \vec{B}\frac{\gamma^2}{2\mu^2}u_0^3, \tag{5.90}$$

The Eqs. 5.90, 5.73, and 5.75 form a set of ODEs which describe the time domain behavior of the acoustic flow $\vec{q}$, the vortical driving flow $\vec{a}$, and the velocity entering the pharynx u_0. These equations can be numerically integrated. The parameters p, r_f, and r_{mouth} can be varied to reproduce the features of rodent USVs.

5.4.2 Analysis and Discussion

The subglottal pressure p is an important quantity in the control of the onset of oscillations. For low values of p oscillations will not occur, and the

solutions of the system will approach a fixed point. However, as p is increased the system undergoes some kind of bifurcation which creates a limit cycle, and acoustic oscillations will begin. This can be seen in Fig. 5.7 in which the system is integrated from rest for different values of p. It can be seen that somewhere around 700 Pa the system transitions from approaching a fixed point to approaching a steady oscillatory state. The transition can

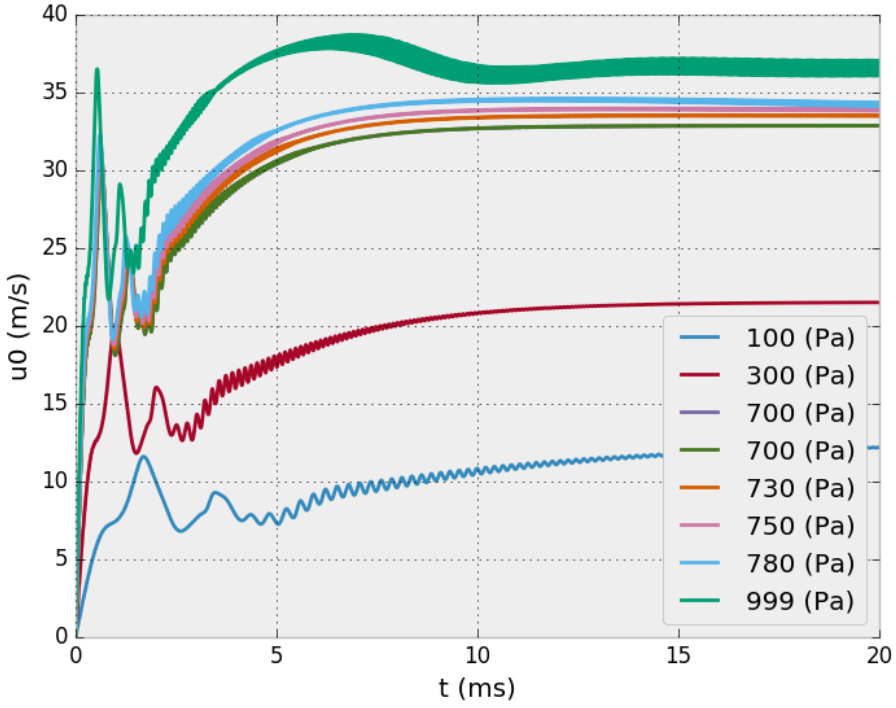

Figure 5.7: The jet velocity entering the pharynx u_0 for different values of the subglottal pressure p. Somewhere around 600 Pa the system transitions from approaching a fixed point to approaching a steady oscillatory state. In this calculation the vocal tract length is $L = 4$ mm, the pharyngeal radius is $r_p = 1.5$ mm, the tracheal radius is $r_t = 1.5$ mm, the mouth radius is $r_{mouth} = .45$ mm, and the vocal fold radius is $r_f = 1.1$ mm.

be seen more clearly by taking the Fourier transform of u_0 for each value of the subglottal pressure p after the initial transients has died out. Then plotting the modulus squared of the Fourier transform against the subglottal pressure. It can be seen that around 1500 Pa the fundamental frequency of the oscillations is around 22 kHz, the same frequency as the rat alarm call! The dynamics of the system can also be understood by plotting the fixed point, which the system approaches, and the eigenvalues of the Jacobian evaluated at that fixed point against the subglottal pressure (Fig. 5.9). For pressures less than 700 Pa. The system approaches a stable fixed point. Around 700 Pa the system undergoes some kind of bifurcation, and that fixed point loses stability. The limit cycle is unusual in that it does not orbit the fixed point but rather some point near it. By examining the real part of the least stable eigenvalue (middle plot) it can be seen the fixed point loses stability at around 700 Pa. By examining the imaginary part of the least stable eigenvalue of the Jacobian it can be seen that it is near the same frequency as the rat alarm call (22 kHz). This system has interesting bifurcation structure that should be explored more in future research.

To summarize what has been done. A set of time domain ODEs, which describe the transient behavior of acoustic oscillations in the rodent vocal tract, have been derived. It has been shown that acoustic oscillations begin with a Hopf bifurcation as subglottal pressure is increased. Once the oscillation threshold has been passed, further increasing subglottal pressure causes modulation of the emitted acoustic frequency. These are all features

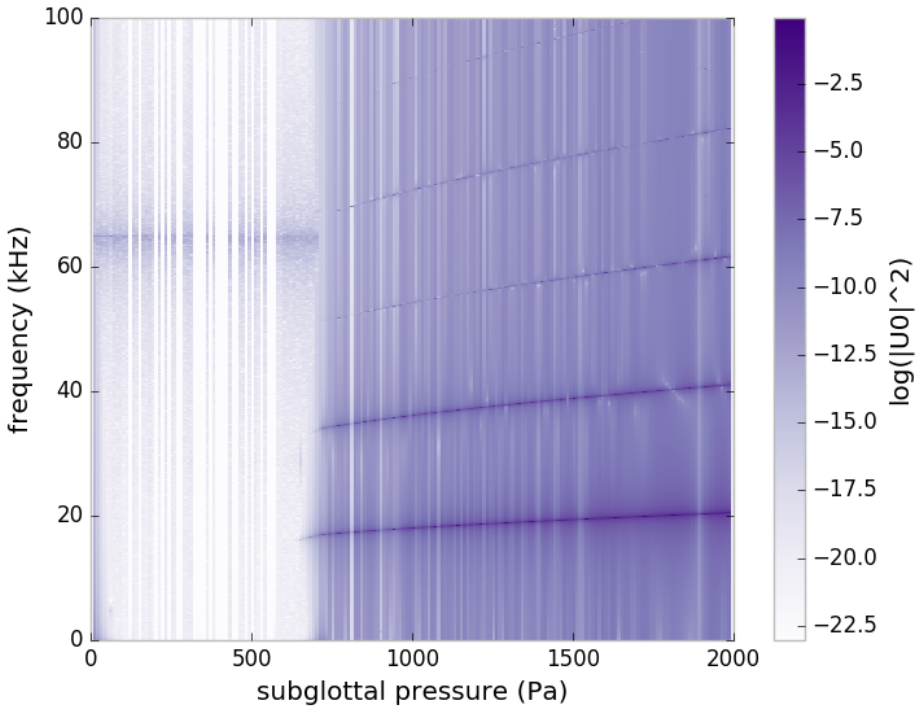

Figure 5.8: The modulus squared of the Fourier transform of u_0 plotted against the subglottal pressure p. Somewhere around 700 Pa the system transitions from approaching a fixed point to approaching a steady oscillatory state. In this calculation the vocal tract length is $L = 4$ mm, the pharyngeal radius is $r_p = 1.5$ mm, the tracheal radius is $r_t = 1.5$ mm, the mouth radius is $r_{mouth} = .45$ mm, and the vocal fold radius is $r_f = 1.1$ mm.

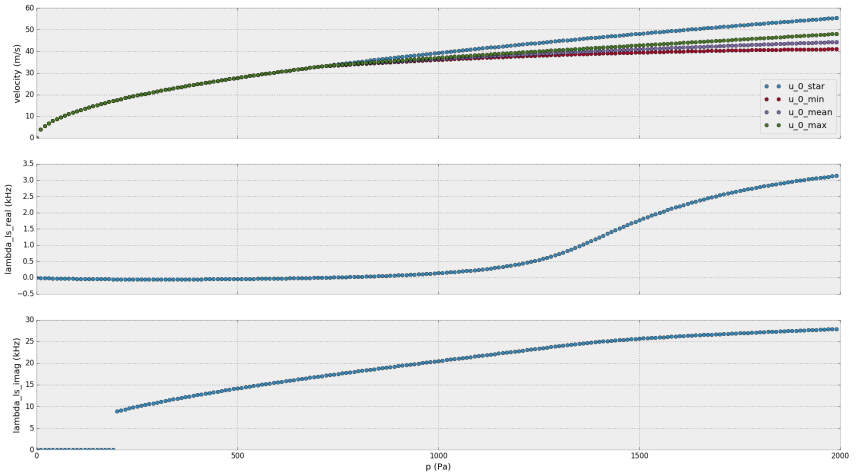

Figure 5.9: The top plot shows the fixed point, which the system approaches, as well as the minimum, maximum, and mean of the oscillations. For pressures less than 700 Pa. The system approaches a stable fixed point. Around 700 Pa the system undergoes some kind of bifurcation, and that fixed point loses stability. The limit cycle is unusual in that it does not orbit the fixed point but rather some point near it. The middle plot shows the real part of the least stable eigenvalue of the Jacobian. It can be seen the fixed point loses stability at around 700 Pa. The bottom plot shows the imaginary part of the least stable eigenvalue of the Jacobian. It can be seen that it is near the same frequency as the rat alarm call (22 kHz).

that have been observed experimentally in rodent USVs. However, frequency jumps have not been recreated using this model. It is difficult to explore the dynamics of the full parameter space of this model, since it has many fixed points. So it is possible frequency jumps occur in some regime not yet explored. However, it is also possible a mechanism has been left out of this model. It is my belief that considering the inertia of the jet as it is absorbed into the upper vocal tract with introduce a time delay factor into the time domain dynamical system governing the acoustic oscillations. I believe this may be an important factor, which will produce frequency jumps in the model. Previous modeling of acoustic systems with time delays have produced models with frequency jumps [63], [56].

Bibliography

[1] H. Gray, W. H. Lewis, and Bartleby, Anatomy of the human body, 2000.

[2] I. R. Titze, *The Myoelastic Aerodynamic Theory of Phonation* (National Center for Voice and Speech, Salt Lake City, 2006).

[3] T. Gardner *et al.*, Physical Review Letters **87**, (2001).

[4] N. H. Fletcher, Handbook of Behavioral Neuroscience **19**, 51 (2010).

[5] N. R. White, M. Prasad, R. J. Barfield, and J. G. Nyby, Physiology & Behavior **63**, 467 (1998).

[6] R. Berry, Field Studies **3**, 219 (1970).

[7] M. B. Fenton, C. V. Portfors, I. L. Rautenbach, and J. M. Waterman, Canadian Journal of Zoology **76**, 1174 (1998).

[8] G. Jones and E. Teeling, Trends in Ecology & Evolution **21**, 149 (2006).

[9] W. Bogdanowicz, Mammalian species 1 (1994).

[10] A. S. Frankel, Encyclopedia of Marine Mammals 1056 (2009).

[11] H. Whitehead, Encyclopedia of Marine Mammals 1091 (2009).

[12] L. E. Rendell *et al.*, J Zoology **249**, 403 (1999).

[13] R. Kastelein, J. Mosterd, N. Schooneman, and P. Wiepkema, Aquatic Mammals **26**, 33 (2000).

[14] T. A. Jefferson, S. Leatherwood, and M. A. Webber, *Marine mammals of the world* (Food & Agriculture Org., Rome, 1993).

[15] I. Sanders *et al.*, *Society for Neuroscience* (Society for Neuroscience, Washington, DC, 2001).

[16] R. C. Chanaud, Scientific American **222**, 40 (1970).

[17] R. Auvray, B. Fabre, and P.-Y. Lagrée, The Journal of the Acoustical Society of America **131**, 1574 (2012).

[18] I. R. Titze, J. Acoust. Soc. Am. **83**, 1536 (1988).

[19] W. Jedrzejewski and B. Jedrzejewska, Ecography **16**, 47 (1993).

[20] S. M. Brudzynski and N. H. Fletcher, Handbook of Behavioral Neuroscience **19**, 69 (2010).

[21] A. H. Bass, E. H. Gilland, and R. Baker, Science **321**, 417 (2008).

[22] M. S. Blumberg and J. R. Alberts, Behavioral Neuroscience **104**, 808 (1990).

[23] M. A. Hofer and H. N. Shair, Developmental Psychobiology **25**, 511 (1992).

[24] M. A. Hofer and H. N. Shair, Behavioral Neuroscience **107**, 354 (1993).

[25] M. A. Hofer, Handbook of Mammalian Vocalization - An Integrative Neuroscience Approach 29 (2010).

[26] S. M. Brudzynski, Behavioural brain research **182**, 261 (2007).

[27] R. Blanchard, D. Blanchard, R. Agullana, and S. M. Weiss, Physiology & Behavior **50**, 967 (1991).

[28] J. Panksepp *et al.*, Behavioral Neuroscience **121**, 1364 (2007).

[29] S. M. Brudzynski and F. Bihari, Neuroscience Letters **109**, 222 (1990).

[30] J. Burgdorf and J. R. Moskal, Handbook of Mammalian Vocalization - An Integrative Neuroscience Approach 209 (2010).

[31] G. S. Berke and J. L. Long, Handbook of Behavioral Neuroscience **19**, 419 (2010).

[32] E. J. Damrose *et al.*, Annals of Otology, Rhinology & Laryngology **112**, 434 (2003).

[33] I. Titze, *Principles of voice production* (National Center for Voice and Speech, Salt Lake City, 2000).

[34] H.-S. Choi, M. Ye, G. S. Berke, and J. Kreiman, Annals of Otology, Rhinology & Laryngology **102**, 769 (1993).

[35] I. R. Titze, J. Jiang, and D. G. Drucker, Journal of Voice **1**, 314 (1988).

[36] J. W. Bradbury and S. L. Vehrencamp, *Principles of animal communication* (Sinauer Associates, Sunderland, MA, 1998).

[37] L. Roberts, Ultrasonics **13**, 83 (1975).

[38] T. Riede, Journal of Neurophysiology **106**, 2580 (2011).

[39] T. Riede *et al.*, Journal of Biomechanics **44**, 1936 (2011).

[40] K. Inagi, E. Schultz, and C. N. Ford, Otolaryngology – Head and Neck Surgery **118**, 74 (1998).

[41] G. K. Batchelor, *An Introduction to Fluid Dynamics* (Cambridge University Press, Cambridge, 2000), cambridge Books Online.

[42] M. S. Howe, *Theory of vortex sound* (Cambridge University Press, Cambridge, 2003), Vol. 33.

[43] R. C. Chanaud and A. Powell, The Journal of the Acoustical Society of America **37**, 902 (1965).

[44] N. H. Fletcher and T. Rossing, *The physics of musical instruments* (Springer Science & Business Media, New York, 2012).

[45] J. W. S. B. Rayleigh, *The theory of sound* (Macmillan, New York, 1896), Vol. 2.

[46] A. D. Pierce *et al.*, *Acoustics: an introduction to its physical principles and applications* (McGraw-Hill, New York, 1981), Vol. 20.

[47] R. M. Aarts and A. J. E. M. Janssen, J. Acoust. Soc. Am. **113**, 2635 (2003).

[48] S. W. Rienstra and A. Hirschberg, Eindhoven University of Technology **18**, 19 (2003).

[49] A. Cummings and I.-J. Chang, Revue de Physique Applique **21**, 151161 (1986).

[50] U. Ingard, J. Acoust. Soc. Am. **42**, 6 (1967).

[51] M. S. Howe, *Acoustics of Fluid-Structure Interactions (Cambridge Monographs on Mechanics)* (Cambridge University Press, Cambridge, 2008).

[52] J. Rossiter, Technical report, Royal Aircraft Establishment, RAE Farnborough (unpublished).

[53] D. K. Holger, T. A. Wilson, and G. S. Beavers, The Journal of the Acoustical Society of America **62**, 1116 (1977).

[54] J. W. Coltman, The Journal of the Acoustical Society of America **60**, 725 (1976).

[55] N. H. Fletcher, Acta Acustica united with Acustica **34**, 224 (1976).

[56] R. Auvray, B. Fabre, and P.-Y. Lagree, J. Acoust. Soc. Am. **131**, 1574 (2012).

[57] D. Henwood, Journal of Sound and Vibration **254**, 575593 (2002).

[58] D. G. Akhmetov, *Vortex rings* (Springer Science & Business Media, New York, 2009).

[59] P. J. Morris, Journal of Fluid Mechanics **77**, 511 (1976).

[60] L. N. Trefethen, *Spectral methods in MATLAB* (Siam, Philadelphia, 2000), Vol. 10.

[61] G. K. Batchelor and A. E. Gill, J. Fluid Mech. **14**, 529 (1962).

[62] J. Horwitz and S. Rosenblat, Acta Mechanica **95**, 131156 (1992).

[63] E. M. Arneodo and G. B. Mindlin, Phys. Rev. E **79**, (2009).